Development, characterization and application of in-liquid electron imaging and diffraction techniques for high-resolution structural analysis

Dissertation

zur Erlangung des Doktorgrades

des Department Physik

der Universit¨at Hamburg

vorgelegt von

Sana Azim

aus Neu-Delhi, Indien

Hamburg 2020

Abstract

Spotting the mesoscale structural dynamics of biochemical processes in vivo with atomic-level detail has been a great technological challenge. Since a majority of these occur naturally in the solution phase, techniques allowing in-liquid observations are particularly attractive to the scientific community. Even though spectroscopic techniques permit straightforward solution-phase measurements, they nevertheless fail to provide direct structural information. Scattering techniques are mostly applied for such applications. In-liquid sample preparation techniques for electrons, which offer a greater scattering cross-section compared to X-rays, is quite challenging. The low penetration depth of the electrons imposes an additional constraint on the sample thickness.

This thesis presents the author's contribution towards the modification of the existing liquid cell technology for in-liquid real-space imaging and diffraction. Silicon based micro- and nanofabrication technology has been used to produce 20 nm thin silicon nitride windows for nanofluidic cells. The behaviour of nanofluidic cells under vacuum was characterized using a thin-film interferometer. These measurements provided insight into the deformation occurring in the silicon nitride windows, which resulted in an increase in specimen thickness. These issues led to the idea of the environmental liquid cell (ELC), where the environmental cell concept was combined with nanofluidic cell technology. The newly developed ELC method was shown to demonstrate controllable liquid thickness, which allowed imaging of gold nanoparticles, polystyrene beads, and ferritin molecules with sub-nm spatial resolution. The same technique was utilized to acquire diffraction from liquid water at room temperature. The scattering data provided information about the O•••H and O•••O pair distribution function, from which the coordination number was extracted and the values were 1.91 and 5,01, respectively. Further, the number of hydrogen bonds per water molecule was computed to be 3.8, implying a nearly tetrahedral structure of water.

Despite delivering very promising results, the ELC technique still cannot be used for phase contrast imaging which require windows as thin as 10 nm. Moreover, the windows in the ELC are prone to failure. These shortcomings prompted the design idea of the elliptical multi-window liquid cell for phase-contrast imaging.

Zusammenfassung

Die Untersuchung von Strukturdynamik biochemischer Prozesse mit atomarer räumlicher Auflösung in vivo ist eine große technische Herausforderung. Da diese Prozesse meist in wässrigem Milieu auftreten sind Techniken, die Beobachtungen in flüssiger Form ermöglichen, für Wissenschaftler besonders attraktiv. Auch wenn spektroskopische Techniken einfache Messungen in der Lösungsphase erlauben, liefern sie dennoch keine direkten Strukturinformationen. Für solche Anwendungen werden meist Streuungstechniken eingesetzt. Präparationstechniken für flüssige Proben, welche mittels Elektronenmikroskopie oder Elektronenbeugung untersucht werden sollen, stellen im Vergleich zu den auf Röntgenstrahlen basierten Analogen eine große Herausforderung dar. Ein wesentlicher Grund hierfür ist der größere Streuquerschnitt der Elektronen, welcher zu einer geringeren Eindringtiefe führt und somit sehr dünne Proben erfordert.

In dieser Arbeit wird der Beitrag des Autors zur Modifizierung der bestehenden Flüssigkeitszellentechnologie für die Realabbildung als auch Beugung von flüssigen Proben vorgestellt. Auf Silizium basierende Mikro- und Nanofabrikationstechnologien wurden eingesetzt, um 20 nm dünne Siliziumnitridfenster für Nanofluidikzellen herzustellen. Das Verhalten von Nanofluidikzellen unter Vakuum wurde mit Hilfe eines Dünnschichtinterferometers charakterisiert. Diese Messungen gaben Aufschluss über die in den Siliziumnitridfenstern auftretende Verformung, die zu einer unerwünschten Zunahme der Probendicke führte. Um dieses Problem zu umgehen, wurde die Idee der Umgebungsflüssigkeitszelle (ELC) konzipiert. Hierbei handelt es sich im Wesentlichen um eine Kombination von Ansätzen herkömmlicher environmental Transmissionselektronenmikroskopie mit der Nanofluidik-Zellentechnologie. Die neu entwickelte ELC-Methode erlaubte die Verwirklichung eines Flüssigkeitsfilms kontrollierbarer Dicke, was seinerseits die Abbildung von Goldnanopartikeln, Polystyrolkügelchen und Ferritinmolekülen mit einer räumlichen Auflösung von besser als einem Nanometer ermöglichte. Dieselbe Technik wurde zur Erfassung der Beugung an flüssigem Wasser bei Raumtemperatur verwendet. Die Streudaten lieferten Informationen über die O---H- und O---O-Paar-Verteilungsfunktion, aus denen die Koordinationszahl extrahiert wurde und die Werte 1,91 bzw. 5,01 betrugen. Weiterhin wurde berechnet, dass die Anzahl der Wasserstoffbrückenbindungen pro Wassermolekül 3,8 beträgt, was eine nahezu tetraedrische Struktur des Wassers impliziert.

Obwohl die ELC-Technik sehr vielversprechende Ergebnisse liefert, konnte sie bisher noch nicht für die Phasenkontrast-Bildgebung eingesetzt werden. Hierfür sind Siliziumnitridfenster von etwa 10 nm Dicke erforderlich. Darüber hinaus sind die soweit genutzten Fenster in der ELC fragil, und somit unzuverlässig. Diese Unzulänglichkeiten gaben den Anstoß zu der Konstruktionsidee der elliptischen Mehrfenster-Flüssigkeitszelle für die Phasenkontrast-Bildgebung.

Declaration

Declaration on oath

I hereby declare, on oath, that I have written the present dissertation by my own and have not used other than the acknowledged resources and aids.

Eidesstattliche Versicherung

Hiermit erkläre ich an Eides statt, dass ich die vorliegende Dissertationsschrift selbst verfasst und keine anderen als die angegebenen Quellen und Hilfsmittel benutzt habe.

Dedication

I dedicate this to my mom and dad, who deserve this and much more.

I. Table of Contents

List of Figures

List of Tables

1 Introduction

The contributions of science and technology towards understanding our environment is unquestionable. The most bewildering of all the ongoing scientific research, from the author's point of view, is the origin and functionality of life. One of the main challenges here lies in resolving the structure/function relationship of biological machines and their contribution to biological systems. Therefore, solving this problem requires not only obtaining atomic-level information from these structures but also gaining insight from their dynamics. Several existing techniques show great promise in exploring the structures and the involved dynamics in molecules/molecular processes occurring at different length and time scales; Figure 1.1 highlights a few of these.
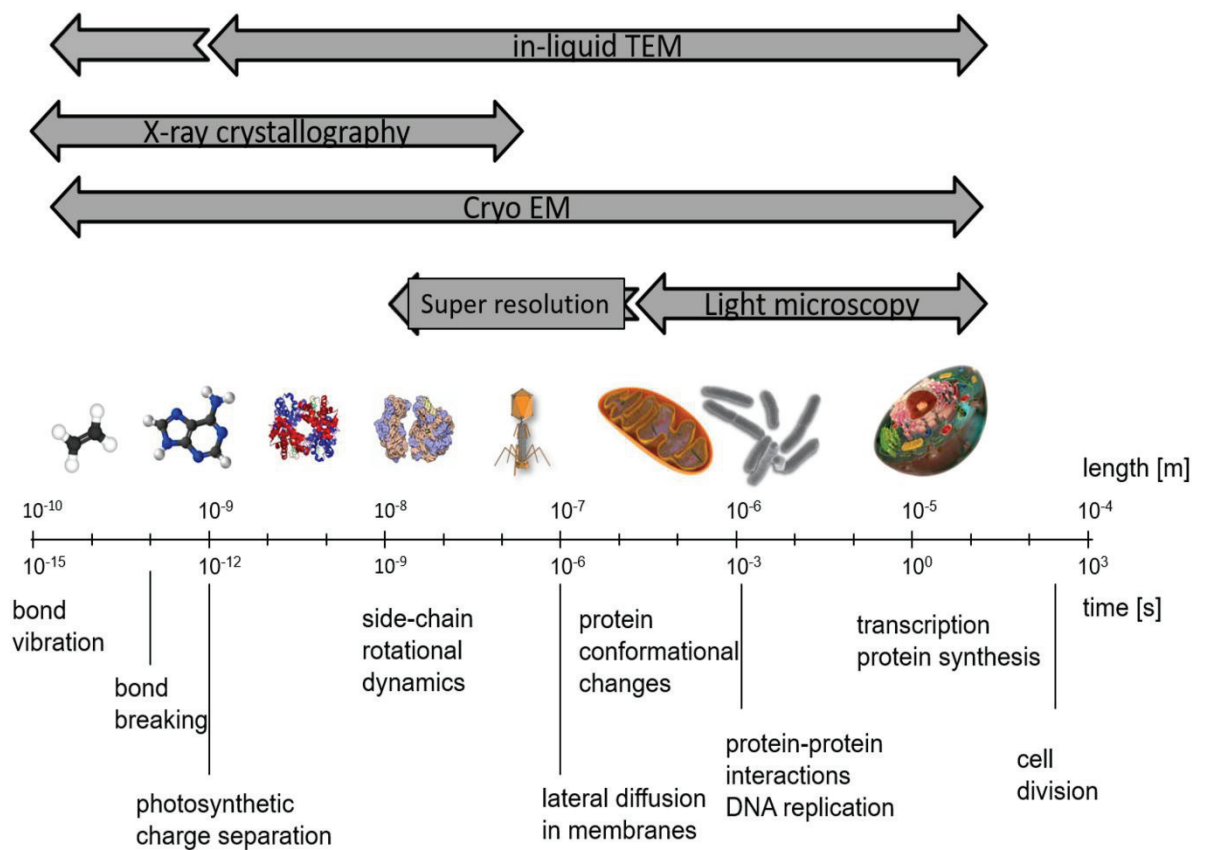
Figure 1.1: Time and length scale of different chemical-biological processes highlighting the various techniques available. These are utilized in getting more in-depth insight into different structures and their related dynamics.

Light microscopy is popular for investigating larger processes/structures such as cell division in mammalian cells which are submillimeter in size. As we move towards smaller spatial dimensions, see Figure 1.1, super-resolution microscopy is available for exploring structure/functionalities, which are otherwise not possible with light microscopy due to the limited resolution. The third widely used method is cryogenic electron microscopy (Cryo-EM), which can resolve sub-nanometer structures with a time resolution of 1 ms, limited by the vitrification step. Thereafter, we have X-ray crystallography which can capture structures with sub-Angstrom spatial resolution within temporal gating windows ranging from femtoseconds (fs) to minutes. The next technique shown in Figure 1.1, is in-liquid imaging. This method can be used to capture the structure of a system and its related motions in solution phase. The fact that a large number of chemical/biological processes occur naturally in the liquid state has made this a top-rated tool. Although the focus of this thesis is in-liquid electron microscopy, some background about the capabilities of other techniques will help understand the topic better.

Light microscopy, particularly the confocal and fluorescence variants, is the most ubiquitous of the aforementioned methods and allows *in situ* imaging of biological structures in their native environment [1]–[4]. However, the spatial resolution achieved is limited by the wavelength of the illumination source ($\lambda = 400\text{-}700$ nm) [5]. New developments in the field of visible light microscopy, such as super-resolution microscopy, can achieve higher resolutions [6]. Stimulated emission depletion microscopy (STED) developed by Stefan Hell works on the principle of non-linear optical effects and allows resolutions as high as 35 nm [7]. The disadvantage with STED is that it requires high-intensity laser excitation that cannot be used for biological samples, as it can damage the specimen. Another variation of optical microscopy is Stochastic optical reconstruction microscopy (STORM), which uses photo-switchable fluorescent labels and a series of images to construct a model [8]. With a resolution of 20-30 nm, this technique is still insufficient to gain insight about the atomic-level details of biomolecules. Additionally, this technique does not allow label-free imaging which deprives a significant class of samples of being investigated [9]–[11].

With the advent of X-ray crystallography (XRC) in 1912, it was possible to investigate the atomic and molecular structure of crystals [12]. Using principles of diffraction, a three-dimensional electron density map is created by measuring the angles and intensities of the diffracted beam while using phasing methods to obtain structure factors. From this map, information about the mean position of the atoms in the crystal, their chemical bonds, and any disorder present can be extracted. In its early days, XRC was mainly used to study materials

like copper sulphate and zinc blend [13]. After the breakthrough discovery of protein crystallization, the technique was used to reveal the structure of a multitude of different proteins, DNA and other biological macromolecules [14]–[17]. This field has made some remarkable progress recently with the advent of time-resolved XRC [18]–[20].

The concept of X-ray crystallography can be extended with electrons and neutrons as similar diffraction patterns are obtained from these. Electron diffraction has been utilized to determine structural details of liquid water, as described in Chapter 6 of this thesis. Other techniques such as powder diffraction and small-angle X-ray scattering are also available for working with polycrystalline materials. However, the information extracted can be less detailed than single crystal techniques [21], [22]. In the case of nanocrystals, electron beams are better suited probes [23]–[27]. Also, electrons are used to observe atomic motions via ultra-fast electron diffraction method, which is capable of providing a picometer spatial resolution and femtosecond time resolution, as shown by Siwick *et al*. in 2003 and Ishikawa *et al*. in 2015 [28]–[30].

Compared to X-ray crystallography Cryo-EM is a more versatile technique because it does not impose any restriction on the size or crystallinity of the specimen and deliver a resolution as good as the former. Cryo-EM has evolved as a crucial method for studying the structure and dynamics of large macromolecular complexes and viruses [31]–[35]. The material of interest is applied to a grid-mesh in the aqueous form, which is then plunge-frozen in liquid ethane or a liquid ethane/propane mix [36], [37]. The plunge-freezing step is done to ensure that the internal structure of the molecules remains intact in the high vacuum environment of a transmission electron microscope (TEM) during the image acquisition process [38]. A true atomic-level resolution has been obtained for several biomolecular structures with the development of the latest detectors and software technologies [27], [39].

None of the above-mentioned techniques can, however, provide information about the structure and dynamics of specimens in their native environment. This is possible only via in-liquid imaging and diffraction. X-ray diffraction in liquid was already possible in 1927 [40], [41]. Moreover, the time-resolved X-ray crystallography approach has provided a platform to observe the structure and its related function in macromolecules [20], [42]–[44]. A long-standing challenge was to do the same with the electrons, which have fundamental advantages over X-rays in how they interact with matter. The problem with electrons is their smaller penetration depth compared to X-rays, which restricts the maximum specimen thickness for electron imaging /diffraction. Imaging of liquid samples in TEM was first performed in 1934

by L. Marton, who successfully imaged biological specimen sandwiched between two thin aluminium foils [45]. Despite this very early start, growth in the field was slow as not much development was made in the next few decades [46]–[53]. This field only received significant attention by the researchers from other areas such as material science and biology, after the introduction of microfabrication technology to fabricate silicon nitride/silicon-based liquid cells, as reported by Williamson *et al.*, in 2003 [53], [54]. No flow capabilities were present in these devices. De Jonge *et al.* first used liquid cell with flow channels in 2009 to image a whole biological cell [53], [55]. Compared to the static design, the construct of a flow liquid cell was not much different; the only modification being the addition of external tubing and a syringe pump [56]. The flow design was a delight for the researchers interested in applications like *in situ* solvent mixing or reagent flow [53]. However, there were problems linked to this flow cell design. Some had specimen drift due to the flowing liquid, as well as window rupture and possible contamination [53]. Mueller *et al.*, in 2013, reported a flow liquid cell with active feedback to control the sample drift [57].

In 2012, Park *et al.* used a graphene liquid cell to capture the growth of platinum nanocrystals at high resolution [58]. The sample was prepared by dispensing a small volume of the liquid specimen between two graphene sheets [59]. Graphene being impermeable to liquids and the thinnest material available is a perfect candidate for high-resolution imaging. While GLC's are excellent candidates for in-liquid imaging/diffraction, their incompatibility with the latest micro- and nanofabrication technology make them unsuitable for complex measurements involving *in situ* flow and solvent or reagent mixing experiments. This is the reason why silicon nitride/silicon cells are still more popular among research groups as these can easily be mass-produced in cleanroom facilities and can, therefore, provide an adaptable platform to include functions such as electrodes, heating and cooling [53], [54], [60]–[62]. Additionally, silicon nitride has unique physical properties such as mechanical strength, and relative inertness, which makes it a good window material.

The main goal of the work presented by the author in this thesis is to improve the existing liquid cell technology and contribute to the enduring quest of investigating molecules and molecular processes in their native environment. Work has been done from both the fabrication and application perspectives to improve current technology. The production of thin 20 nm liquid cells was followed by the development of the environmental liquid cell (ELC) setup. The author has utilized this new ELC TEM technique to perform in-liquid electron

imaging and diffraction. Henceforward, the author provides brief details of different chapters in this thesis.

Chapter 2 introduces the concept and methods implemented in other parts of this thesis. An introduction to liquid-phase electron microscopy is provided and describing the probing tool. In chapters 3 and 4, the author discusses the technical details involved in the fabrication and characterization of liquid cells. In Chapter 3, the three essential cleanroom techniques used by the author in the development of liquid cells are discussed at length. Detailed fabrication steps involved in the fabrication of standard liquid cells are presented. In chapter 4, the basic characterizations done to evaluate the performance of conventional liquid cells are discussed, and a new design idea for better liquid cells is presented. Chapter 5 describes the environmental liquid cell technique developed by the author to overcome the drawbacks of standard liquid cells. The technical details of the equipment used are discussed, and the results from the proof of principle experiments performed by the author are presented.

In chapter 6, results from electron diffraction measurements conducted by the author utilizing the environmental nanofluid cell technology developed in chapter 5 are presented. Chapter 7 contains work done by the author using negative stain electron microscopy. The author has done this work to study the aggregation behaviour of human γS-crystallin, present in the human eye lens. While initially intended as an liquid phase transmission electron microscopy (LPTEM) project, it was not possible to attain sufficient contrast and resolution therewith. In chapter 8, the author provides a summary of the work presented in this thesis. At the end of this thesis, preliminary results on real-space imaging performed by the author on different biological structures and a list of forthcoming publications are attached as appendixes.

2 Transmission electron microscope: a tool to probe liquid specimens

To answer the scientific questions involved in the field of liquid-phase transmission electron microscopy (LPTEM), the fundamentals of electrons as a probing tool as well as liquid specimen encapsulation technology must be well understood. In this chapter, the author provides an overview of the LPTEM, while a substantial part has been dedicated to discuss the physical mechanisms involved in probing a specimen via a TEM. Particular emphasis has been laid to explain the factors such as resolution/contrast and electron beam damage, which affect the quality of the TEM micrograph. The theoretical discussions are limited to the concepts and methods relevant to the experimental work done in chapter 5, 6 and 7. Liquid encapsulation technology is discussed at length in chapter 3.

To provide an overview of liquid phase transmission electron microscopy, the state of the art is discussed in section 2.1. In section 2.2, the idea of using an electron as a probe as opposed to X-rays is discussed. Moreover, the concepts of electron-matter interaction and scattering theory are included. Since TEM has been used for all the experimental work covered in this thesis; the discussion is focused on this technique, and other well-known electron-based tools like STEM, SEM, STM are not included. Section 2.3 deals with a detailed explanation of working of a TEM. Furthermore, the practical aspects linked to transmission electron microscopy such as resolution, contrast, and electron beam damage are also discussed. As mentioned in chapter 1, different characterization techniques have specific specimen requirements; for instance, in cryo-EM, the samples must be plunge-frozen. Therefore, an essential aspect of transmission electron microscopy is knowing the requirements of an ideal specimen beforehand. The author has described this in section 2.4.

2.1 Overview of liquid-phase transmission electron microscopy (LPTEM)

Liquid phase transmission electron microscopy (LPTEM) emerged as a way to observe samples in their native environment while avoiding the need for thin sections, staining, or vitrification [63], [64]. This technique involves encapsulation of a thin liquid specimen layer between two electron-transparent windows typically fabricated from amorphous silicon nitride [65]. The author has described details about the silicon cleanroom technology and how it is used to manufacture silicon nitride/silicon liquid cell in chapter 3. Liquid cell configurations

are routinely used in material science to study growth and etching of metal nanoparticles [66], [67]. Observing the growth process, in particular, is vital in realizing the desired conditions for nanocrystal synthesis [68]–[71]. The liquid cell also finds application in tracking the motion of nanoparticles in solution, and these studies are required to get a hold of the physics that dictates nanoparticle motion in solution [72]. In this respect, Zheng *et al.* reported microscopic details of nanoparticle motion as the fluid evaporates [68]. Later, in 2013 Muller *et al.*, captured the movement of gold nanorods in a flow cell [57]. In the same year, Chen *et al.* demonstrated the 3D motion of DNA-gold nanoconjugates in a graphene liquid cell, using double stranded DNA [73]. In a similar study, Keskin *et al.*, in the year 2015 showed that the motion of gold nanoparticles in DNA-gold conjugate was dictated by hybridization process of single stranded DNA molecules [74].

Another direction in which LPTEM has shown promising outcomes is the self-assembly of nanomaterials. Thorough knowledge of the essential mechanisms in the assembly processes may help in the large-scale production of nanoparticle arrays required for a suitable device architecture [72]. In this regard, Park *et al.* reported the possibility of forming an ordered nanoparticle superlattice from their random distribution by the capillary forces and local solvent fluctuations [75]. Self-assembly of gold nanoparticles coated with positively charged CTA^+ and negatively charged Cl^- in solution was shown by Liu *et al.* [76]. In-liquid imaging also finds application in studying the electrochemical processes, which are essential for batteries and other energy storage devices [54], [77]–[79]. Holtz *et al.* investigated the lithium-ion transport kinetics and degradation mechanism in $LiFePO_4$ [80].

Imaging of biological specimens under physiological conditions is a major scientific challenge, key to understanding living system, that is being addressed by several research groups using LPTEM. Diana *et al.* utilized flow cell to successfully image fixed mammalian cell with nanometer resolution [63]. Huang *et al.* used a self-aligned wet cell for bacterial cell incubation and obtaining its snapshots in a damp environment in TEM [81]. Mirsaidov *et al.*, successfully imaged acrosomal bundles in water in a bonded or self-contained liquid cell and obtained 2.7 nm spatial resolution [82]. Varano *et al.*, for the first time, presented time-resolved movies of motion of individual biological complexes (rotavirus) moving in liquid [83]. Later, in 2017 Besztejan *et al.*, demonstrated sub-cellular structures in fixed and non-fixed PC3 cells [64].

To sum up, so far this technique has helped in extending the imaging modalities beyond the limits of optical microscopy and has proved especially beneficial for the molecules which

7

cannot be labelled or stained [72]. In practice, however, effects such as bulging of the silicon nitride windows, and excessive background scattering from thick (50 nm) silicon nitride make it challenging to achieve high contrast and resolution from weakly scattering organic specimens [84]. The motivation behind this thesis work is to resolve some of these challenges and contribute to this intriguing area of science. In the next four sections of this chapter, the author constructs a theoretical outline for the experimental work presented later in this thesis.

2.2   Electrons as a probe for real-space imaging and diffraction

Electrons can be used as a probe to investigate the structure and dynamics of inorganic, organic and biological materials at the atomic level. Electrons being charged particles get scattered by the Coulomb potential of the atomic nucleus. Therefore, the scattering cross section of electrons is 10^6 to 10^7 larger than matter compared to hard X-rays, which are scattered by photon-electron interaction with the electronic orbitals. This strong interaction gives electrons a fundamental advantage over X-rays as the scattered electron beam is comparatively more intense with respect to scattered particles at the detector plane and carries direct information for the position of atoms in a specimen. The higher scattering cross-section makes them more suitable for studying the molecular structure of liquid and gaseous samples [85]–[88].

Two basic requirements to be able to use electrons as a probe are the application of sufficient electron dose required to form an image at the desired resolution, and a specimen with a thickness that is no more than a few times the elastic mean free path of electrons at the relevant energy [29], [89]. The radiation sensitivity of the specimen of interest dictates the maximum allowed electron dose. If the sample is radiation hard (e.g. metal nanoparticles), a high electron dose can be used. In case of specimens prone to radiation damage such as organic or biological samples, lower dose values should be applied. Matters of resolution and contrast in the TEM and how they are affected by electron beam induced damage is discussed in sections 2.3.1 and 2.3.2. The author further illustrates the application of these in chapter 5, in quantifying the data obtained using the ELC TEM method. Specimen thickness, typically required to be at most a few times of the mean free path of electrons in the material under study, can be easily achieved for solid samples. However, this becomes challenging in case of liquid and gaseous samples. The standard tools which utilize electrons as a probe are transmission electron microscopy (TEM), scanning electron microscopy (SEM) and scanning transmission electron microscopy (STEM). Regarding the present thesis work, all imaging and diffraction were done on a transmission electron microscope (TEM), and therefore discussion throughout this chapter is centered around this technique.

To better understand the effects of probing matter with electrons, some theory regarding electron matter interaction and scattering theory are included here. The exposure of matter to high energy electrons leads to many possible interactions, see Figure 2.1. These can be broadly classified into two categories: elastic and inelastic interactions [90], [91]. In the case of elastic interaction, no energy is transferred to the specimen. Here, electrons can either pass without any interaction (direct beam) or they can get scattered by the electrostatic attraction of the positive potential inside the electron cloud. The signal coming from such interaction is mainly utilized in TEM and electron diffraction. Diffracted electron waves which are scattered by the atomic potential form diffraction patterns on the back focal plane. These patterns can either be in the form of bright spots or as diffused rings depending upon the crystallinity of the sample. Liquid Specimens, where long-range ordering is absent, give rise to diffuse diffraction patterns.

In the case of inelastic interaction, energy is transferred from the incident electrons to the specimen. Such interactions produce secondary electrons, phonons and cathodoluminescence. Furthermore, ionization of atoms by removal of inner-shell electrons results in the emission of X-rays and Auger electrons. Signals arising from this type of interaction are exploited in analytical electron microscopy. Secondary electrons are used in scanning electron microscopy (SEM) as the primary signal. They are also useful in constructing high-resolution images of the specimen surface in scanning transmission electron microscopy (STEM).

The notion of scattering cannot be fully understood without a mathematical explanation, and therefore the author describes the idea of scattering in terms of the scattering length. These have implications in chapter 6. The amount of scattering in the direction of the solid angle Ω is $f(\Omega)$. The quantity f is the scattering length, which indicates the normalized scattering flux $\Delta\sigma$ (Ω) for a solid angle $\Delta\Omega$ in the direction Ω, for unit incident wave flux density:

$$\Delta\sigma = |f(\Omega)|^2 \, d\Omega \qquad\qquad 2.1$$

The total scattering cross-section is obtained by integrating equation 2.1 and is given by

$$\sigma = \int |f(\Omega)|^2 \, d\Omega \qquad\qquad 2.2$$

The fundamental physics of scattering of electrons from matter is the same as that for X-rays, the only significant difference being the strength of scattering, which is higher for electrons. Due to the similarity between the two, the scattering cross-section for electrons can be directly deduced from that of X-rays. In the Schrodinger equation or the electron wave equation, the scattering intensity from point r is determined by the potential function at that point V(r). Therefore, the scattering form factor is given by

$$f(Q) = \frac{2m_e e}{\hbar^2} \int_0^\infty \frac{V(r) Sin(qr) r^2}{q\, r} dr; \qquad\qquad 2.3$$

where m_e is the mass of the electron, e is the electronic charge, and $\hbar$ is the Planck's constant [92]. The interaction between electrons with matter can also be described using the concept of the mean free path (mfp). After traversing one mfp, a fraction of 1/e of the electrons remain unscattered on average. If the mean free path of electrons in a material/specimen under investigation is known beforehand, the thickness of the sample can be tuned to avoid multiple scattering. However, it is not always possible to optimise the specimen thickness to get rid of the multiple scattering completely; in fact, it is very challenging for specimens in liquid. In Chapter 5 and 6 of this thesis, an approach developed by the author to control the liquid layer thickness is described. Additionally, the problem of multiple scattering in handling electron scattering data on liquid water has also been illustrated in chapter 6.

Mathematically, the mean free path is given by the following equation,

$$L = \frac{W}{\sigma\, \rho\, N_A} \qquad\qquad 2.4$$

where ρ and W are the density and atomic weights of the sample layer, and N_A is Avogadro number. The cross-section σ is the sum of inelastic and elastic contributions [93], [94].
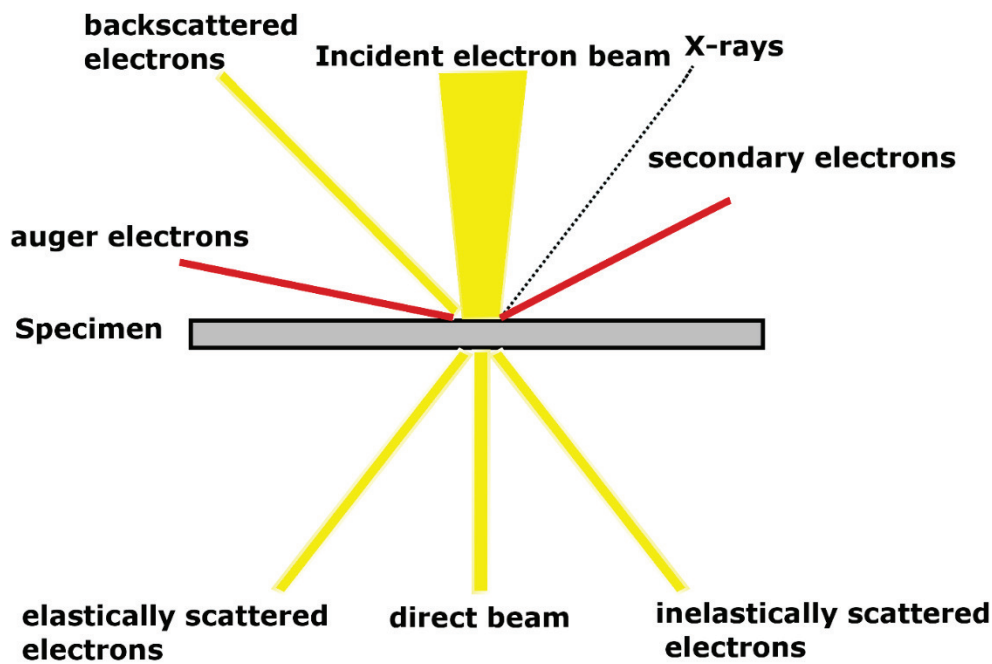
Figure 2.1 Important interactions between an electron beam and a specimen

2.3 Transmission electron microscope (TEM)

Electron microscopes are tools utilised to inspect the ultrastructure of an extensive range of biological and inorganic samples including microorganisms, cells, large molecules, metal nanoparticles and crystals. The idea of an electron microscope followed from the groundbreaking discovery by Louis de Broglie that electrons have wave-like properties. The term was first used in the celebrated publication of Knoll and Ruska (1932) [95]. Seven years later, the first commercial TEM was developed by Siemens AG [96]. The technology has seen some significant modification since that time and is still being improved. Currently, state of the art systems developed by JEOL, FEI, and Hitachi are available with a resolution as good as 0.05 nm.

In a TEM, the transmitted electrons from the specimen form the signal. It can be operated in two different modes, bright field, and dark field. In the bright field mode, the unscattered or transmitted electrons are allowed while the scattered ones are blocked. Therefore, the areas (specimen) with high mass-thickness appear dark as opposed to the bright background. On the other hand, in dark field mode, the unscattered beam is blocked, and only scattered electrons are selected. Consequently, the specimen which has a higher mass thickness appears brighter as compared to a dark background. Bright or dark field images can be obtained in a

TEM with a magnification in the range × 1000–×100,000 or greater by adjusting the lenses of the microscope [93], [97].

Samples can be inorganic, organic or biological and can be imaged in the solid, liquid or frozen state. Inorganic solid samples, like metal nanoparticles dried on a TEM grid, are the simplest of all and require no additional care such as staining or vitrification. Organic and biological specimens are delicate and need either liquid or frozen state to keep their structures intact. In material science, the research is mainly focused on inorganic materials, and atomic resolution has been achieved already. For the other two types of samples, cryo-EM (cryo-electron microscopy) has been used to obtain atomic resolution using single particle methods [98]–[100]. LPTEM is another technique to capture organic and biological structures and processes. Unlike cryo-EM, here the specimens are imaged in their native liquid state. Atomic-resolution has been achieved with LPTEM for metal nanoparticles but not for the organic/biological specimen, as they have poor mass thickness contrast and are sensitive to electron beam induced damage [101]. For such cases, single-particle ensemble averaging can be performed where large (10^4) number of poorly resolved particles can be averaged to acquire atomic-level information [102]–[105]. In section 5.5, an illustration has been made with ferritin molecules of how ELC TEM can be used to collect such a large number of particles in a stable liquid environment. Moreover, in appendix 2 the author presents the challenges in repeating the same with T7 virus and gold-labelled antibodies. A TEM can be operated both in imaging and diffraction modes. Diffraction modes can also be used to get structural information either from crystalline or amorphous specimens [93], [97].

A TEM can be broadly classified into three essential sections: (1) an electron gun for electron beam generation and a condenser system which focuses the beam onto the object, (2) the image-producing system, this consists of an objective lens, movable specimen stage and intermediate and projector lenses and (3) image-recording system, which converts the electron image into a form noticeable by the human eye. This system is equipped with a fluorescent screen (for viewing and focusing) and a digital camera (for permanent records). In addition to these, a vacuum system involving pumps, gauges valves, and power supplies is also present [106].

The three different types of electron sources used in TEM are thermionic, Schottky and field-emission source. Table 1 presents the different types of electron sources available in terms of the material, current density, brightness, adequate source size, and energy spread. A thermionic source is made up of either tungsten or lanthanum hexaboride (LaB_6) and emits

when heated to high temperatures (2700 K for W and 1400-2000 K for LaB6) using a direct current. This process is called thermionic emission. The heating of the LaB_6 crystal is done by passing a current through wires between which the crystal is mounted, causing thermionic emission. Electrons emitted from the cathode are accelerated towards the anode by applying a high voltage between the emission source and the anode plate.

Type of Source	Tungsten thermionic	LaB₆ thermionic	Schottky emission	Cold field-emission
Material	W	LaB_6	ZrO/W	W
Current density (j_e) in A/m²	$\approx 10^4$	$\approx 10^6$	$\approx 10^7$	$\approx 10^9$
Reduced Brightness (β) in Am⁻²sr⁻¹V⁻¹	$\approx 10^5$	$\approx 10^6$	$\approx 10^7 - 10^8$	$\approx 10^8 - 10^9$
Effective source size (d_c) in μm	≈ 40	≈ 10	≈ 0.02	≈ 0.01
Energy Spread (ΔE) in eV	1.5	1.0	0.5	0.3

Table 1: Operating parameters of four types of electron source (taken from reference [91])

The second type of source used is the Schottky thermal field emission source. Here, the potential barrier of the emitter is reduced by the application of a strong electric field which in turn eases the emission of thermionic electrons. Finally, the third type of the source used is field emitter, which has an extra-fine tip (<100 nm) for electron emission and two different anode plates. The function of the first anode plate is to deliver low voltage for the extraction of electrons from the tip while the second anode accelerates the produced electrons up to the set energy, typically in the 80 - 300 keV range. This type of source has a small beam diameter, and higher current density compared to the other two and is therefore well suited for applications such as high-resolution phase-contrast microscopy and electron holography [91]. A thermionic

Sana Azim   Hamburg, 2020

LaB$_6$ source equipped (JEM 2100, JEOL) TEM has been used for all the imaging and diffraction results in this thesis, as unlike the other two it does not have very stringent vacuum requirement, an essential prerequisite for conducting liquid cell measurements. Additionally, it can deliver higher total current than Schottky and field emission sources, thereby allowing for a large field of view at high current density, albeit lower coherence. The latter is most essential in case of phase-contrast imaging, but relatively unimportant for mass contrast imaging.

The operation of a LaB6 TEM is now described, which differs from a FEG TEM mainly in the gun design and vacuum system, the remaining electron optics and the camera system are similar. Right after the electrons are emitted from the source, they first pass through a cross-over point by the first electrostatic lens (Wehnelt cap) and then go through a series of electromagnetic lenses namely the condenser lenses, the objective lenses and the projector lenses, see Figure 2.2. A customized magnetic field from these lenses is formed to manipulate the electron beam coming out of the LaB$_6$ source [107]. The focus and magnification of the electron beam are as well managed by tuning the strength of these lenses.
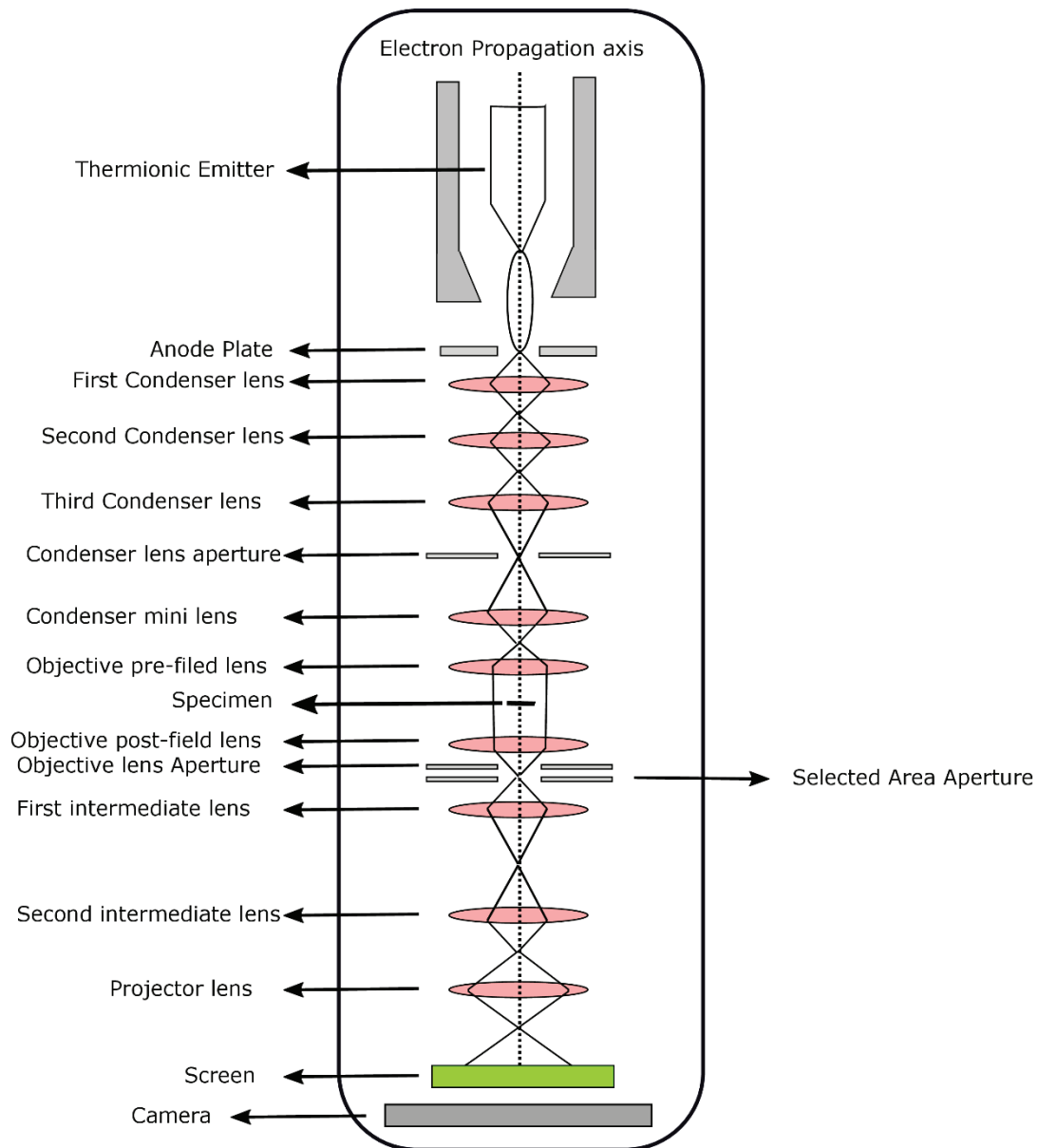
Figure 2.2 Schematic of a bright-field TEM

Elaborating the functionalities of these lenses, a condenser lens collects the electrons of the first crossover image and focus them onto the sample so that only area being examined is illuminated. The purpose of an objective lens is to focus and initially magnify the image. Intermediate lenses magnify the image coming from the objective lens, and finally, the projector lens further magnifies it and projects it on to the phosphor screen. In addition to the lenses, the TEM column is also equipped with apertures which are defined as circular holes in metal disk typically made from platinum or molybdenum [97]. Three different apertures are present within the TEM column condenser aperture, objective apertures and selected area aperture. The

diameter of these apertures is important; for instance, the condenser-aperture determines the size and divergence angle of an electron beam, while the scattering angle of an electron exiting from a sample is determined by the objective aperture. The selected area aperture is used to regulate the area from which a diffraction pattern is obtained [93].

Lenses and apertures together are used to control the divergence or convergence of the electron beam, brightness of the beam on the specimen, as well as angle and spot size of illumination. The quality of the image formed depends on the overall alignment of the lenses. Quadrupole lenses are used as stigmators which can compensate for axial astigmatism. Aberrations due to magnetic lenses and apertures affect the resolution. The details about these aberrations will be discussed in the next section.

After a discussion has been made about image formation, it is also crucial to describe the detection and collection of the image/diffraction patterns. Cameras coupled to scintillators are commonly used for this purpose. Two such cameras are charged coupled device (CCD) and complementary metal oxide semiconductor (CMOS). Both of these uses a scintillator, typically single crystal phosphors, to convert electrons to photons which are then transferred to their sensor through a fiber optic plate [97]. There are two points of difference between CMOS and CCD, which make the former superior to the latter. The first one is that CMOS cameras are less susceptible to blooming, spreading of the charge from an oversaturated pixel to nearby pixels. The second is that they have a faster readout speed compared to CCD cameras. The use of scintillators for electron to photon conversion decreases the detective quantum efficiency of CCD and CMOS cameras. This is why many TEMs now incorporates direct detectors which are directly exposed to the electron beam and therefore have a higher detector quantum efficiency [108].

The TEM camera used for all the work done in this thesis is the TVIPS TEMCAM F216, which is based on CMOS technology with active pixel sensors. It is a 4-megapixel camera and covers an image area of 32×32 mm^2, and it has a 72% fill factor and a read-out speed of 2×10 megapixels/sec @ 16 Bit. The signal-to-noise ratio for a single electron is 14:1 for 120 kV and 12:1 for 200 kV.

2.3.1 Resolution and contrast

Resolution is defined as the ability of a microscope to resolve two closely spaced objects [109]. From the classical Rayleigh criterion for visible light microscopy, the resolution is diffraction-limited and is given as

Sana Azim   Hamburg, 2020

$$\delta = \frac{0.61\,\lambda}{\mu\,Sin\beta} \qquad\qquad 2.5$$

Here λ is the wavelength of the radiation, μ is the refractive index of the viewing medium, and β is the semi-angle of collection of the magnifying lens [110], [111]. The term $\mu Sin\beta$ is called the numerical aperture, and this is an essential concept in microscopy as it determines the resolving power of a lens. In the case of optical microscopes, the numerical aperture can be set to unity, which gives δ (resolution) equal to half the wavelength of light, using equation (2.5). For instance, the wavelength range of the visible spectrum is 400-700 nm. If we take $\lambda = 400$ nm, a resolution of 200 nm is obtained, the limit of resolution for light microscopy. The practical resolution for a light microscope is about 300 nm [91]. With developing optical technologies like fluorescence microscopy, however, the resolution limit of these microscopes has been pushed to tens of nanometers for suitable specimens using super resolution methods [112].

Resolution in case of high energy electrons (100-300 kV) is not diffraction-limited. Instead, it is limited by lens aberrations (chromatic and spherical), signal-to-noise-ratio, and stability of the specimen under investigation. The typical value of resolution obtained in a TEM is 0.2 nm. Spherical aberration becomes dominant for the case of ultra-thin samples. Due to this type of aberration, electrons travelling at a larger angle to the optic axis are focused more strongly than those moving closer to the axis. In LPTEM, the spherical aberration only applies to a few cases such as the graphene liquid cell. For such cases, optimizing the objective lens angle (α) will give a point resolution (d_S),

$$d_S = C_S\alpha^3 \qquad\qquad 2.6$$

where C_S is the coefficient of spherical aberration and has values in the range 1-2 mm. If the spherical aberration is corrected, a resolution value below 0.08 nm can be achieved. The typical spatial resolution for the uncorrected 200 keV TEM is 0.24 nm [89], [111].

The second type of aberration which limits the image resolution in a TEM is chromatic aberration. It is caused by focusing of different wavelengths of electrons to varying distances from the lens. It becomes dominant when the TEM has a high energy spread (ΔE) or works at a low accelerating voltage (E). The factors affecting the energy spread of electrons that form the image are lens instabilities, intrinsic properties of the electron source used and inelastic

Sana Azim   Hamburg, 2020

scattering from the specimen under investigation. The image resolution for the cases where chromatic aberration dominates is given by

$$d_C = \alpha C_C \frac{\Delta E}{E} \qquad\qquad 2.7$$

Where d_C is the chromatic blur which gives the image resolution, and C_C is the coefficient of chromatic aberration [111].

In addition to the two aberrations, another factor affecting the image resolution in TEM is astigmatism. Electrons passing through the column of the microscope can get exposed to an inhomogeneous magnetic field which may arise due to lens imperfections. These inhomogeneities lead to astigmatism and can be corrected by using a compensating field which is introduced in the microscope by using stigmators.

Specimens studied in solution like organic polymers or biological macromolecules are more sensitive to the electron dose than inorganic, hard, materials. In case of these samples, the image resolution is dominated by electron dose rather than the aberrations. Due to the presence of statistical noise, an object can only be detected in an image if the corresponding pixels have a signal level above the background counts such that the signal-to-noise ratio (SNR) is greater than a value of 3-5 [89], [113]. When imaging an object in liquid, the statistical fluctuations are caused by the background scattering from liquid, and detector noise is insignificant. The SNR in the image is given by

$$SNR = DQE^{1/2} C \langle I \rangle^{1/2} \qquad\qquad 2.8$$

Where *DQE* is the detector quantum efficiency, $C = |\Delta I|/<I>$ is the image contrast, and $<I>^{1/2}$ is the noise level [89], [111]. These concepts of resolution have been used to quantify the image quality in chapter 5 of this thesis.

The contrast C in a TEM as explained above is defined as the difference in intensities of a point corresponding to an object with respect to other areas like background and is given by

$$C = \frac{I_2 - I_1}{I_1} \qquad\qquad 2.9$$

where I_2 and I_1 are the intensities of the object and background, respectively. The contrast in a TEM has two main contributions, amplitude contrast and phase contrast. The variation in the mass or thickness of a specimen changes the electron-matter interaction, giving rise to amplitude contrast given by

$$C = 1 - e^{-Q\Delta t} \qquad\qquad 2.10$$

Where Q is the total elastic scattering cross-section and Δt is the change in the specimen thickness [93].

When an electrons pass through the specimen of interest, they are scattered away from the axis by elastic nuclear interaction (Rutherford scattering). The elastic scattering cross-section is a function of the atomic number (Z) of the specimen, and it increases with increasing specimen thickness as the mean free path is constant. This implies regions of the sample with higher Z will scatter more electrons than the ones with lower Z, provided they have the same thicknesses. On the same note, thicker areas of the specimen will have more scattering than thinner regions having the same average Z. When it comes to image interpretation, two different modes exist: bright field and dark field. In the bright field mode, areas with higher Z or thickness will appear darker than thinner or lower Z areas. The opposite holds for the dark field images. Another essential thing to note is that the images obtained from a TEM are the two-dimensional projection of the three-dimensional objects and therefore, should be analyzed keeping this mind [93].

In TEM imaging of amorphous materials like polymers or biological specimens, mass-thickness contrast is the primary contrast mechanism and can be enhanced by either shadowing or heavy-metal staining. The author has provided a short description of the staining method in section 2.4. In chapter 8 of this thesis, the author has utilized the negative staining technique to study the aggregation behaviour of small protein (γS-crystallin) which was otherwise not possible with LPTEM due to inferior mass-thickness contrast.

The second contrast mechanism, which is phase contrast, arises from the interference of the scattered and unshattered electron waves. Electrons, after getting scattered from a specimen, undergo a phase shift ($\varphi(r)$) which is related to the specimen potential by the following equation

$$\varphi(r) = \int_0^{t(r)} aV_t(r)\, dz \qquad\qquad 2.11$$

where a is the interaction constant, $V_t(r)$ is the projected potential of the specimen, $t(r)$ is the local thickness of the TEM specimen, and the electron beam is travelling in + z-direction [114]. The projected potential $V_t(r)$, which is obtained from holography measurement is related to the mean inner potential V_0 of a specimen by the following relation,

$$V_0 = \frac{1}{A} \int V_t(r)\, dA \qquad\qquad 2.12$$

where A is the area of a projected specimen. Most of the biological macromolecules are made up of carbon and hydrogen which have low inner mean potential and therefore have a small phase shift resulting in weak phase contrast [115]. The quantification of the amount of phase signal being transmitted to the real space wavefunction in the image plane is done using the contrast transfer function (CTF). The form of the CTF determines the quality of real space images in a high-resolution TEM (HRTEM). In a regular TEM, the defocus contrast can be used to enhance the image quality slightly [116].

Another way to increase the phase contrast in TEM images is by using a phase plate at the back focal plane. Phase plates have shown a significant increase in the contrast of biological specimens and are a promising candidate for performing liquid phase microscopy of biological macromolecules [117]–[121]. Despite the promising phase enhancement, they are not very popular, which is due to existing drawbacks such as short lifetime, and lack of hardware and software support [120], [122]–[124].

2.3.2 Electron beam damage

Electron beam damage is caused by either elastic scattering of incident electrons from atoms or inelastic scattering from atomic electrons or a combination of both. Based on these, the different mechanisms of electron beam damage are Knock-on damage (for elastic beam-atom collision), radiolysis (for ionization) and heating [93]. Elastic scattering of primary electrons where the energy is directly transferred to an atomic nucleus gives rise to knock-on damage. The amount of energy E being transferred, depends on the angle of scattering (θ) and is given by,

$$E = \frac{E_{max}}{2}(1 - cos\theta) \qquad\qquad 2.13$$

where E_{max} is the maximum possible energy exchange corresponding to $\theta = 180°$. The threshold incident energy below which no knock-on damage occurs is given by

$$E_0^{th} = 511 \ keV \left\{ [1 + \frac{AE_d}{561 \ eV}]^{1/2} - 1 \right\} \qquad\qquad 2.14$$

where A and E_d are the atomic weight and bulk or surface displacement energy of the scattering atom [93], [125]–[127]. For most of the elemental solids, this threshold is above 200 keV for bulk displacement but below 200 keV for surface sputtering. This threshold can go even below 100 keV for many low-Z atoms, and it is for this reason that low voltage TEMs have been developed. For instance, demonstration of atomic-scale imaging by the aberration-corrected TEM operating at 40 and 20 keV [127]–[129].

The electronic excitation and ionization cause radiation damage in liquid or frozen specimens in a process known as radiolysis. It results in the formation of radical and molecular species such as hydrated electrons (e_h^-), hydrogen and hydroxyl radicals ($H \bullet$, $OH \bullet$) and hydrogen molecules (H_2) upon decomposition. The radicals formed are chemically reactive, and they recombine to create a series of highly reactive species, known as primary products, as given by the following relationship [111], [130], [131]

$$H_2O \rightarrow e_h^-, H \cdot, OH \cdot, H_2, H_2O_2, \ H_3O^+, HO_2 \cdot \qquad\qquad 2.15$$
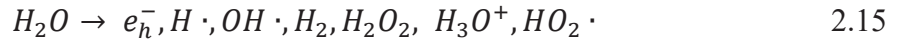
The damage caused by radiolysis is a result of energy transfer from inelastic scattering. The intensity of radiation is measured by the amount of energy deposited in the sample. It is given in units of gray (absorption of 1 joule of radiation energy per 1 kilogram of matter) [130], [132]. The absorbed energy in radiolysis is proportional to the energy deposited per unit volume of the specimen. The average energy deposited in a sample with thickness t where multiple scattering is present is given by $<E> = (t/L_i) \ E_m$, and E_m is the average energy loss per inelastic event, with L_i being the mean free path for all inelastic scattering events. Damage due to radiolysis can be reduced in several ways. These include making use of low dose techniques like avoiding any pre-irradiated area or by sampling multiple copies of the structure being investigated at low dose and averaging to get sufficient SNR for image reconstruction. The damage can also be decreased by continuously replenishing the specimen by flowing samples through a jet or a nanofluidic liquid cell [133]–[135]. Maximizing the signal by using contrast enhancer (stain) can also help to keep the radiation damage low [136]. Lowering the specimen

temperature increases the critical dose and therefore, as well reduces the radiation damage for a given intensity [137]–[139].

The damage caused by heating from the beam is a consequence of energy transfer from the electron beam to the specimen via the electron-phonon coupling. It can be minimized by reducing the incident electron beam current [126], [127], [140]. Electrostatic charging is another factor that causes electron beam damage and can be lowered by coating the substrate with materials such as carbon or graphene [141], [142]. Most of the specimens studied with TEM in this thesis are organic and therefore are sensitive to radiolysis. In chapter 5, the radiation damage in polystyrene particles and how working at low doses can reduce it has been shown.

2.4   Specimen requirements for transmission electron microscope

The required thickness of a specimen for successful imaging in a TEM strongly depends on the electron energy and the average atomic number of the sample. As stated in section 2.3.1, it should be at most a few times the mean free path of electrons at a particular energy. However, for the high-resolution TEM imaging, phase contrast is essential, and it requires the thickness to be less than the elastic mean free path of the electron [97]. Traditionally TEM is used with solid specimens because handling liquid and gas samples in the high vacuum of TEM is difficult. Preparing thin solid specimens for TEM can be done via different methods. A few of these are thin-film drop-casting, ultramicrotomy of soft matter bulk specimen, and focused ion beam (FIB) milling of samples. Soft matter specimens with low inner mean potential have poor mass thickness and phase contrast and therefore require either heavy metal staining or a phase plate to be imaged. The author has used drop-casting and negative staining to unravel aggregation pathways of human γS-crystallin protein. Therefore, a short description of the method has been provided in section 2.4.1.

The central theme of the present thesis is to capture the structure and dynamics of biological/chemical macromolecules or particles in their native state, which is otherwise not possible by any of the methods mentioned above. As stated in the first section and also in the introduction chapter, liquid cells are used for that purpose. Therefore, in section 2.4.2, the author provides insight into different approaches of performing LPTEM. Later, a concise introduction to the liquid cell used in this thesis work is given.

2.4.1 Thin-film drop-casting and heavy metal staining

There are smaller protein or other biological molecules which have poor mass-thickness contrast. Such samples are usually imaged via thin-film casting in combination with heavy metal staining. The sample of interest is taken in solution form and is drop-casted onto TEM grids. These grids have a very thin (2-20 nm) layer of carbon on top. Since carbon is a hydrophobic material; it is treated in the plasma or glow discharge chamber before dispensing the sample. The last step ensures that the drop-casted sample spreads evenly onto the entire surface of the grid. This step is followed by staining of the sample to enhance the mass-thickness contrast. Heavy metal salts such as uranyl acetate, ammonium molybdate and phosphotungstic acid can scatter electrons strongly. Therefore, these can be used as a stain or contrast enhancer. They can either be applied to the biological specimens directly (positive staining) or the grid background (negative staining) [143].

The procedure is straightforward, depending on the type of staining. In the positive staining technique, the molecules or objects are stained against a light background [144]. In the case of negative staining, the stain is applied to the background, which then appears darker compared to the molecule of interest [145]. The following is the procedure to prepare negatively stained samples. After applying the sample solution onto the grid, it is blotted and, in some cases, washed in deionized water. The washing is done to avoid salt crystallization as the solution dries on the grid. At this point, approximately 2-4 µl of 1% stain solution is applied, blotted and washed [146]–[148]. The negative stain TEM has been utilized by the author to study the aggregation mechanism in human γS-crystallin proteins, and this forms the basis of chapter 7.

2.4.2 Handling liquid specimens in TEMs: nanoscale liquid cells

Liquid samples are difficult to handle as they evaporate in the high vacuum of a TEM specimen chamber. Therefore, they require a unique device for encapsulation, called a liquid cell. Different materials like stoichiometric and non-stochiometric silicon nitride, hexagonal boron nitride and graphene have been tested for making liquid cells [103], [142], [149], [150]. The current state of art LPTEM allows atomic resolution imaging of metallic nanoparticles [104], [151]–[153]. In-liquid imaging of soft matter and biological macromolecules poses challenges due to poor mass thickness contrast and low tolerance to beam-induced damage [66], [82], [83], [154].

LPTEM can be performed by using various approaches. The three important ones are, a hermetically sealed static and flow liquid cell, graphene liquid cell, and open or environmental

cell. In a hermetically sealed approach, the liquid specimen is sealed between electron transparent silicon nitride windows fabricated on a silicon support. The windows are separated by a thin (80-200 nm) spacer [57], [64], [74]. In a hermetically sealed static cell, the sample is placed on to the liquid cell chip which is then mounted into the sample transfer arm and finally imaged under a TEM [64], [74]. This technique has ease of use and requires small sample volume; therefore, it can be used with precious samples. The drawback linked to this approach is no *in situ* sample exchange which is a highly desired capability for beam sensitive samples to reduce radiation damage [155]. Beam sensitive protein samples, for instance, can easily get damaged after being imaged [74], [76]. Alternatively, a liquid cell with flow capabilities allows sample/buffer exchange *in situ,* but controlling the pressure fluctuations due to continuous flow is difficult, thus making the liquid cell windows more vulnerable to breakage. The requirement of a large sample volume can also be an issue depending on the inner diameter and length of the connecting tubes [57], [149], [156].

A graphene liquid cell (GLC) utilizes a single or multi-layer graphene sheet to encapsulate liquid specimen [58], [101]. A GLC has shown significant enhancement in achievable resolution compared to the silicon nitride/silicon-based liquid cells [101], [157]. The downside of this technique is its incompatibility with cleanroom microfabrication. Additionally, simple modifications like flow, heat/cooling, and electric biasing are hard to perform on these cells [72], [111]. Therefore, despite the very promising results obtained from graphene liquid cells, they still cannot replace silicon/silicon nitride-based liquid cells in all applications.

An environmental cell can either be with or without a window. In the window-less environmental cell, the TEM specimen chamber is modified by applying a differential pumping technique. Here, a series of pumps and apertures are used to change the pressure along the column gradually [158], [159]. The main problem linked to this approach is not being able to achieve atmospheric pressure. Because of this, most solvents such as dichloromethane, isopropanol or water are incompatible with it [159]. In spite of this, a few LPTEM studies were successfully performed using this approach [160], [161]. A windowed environmental cell, on the other hand, utilizes two electron transparent membranes separated by a large spacer and can, therefore, maintain a much higher pressure. The exchange of fluid and different gases is facilitated by external tubing to which an air/fluid reservoir is connected to one end while the other end is connected to a vacuum pump to adjust the pressure [162]. The author has utilized this very same idea and incorporated it into the latest microfabricated liquid flow cell

technology to develop a new environmental liquid cell, which is discussed at length in chapter 5. The detailed fabrication protocol has been discussed in chapter 3, while some brief technical details are provided hereafter.

The liquid cells used are silicon nitride/silicon devices which can be used both as hermetically sealed static liquid cell or as a flow liquid cell. The design idea of these cells has been taken from the Miller group while the fabrication was done by SiMPore Inc., USA. These comprise of two parts, top and bottom, each having an outer silicon frame with dimension 3×8 mm and a rectangular window in the centre. The windows are made from a free-standing thin film of non-stoichiometric silicon nitride. The dimension of window is 200x30 μm^2, 200x50 μm^2, 100x30 μm^2 and 100x50 μm^2. Along with the window, 80 nm thick spacer (5400x250 μm^2) made from silicon dioxide is present on the top part. This spacer is fabricated so that it acts as a flow channel. Two flow openings (600x600 μm^2) and two trenches (2550x250 μm^2) are present on the bottom part in addition to the centre silicon nitride window.

A liquid cell holder, designed in-house, is used to mount the assembled liquid cell with fluid specimens. This holder is designed to fit in the goniometer of the TEM and can, therefore, be moved, by moving the stage to adjust the focus. Figure 2.3 illustrates different parts of the liquid cell holder and the liquid cell. Further details about the liquid holder are given in chapter 5, where the development of environmental liquid cells is discussed.
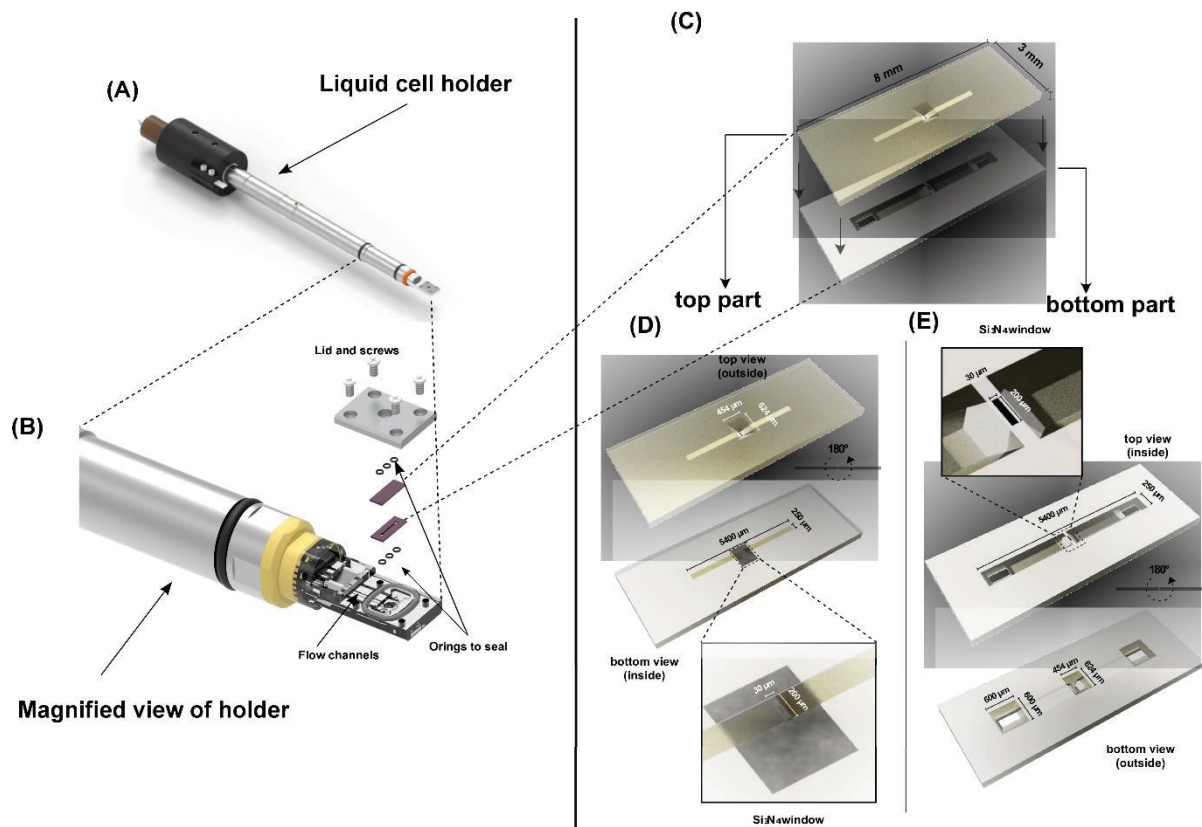
Figure 2.3 CAD renderings, (A) Liquid cell holder, (B) magnified view near the head of the holder, showing flow channels machined for flow. Also, the top and bottom part of liquid cell along with O-rings and lid of the holder is shown. (C) Magnified view of the top and bottom part, (D) outside/inside view of the top part displaying the 45 degree etch in silicon (454×624 μm^2) on the outside which opens a 30×200 μm^2 window on the inside. An 80 nm, 250×5400 μm^2 flow channel is as well shown, (E) shows outside/inside view of the bottom part, displaying 600×600 μm^2 flow openings and two trenches 2550×250 μm^2.

3   Microfabrication

In this chapter, basic microfabrication techniques used in the development of liquid cells are discussed. The design of the nanofluidic chips used in this thesis was originated in the Miller group, and initial fabrication was done at Technical University Hamburg Harburg (TUHH). Later, the same design was produced at SiMPore Inc., USA. As the silicon nitride/silicon liquid cells based on the standard silicon microfabrication techniques such as thin film deposition, photolithography and etching. Therefore, firstly, the author provides a general introduction with special mention to the specific designs used in fabricating the liquid cells. Secondly, the author gives finer details about the cleanroom fabrication of the cells. A detailed description of the same has also been provided in the thesis of Dr. Christina Mueller and Dr. Sercan Keskin [163], [164].

3.1   Introduction to silicon microfabrication

Silicon is the backbone material for microfabrication technology due to its natural abundance, low cost, standard fabrication protocol, wide range tunability of its resistivity, availability of silicon wafers in different thicknesses and sizes, smoothness, flatness and mechanical strength [165]. Single crystal silicon wafers find use in the fabrication of almost all the micro-electromechanical systems (MEMS) devices. For all the microfabrication work presented in this thesis, single crystalline silicon wafers were used. Depending upon the fabrication processes involved, the wafer specifications, such as wafer thickness, diameter, crystal orientation, doping, and resistivity can be optimized using well developed protocols.

In the following subsections (3.1.1-3.1.3), techniques involved in the fabrication of the liquid cell, such as thin film deposition, photolithography, wet and dry etching, bonding and dicing will be discussed briefly.

3.1.1   Thin-film deposition

Thin-film deposition techniques can be broadly classified under two categories based on the nature of deposition used, Physical vapour deposition (PVD) and Chemical vapour deposition (CVD). The former includes a source material that provides the vapour to be coated on the substrate. This vapour is then transferred to the substrate and eventually made to condense on its surface. The two common types of PVD processes are thermal evaporation and sputtering. Sputtering is generally preferred over evaporation due to the availability of a broader range of materials as targets. Additionally, the adhesion of the films deposited via sputtering is

Sana Azim   Hamburg, 2020

better when compared to the thermally evaporated films. Silicon dioxide thin-film, 80 nm, which works as a spacer in the liquid cell, has been deposited on a silicon substrate using sputtering [166], [167].

In CVD, the materials to be deposited are present in the reactor as precursor gases. These gases are activated as a plasma, which diffuses convectively and gets adsorbed on the surface of the substrate, forming a continuous thin film. The byproducts are desorbed and pumped away. In this thesis, non-stoichiometric silicon nitride thin film, which works both as an electron transparent window in the liquid cell and as a hard mask for etching is fabricated using the CVD technique. The quality of the silicon nitride thin film deposited is essential as to some extent it controls the mechanical stability of the liquid cell window. The specifications of the deposited film are governed by the deposition pressure and temperature. Generally, low-pressure CVD (LPCVD) is utilized to obtain better quality (uniformity better than 5%) silicon nitride thin films. In the standard LPCVD process for silicon nitride deposition, the operating parameters are 0.25-2 Torr pressure, 100-1000 sscm (standard cubic centimetres per minute) gas flow rates of the precursor gases and 300-900 ℃ working temperature. Silicon wafer is coated with silicon nitride at around 800 ℃ with the following reaction of ammonia and silane [168]–[173],

$$3SiCl_2H_2 + 4NH_3 \quad \rightarrow \quad Si_3N_4 + 6HCl + 6H_2 \qquad 3.1$$
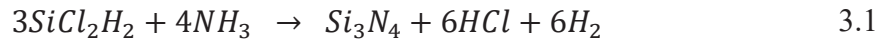
3.1.2 Photolithography

Lithography is a process of transferring patterns of geometric shapes via a mask to a thin layer of radiation-sensitive material called a resist, which is spread onto the wafer or substrate of interest [174]. The type of light source used can decide the minimum feature size and the possible resolution that can be transferred onto the substrate. Integrated circuits for active devices have a requirement of large feature sizes (>1 µm) with high throughput production, and therefore UV-photolithography is generally used for the purpose. On the other hand, electron beam lithography is used when smaller features in the range from submicrometer down to a few nanometers are to be transferred [175].

The two types of optical exposure methods are shadow printing and projection printing. In shadow printing, which can be further divided into contact and proximity printing, the mask and the substrate wafer are in direct contact, this gives very high resolution, R, which can be theoretically given by,

Sana Azim   Hamburg, 2020

$$R = k\sqrt{\lambda\left(s + \frac{z}{2}\right)} \qquad\qquad 3.2$$

where k is a constant with value 1.5, z is the thickness of the photoresist coating, s is the gap between photoresist and mask and λ is the wavelength of the exposing radiation. Using Equation 3.2, for 2 μm thick phot resist, deep UV exposing radiation (~250 nm), s= 0 (contact printing), the obtained resolution is ~0.75 μm. Contact printing is generally used for dimensions between 5-10 μm [176]–[178]. The patterns for liquid cell window, channel, and trenches are large (>5 μm); therefore, contact UV-Photolithography (λ = 365 nm) was used for all the fabrication work in this thesis.

A photoresist is spin-coated on to the surface of the substrate wafer before lithography. Depending on the chemical changes occurring in the photoresist on exposure to ultraviolet radiation, they can be classified into two categories: positive photoresist and negative photoresist. Positive resist is insoluble in the developer solution before exposure. After irradiation, the photosensitive compound in the exposed area absorbs energy which changes its chemical structure and thereby transforms it into a more soluble compound. Therefore, the exposed region becomes more soluble and thus removed more readily in the developing solution [179].

On the other hand, a negative photoresist are polymers combined with a photosensitive compound, when this resist is exposed to radiation the photosensitive compound absorbs the radiation, initiating a chain reaction causing cross-linking of the polymer. The cross-linked polymer has a higher molecular weight and thus becomes insoluble in the developer. Because of this, after the exposure, the unexposed portions are removed [180], [181]. Spin coating of the resist is done in a vacuum chuck, which holds the substrate wafer while the resist is dispensed on it. The substrate is placed in a vacuum on a hot plate after spin coating to get rid of the remaining solvent. The thickness of the photoresist depends on the spinning speed, viscosity, and solution concentration [182]. The photoresist for the fabrication of single window liquid cells used in this thesis, is a positive resist, HPR-504.

The patterns on the masks are generated using AutoCAD systems and then transferred onto the physical masks which are typically made from material such as glass or quartz, which are transparent to deep UV, and covered with an absorbent metallic layer like chromium or iron oxide. Patterns to be transferred on the substrate are present on this layer. Masks can also be

classified into positive and negative variants. A positive mask or dark field mask is one where the patterns are transparent with a dark background, and on the contrary, a negative field mask is one where the patterns are dark with a transparent background. The resolution of the transferred features also depends on the proximity between the substrate and mask. Hence, direct contact masks are used when aiming for higher resolution. However, the longevity of direct contact masks is limited and therefore, is not preferred in the industry [183]. AutoCAD was used to design the mask for liquid cell windows channels and trenches, and the physical mask was developed in JD Photo Data, UK. Patterns were transparent with dark (chrome) background, that is a positive mask was used.

3.1.3 Etching techniques

The etching is a common technique used in microfabrication of semiconductor devices to remove selected portions of a wafer to transfer patterns. Etching can broadly be classified into two categories: Wet etching (liquid-based etchants) and dry etching (plasma-based etchants). In wet etching, the unwanted portion from the wafer is removed by immersing the wafer into a tank of etchant solution. The etchant is a chemical solution that reacts with the selected portion and forms soluble by-products. In dry etching, plasma is used to etch the material of interest. This technique is comparatively more accurate than wet etching.

3.1.3.1 Wet etching

The wet etching process involves three main steps: transport of the etchant to the wafer surface, a chemical reaction between the etchant and the exposed surface and removal by diffusion of the by-products formed. The etch rate for the wet etch process is defined by the slowest of the three stated above, the so-called rate-limiting process. The shapes of the etching sidewalls are determined by the orientation of the etched materials and etching conditions. Based on this, there are three types of etched sidewall shapes: rectangular, positive sloping and negative sloping. Diffusion-limited etching produces sloping edges, but it is not desirable as it results in trenching issues. Wet etching of polycrystalline materials like silicon is anisotropic because the etchant (KOH) shows an etch rate selectivity 400 times higher in the <100> direction over the <111> direction. A cavity with a trapezoidal cross-section is created due to anisotropic wet etching of silicon wafer. The bottom of the cavity is the {100} plane while the sides are {111} planes. The SiO_2 layer is etched using a buffered oxide etch (BOE), and the underlying Si layer is etched with KOH. The sidewalls of the developing structure are inclined at θ= 54.74° to the surface. In Figure 3.1, the structure of anisotropic etching is shown.
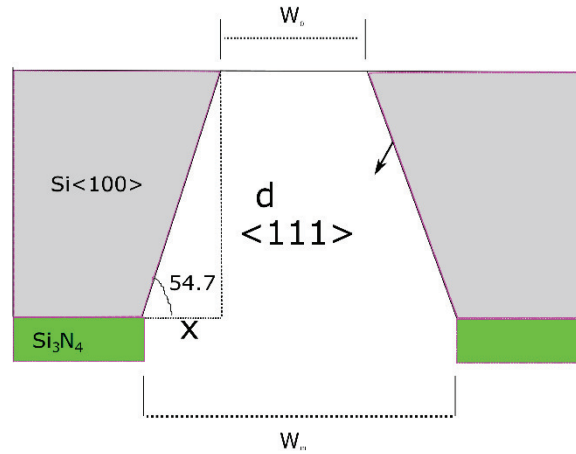
Figure 3.1: Etched Structure of Si<100>

$$x = \frac{d}{tan\theta}$$

3.3

where x is the horizontal component, and d is the wafer thickness. Since $\theta = 54.74°$, the value of x can be calculated to find the dimension for the etching window. If a backside etches mask needs to be designed, the backside window dimensions must be defined as:

$$W_m = W_0 + 1.41 \times d$$

3.4

where d is the wafer thickness, or the required etch depth [184].

In this thesis, we have used potassium hydroxide (KOH) to etch Si<100> using silicon nitride as the etch mask. This is due to its slow etch rate in KOH (<1 nm/hr.). Further BOE was used to pattern the silicon dioxide film.

3.1.3.2 Dry etching

Dry etching is the most widely used etching method; it can create feature sizes smaller than 100 nm and is highly anisotropic. This etching process either works by using chemically reactive gases and plasma or by physical methods such as sputtering and ion beam induced etching. Dry etching, where a combination of two is used, is known as reactive ion etching. The mechanism of dry etching involves introducing a feed gas into the chamber where the gas breaks down and forms a plasma, which then diffuses to the surface of the thin film and gets adsorbed.

The adsorbed plasma reacts with the film etching away the unwanted portion, thereby forming the desired pattern.

In the final step, the by-product desorbs from the surface and diffuses away by the stream of gas. The gases used are all fluorine-based. The high selectivity and high etch rates result in vertical sidewalls (high anisotropy) [185]–[187]. Reactive Ion Etching (RIE) can be used to etch tens of microns features with a good aspect ratio [184]. In present work, RIE is used to etch silicon nitride while deep reactive ion etching (DRIE) is used to pattern structures in 100 µm thick silicon wafers.
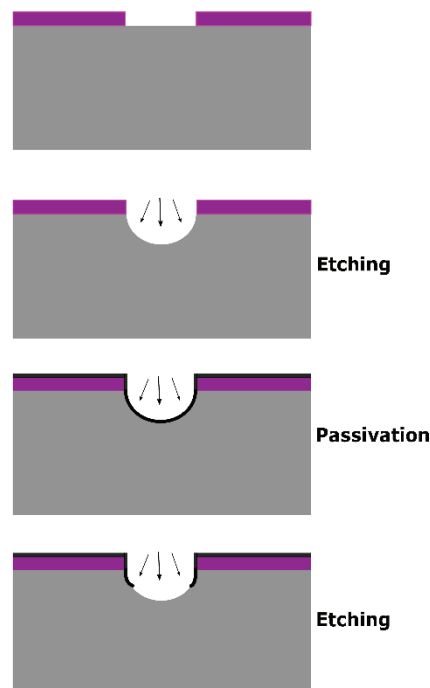
Figure 3.2 Schematic illustration of Bosch Process

RIE is a plasma process where radiofrequency discharge-excited ions are used to etch a thin film in a low-pressure chamber. RIE is anisotropic (it has lower etched rate laterally and vertical sidewalls) because the ion bombardment is directional. RIE of silicon does not depend on the crystal plane, and therefore any shape can be fabricated, which is not possible in anisotropic wet etching. DRIE is similar to RIE but has a high rate of etching for deeper structures. There are two main ways to perform DRIE: Cryogenic and Bosch. In the present work, the Bosch process has been used to etch 100 µm features in silicon with vertical sidewalls.

The principle of the Bosch process is based on alternating etch, and passivation steps, Figure 3.2, the gas used for etching is Sulfur hexafluoride (SF_6), which creates fluorine radicals in high-density plasma. After each etches step, a thin passivating film of fluorocarbon is

deposited from cyclic octofluorocyclobutane (c-C_4F_8). This film prevents further etching and therefore, is used at the start of every next step. This passivating film is removed from the horizontal surfaces but not from the sidewalls. Because of this the etching mainly occurs from the horizontal surface, and the sidewalls remain passivated (highly anisotropic). The repetition of etching and passivation steps results in vertical sidewalls with an aspect ratio of 20:1. The pulse timings of etching and passivation are typically 5-15 s. These pulsed etch, and passivation steps are the reason the etched structure of sidewalls shows scalloping (undulation). The anisotropy, etch rate, selectivity and scalloping all of these depend on the duration and overlap of etching and passivation pulses [18].

3.2   Fabrication of thin liquid cell

Compared to the liquid cells previously used in Miller's group [57], [74], the liquid cells used in this thesis are 8×3 mm in size and uses thinner (20 nm) low-stress LPCVD silicon nitride with four different lateral dimensions 30×100, 50×100, 30×200 and 50×200. The outer dimensions of the chips were changed to adapt to the new specimen holder developed in-house. At the same time, the thickness was reduced to decrease the background scatter, which should be minimum to extract the detailed information about the specimen, as described by the author in section 2.3.1. The lateral dimensions were then chosen to suit the thin windows and at the same time to maintain a balance between bulging and viewing area. However, the total bulging was still too much to get the desired resolution for in-liquid imaging and diffraction (~3 µm). Details about bulging calculation have been provided by the author in section 4.1. In Appendix 1, this issue of window deformation and poor spatial resolution is illustrated.

To attain excellent resolution for different types of specimens such as inorganic, organic and biological materials, additional techniques such as pressure regulation would be required [188]. The author has combined these 20 *nm* thin windowed flow cells into an environmental cell concept to develop a new setup called the environmental liquid cell. In chapter 5, the author has illustrated the improved resolution attained with it for different types of specimens.

Figure 3.3 explains the fabrication steps involved in making the liquid cells. Single crystalline silicon wafers (300 µm) with low-stress silicon nitride deposited on both sides by the LPCVD method is etched anisotropically in hot KOH. The pattern is transferred using UV-photolithography, and then reactive ion etching is used to remove silicon nitride. The remaining silicon nitride is used as a hard mask for KOH etching. Finally, 20 nm thick free-standing silicon nitride windows are obtained along with the flow openings. A silicon dioxide spacer 80 nm

thick is sputtered on the top part and patterned as a rectangular nano-channel (250 µm× 5400 µm) using UV-photolithography and buffered oxide etch (BOE). The nano-channels are overlapped with 150 µm deep reservoirs which are present to reduce the high flow resistance area and help flowing liquid in an 80 nm thick channel with significant internal pressure.

Flowing in the liquid is not easy, and therefore care must be taken to have the channels and windows thoroughly cleaned and the liquid cells should be surface treated to increase the hydrophilicity of the windows [164]. The liquid cell parts are cleaned with a mixture of concentrated sulfuric acid and hydrogen peroxide at 80 °C (piranha solution) for 30 min. This treatment not only removes the organic contaminants by oxidizing them but also makes the surface of the liquid cell hydrophilic which is very much required to increase the wettability [74]. The liquid cells produced at SiMPore Inc., USA were clean and free from organic contaminants. Therefore, instead of using piranha, simple plasma glow discharge was performed to increase the hydrophilicity of the silicon nitride windows.
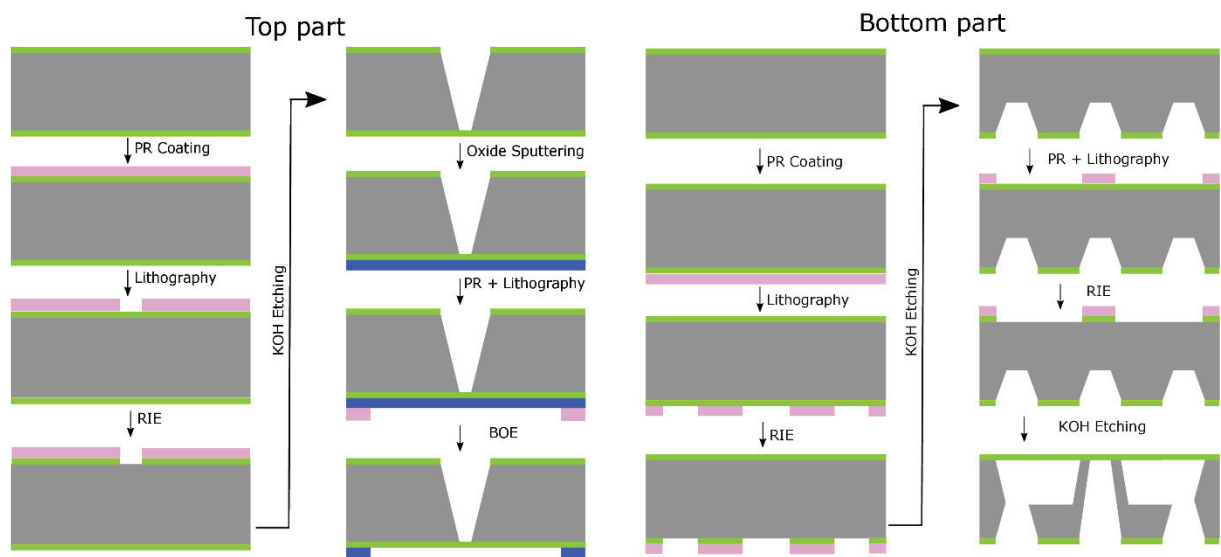
Figure 3.3: Microfabrication of top and bottom part of single windowed (standard) liquid cell

The liquid cells can be used in two different assemblies. The first is a static assembly, where small volume (0.5-1 µl) liquid sample is pre-loaded on the liquid cell chips. The second can be a flow assembly, which can either be used to flow sample or reagents for capturing the reaction dynamics *in situ* [56], [57], [64]. The flow assembly can also be utilized for single-shot diffraction experiments where the sample is damaged with an electron beam and needs to be refreshed frequently [189]. The author has performed all the in-liquid TEM measurements with the nanofluidic (flow) chips combined with the environmental cell concept, discussed in chapter 5.

4 Challenges using liquid cells: bulging measurements

The contribution of sample support, for instance, liquid-cell window, in a TEM measurement, should be such that the background scattering is minimum. The strong electron matter interaction in TEMs, discussed in section 2.2, poses stringent limits on the material composition and thickness of the window through which the electron beam must pass. Both of these can be tuned to obtain optimal performance [190]. In the present thesis, significant work has been done by the author to improve the performance of the liquid cell window.

Excellent mechanical properties offered by silicon nitride thin film make them good candidates for liquid cell windows. The ability of these films to withstand as large as atmospheric pressure differential while being suspended over a large area (hundreds of micrometers wide) free-standing thin films (< 100 nm) on silicon support, making them ideal candidates for the purpose. Their ability to act as a free-standing film is a consequence of being able to control the film stress through film stoichiometry during deposition [191], [192]. The excellent mechanical properties of these films have made them useful in areas such as nanofluidic cells for ultrafast studies on water and as a window material for performing LPTEM [57], [74], [193].

The free-standing thin films of silicon nitride used as liquid cell windows are non-stoichiometric (silicon-rich silicon nitride) deposited via the LPCVD technique, as described in section 3.1.1. The stoichiometry and in turn, the residual stress in these films can be controlled by tuning the ratio of the precursor gases [194]. The tensile residual stress of these thin films is responsible for giving them the excellent ability to hold to atmospheric pressure difference. When using non-stoichiometric LPCVD silicon nitride thin films as liquid cells, two free-standing films suspended on silicon support are hermetically sealed with a spacer of desired thickness [57]. These films tend to bulge outward under pressure differences. Outward bulging drastically increases the sample thickness during TEM measurements. Hence, it is essential to characterize the bulging in the liquid cell window and investigate ways to minimize it.

This chapter has three parts, the first part, focuses on previous work done in the group related to liquid cell fabrication and development and the challenges faced. Thereafter, the author explains the idea of bulging in liquid cells. In the last section, the author introduces the concept of a multiple-window liquid cell for phase-contrast imaging.

4.1 Liquid cell design and challenges

The first closed liquid cell with flow capabilities presented in the Miller group was from Maher Harb. The design included two 40 nm thick windows separated 100nm silicon dioxide spacer. The specimen used was diiodomethane (CH_2I_2), but the attempts to acquire diffraction signals from iodine were unsuccessful [195]. The reason for this was the outward bulging of silicon nitride windows under the 1 atmosphere pressure difference for such thin windows. This work was taken forward by Christina Mueller, who worked to adapt the silicon nitride windows (100×50 μm) for use in TEM. This design included an active feedback loop to avoid fluctuations in the liquid layer thickness during in-situ measurements [163]. Although the problem of bulging and continuous flow was still not solved, nanometer spatial resolution was obtained on gold and polymer using STEM [57]. This development was continued by Sercan Keskin. These liquid cells included 50 nm thin silicon nitride windows with lateral dimensions of 200 μm x 100 μm for e-diff experiments and various sizes ranging from 200 μm x 50 μm to 100 μm x 10 μm for TEM measurements [164]. The problem of the bulging and continuous flow continued. Still, it was possible to capture biomolecular and cellular dynamics without liquid loss and over viewing times of up to several hours with a static liquid cell [64], [196].

In this chapter, work has mostly been done to address the issue of bulging. The new elliptical multi-window liquid cells promise to solve the two main problems existing in the single large window liquid cell. Firstly, the bulging issue is resolved here by introducing small (5 -15 μm) elliptical windows. The total bulging in the centre of a 5 μm, 10 nm thin Silicon nitride windows is 120 nm. Further details are provided in part 4.3. With this, specimen thicknesses less than half the elastic mean free path length, required to achieve phase contrast imaging conditions can be attained. The mfp length for water, of 200 keV electrons with zero collection semi-angle is 445 nm, this vale is obtained using Equation 2.4, in chapter 2, further details about which has been given in section 5.3 [89].

Secondly, the issue of having a larger viewing area is resolved as this design utilizes multiple small windows. Conventional liquid cell design with single windows are restricted to have dimensions lower than 200×100 μm^2. Large single windows are not mechanically stable plus an additional upper limit is imposed on their width due to bulging. Subsequently, the available viewing area is restricted to a maximum value of 50-100 μm^2. The smaller area poses issues while performing in-liquid measurements with custom-built machines with large electron probe size. Also, it is not ideal for doing *in situ* measurements of biological systems such as mammalian cells. The windows in the new design, have four times higher viewing area than the single-window design. The author is of the view that to be able to understand how the new

elliptical multi-window idea is better compared to the conventional single-window design; it is very crucial to get hold of the main issues of the latter. Therefore, in the next section, the author provides a short theoretical background about bulging in silicon nitride thin film. Measurements done by the author to realize the deformation in the conventional single-window liquid cell, describer earlier in chapter 3, are also discussed.

4.2 Bulging in the liquid cell

Bulging is defined as the deformation of thin membrane inward or outward under a pressure difference. In LPTEM the standard liquid cells have windows made from free-standing films of LPCVD silicon nitride which bulges outwards increasing the separation between the top and bottom membranes which in turn increases the liquid thickness. As a consequence, the liquid thickness is greater than the designed spacer thickness, which results in an inhomogeneous layer of liquid that is thicker in the centre than towards the edges. Therefore, imaging needs to be done around the edges of the window to obtain high-resolution images [111]. Another possible method to mitigate the bulging is to intentionally introduce a thick spacer (10 µm) with the standard liquid flow cell, in combination with an environmental cell concept. This idea, called the environmental liquid cell, is explained in detail in chapter 5 of this thesis.

4.2.1 Model for bulging

Mechanical properties of thin films and the residual stress in them have proven as beneficial concepts for the fabrication of electronic devices, microsensor and liquid cells [197], [198]. The techniques used to characterize the mechanical properties for bulk material did not work for thin films. To assess the mechanical properties of thin films, Beams established the bulge test technique back in 1959 [199]. Thereafter, Vlassak *et al.* and Small *et al.* performed bulging measurements to characterize thin films of silicon nitride [84], [200]. Deformation in the centre of a rectangular or square thin film under a uniform pressure as explained by the schematic in Figure 4.1 is given by,

$$P = \frac{c\,t\,\sigma_0\,h}{a^2} + \frac{8\,Y\,t}{6a^4(1-v^2)}h^3 \qquad\qquad 4.1$$

where P is the pressure, σ_0 is the residual stress in the thin film. The thickness of the film is t while a is its width. The Young's modulus, Poisson's ratio and coefficient of residual stress are, Y, v, and c, respectively, and h is the maximum deformation at the centre of the thin film. The

author has used Equation 4.1, to compute the bulging (h) in LPCVD deposited low-stress silicon nitride thin film (20 *nm*). These membranes have been used by the author for performing all the LPTEM work reported in this thesis. The parameters used are, $Y = 235$ GPa [164], $v = 0.28$, $\sigma_0 = 147$ MPa, $P = 100000$ Pa, and $c = 2$ [84]. The residual stress coefficient (c) is a function of the membrane aspect ratio [84].
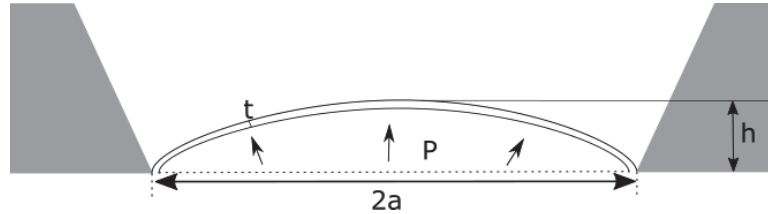
Figure 4.1: Schematic showing bulging (h) in a thin film of a thickness (t) and short edge width (2a) under constant pressure (P).

 Bulging was calculated for two different cases, see Figure 4.2. The A part of the figure shows total bulging (2h) versus the width of the window (2a) for thicknesses 10 and 20 nm, while part B displays total bulging (2h) versus the thickness of window (t) for widths 30 and 50 µm.
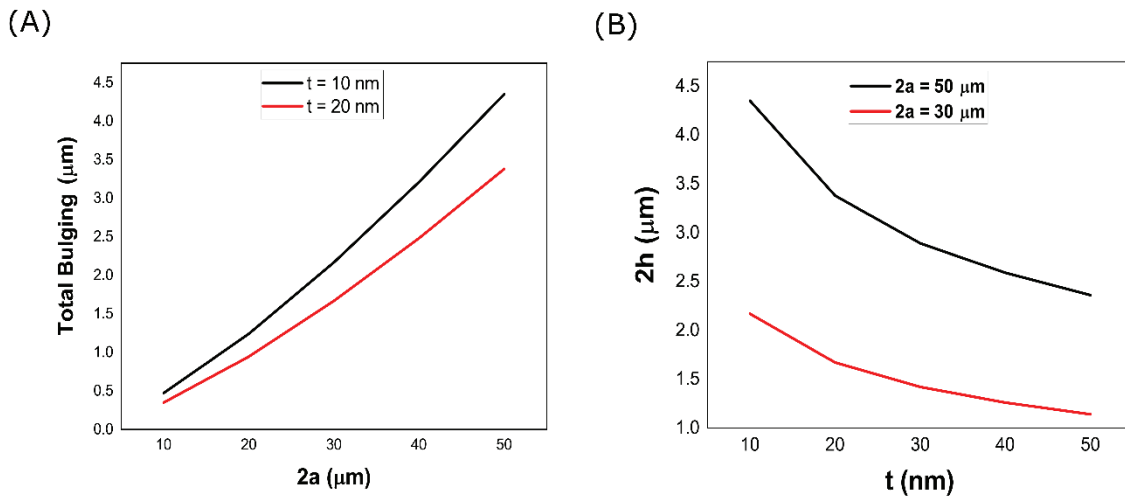
Figure 4.2: Plots calculated using eq. (5.1) showing the variation in total bulging (2h) concerning (A) width of short edge (2a) of the window, (B) thickness (t) of the window.

4.2.2   Measuring the bulging in silicon nitride

When the light of a particular wavelength is shone on two thin films separated by a distance, constructive and destructive interference of the light waves occurs depending on the distance between the thin films. Bright or dark fringes similar to Newton rings can be observed and can be used to calculate the distance between the centres of thin films. The thickness profile

achieved using this method is not absolute; instead, it gives a relative thickness above the offset. The author has utilized this technique to measure the relative distance between the top and bottom chips of a hermetically sealed liquid cell under a pressure difference of 100000 Pa. The measurement was done to confirm the bulging computed using Equation 4.1.

A thin film interferometer with a green bandpass filter ($\lambda = 550$ nm, FWHM = 10 ± 2 nm) was used to observe the interference of light waves transmitted through the silicon nitride windows in a vacuum. This setup was designed by Dr. Sercan Keskin (Miller group) and has been extensively described in his thesis [164]. The top and bottom 20 *nm* silicon nitride/silicon liquid cell chips were put together in the liquid cell specimen holder and sealed using Viton O-rings. The O-rings pressing against the silicon wafer in the mount of the holder can induce mechanical stress on the windows. If an inhomogeneous force is applied on the liquid cell, windows can deform, resulting in interference. These fringes can be captured using a camera attached to the objective piece. When the experiment chamber where the liquid cell holder is placed, is evacuated, the number of fringes already present on the windows, increases.

Figure 4.3 shows the phenomenon of interference, on illumination by a white light source, some fraction of the incident light (ray 1) transmits unaltered through the window. In contrast, some fraction (ray 2) gets transmitted after being reflected from top and bottom windows. If ray 1 travels a distance d, then the distance travelled by ray 2 is 3d when this difference of 2d corresponds to a multiple of the wavelength of the light source ($\lambda = 550$ nm), the rays then interfere constructively and give rise to bright fringes in the centre of the window. This relation can be mathematically expressed as,

$$2dn = m\lambda \qquad\qquad\qquad 4.2$$
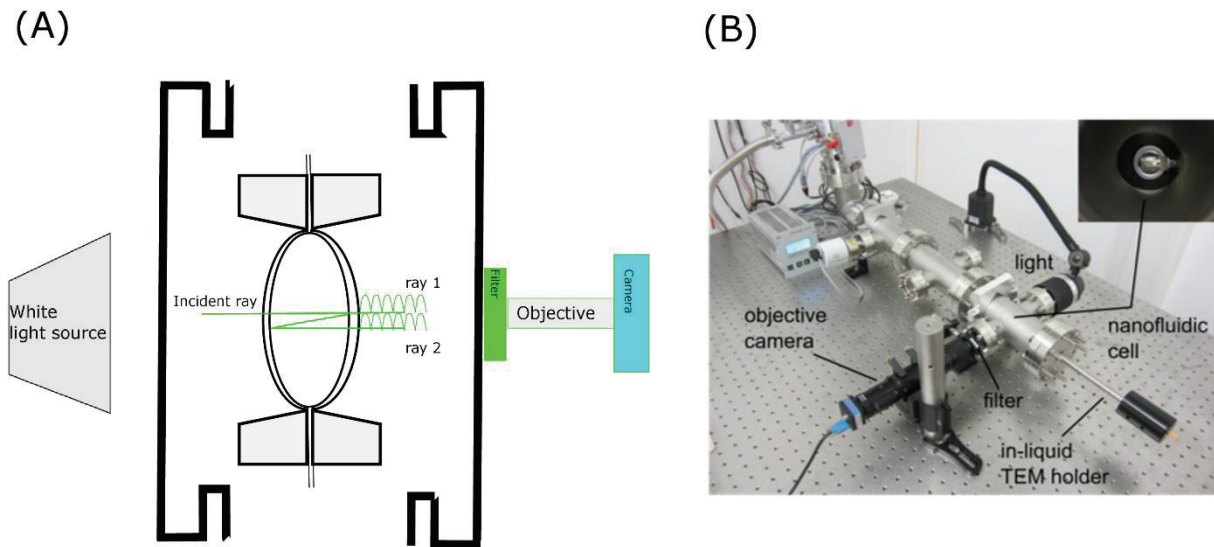
Figure 4.3: (A) Schematic illustrating the white light interferometer. A white light source is incident on the liquid cell window under vacuum (deformed) the transmitted light after travelling the distance undergoes interference which is captured by using an objective and a camera, the (B) setup used for calculating the bulging [164].

where d is defined as the bulging, n is the refractive index of water, m is the number of fringes formed, and λ is the wavelength of the light used. The bulging can be calculated knowing the number of fringes formed (m) when the window is under a pressure difference.

Figure 4.4 shows two silicon nitride windows with lateral dimensions as 50 × 200 μm and a thickness of 20 *nm*. 1 μl of deionized water was drop cast on the bottom chip, covered with a top chip and hermetically sealed with O-rings in the liquid cell specimen holder [201]. In the A part of the figure, no bulging occurs as pressure difference is zero, while in part B, bulging is observed as the pressure difference is 1 bar (10^5 Pa). The number of fringes in the case of a maximal bulged liquid cell is 16, giving a total bulging (2d) of 3.3 μm. The computed value of the total deformation, using Equation 4.1, for a similar window dimension is 3.4 μm. The two methods appear to be in good agreement with each other. Therefore, either the calculation or the experimental method can be used to assess the deformation of the liquid cell window.

A total bulging of 3 μm, implies a specimen thickness seven times of the elastic mean free path length for water, in a 200 keV TEM. In-liquid imaging, with these liquid cells, is only possible at the edges. The author has looked into this problem via two different approaches, mitigating the bulging effects by a reduction in the width of the windows, and using an environmental cell

approach which bulging becomes insignificant. The former is discussed in the next section (4.3) while the latter has been described in chapter 5.
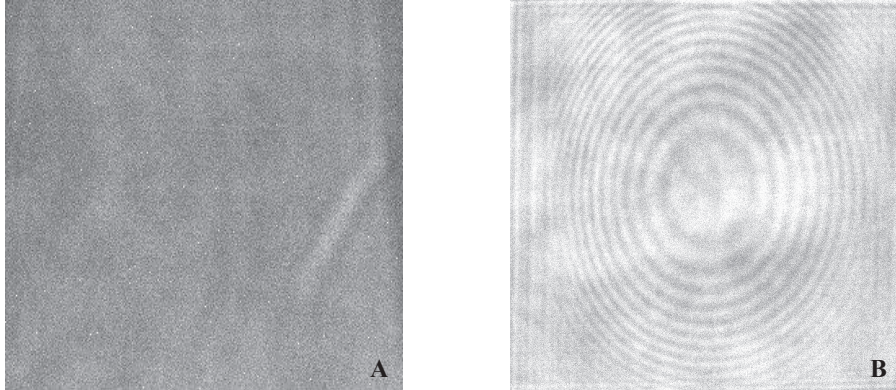
Figure 4.4: Interference images from two 20 nm silicon nitride windows assembled (A) at 1 bar pressure (no vacuum), (B) at 4 mbar (vacuum). No interference patterns are observed when the chamber is maintained at atmospheric pressure (1 bar). Patterns start to appear as the chamber is evacuated, and at $P = 4$ mbar a maximum of 16 fringes are seen [201]. No further increase in the number is observed after this point.

4.3   Multi-window liquid cell for phase-contrast imaging

As described in 4.2, for some specific in-liquid imaging/diffraction application, large windows are essential. But, the single-window liquid cell cannot promise large viewing area due to bulging and mechanical instability. Honeycomb patterns, on the other hand, are known for their mechanical strength [202]. Therefore, multiple small windows separated by bars (5-10 μm thick) were designed with a honeycomb pattern to reduce the total bulging and increase the viewing area without compromising on the mechanical stability of the windows [164]. The details of the fabrication can be found in the thesis of Dr. Sercan Keskin (Miller group), who was involved in the design process. The manufacturing was done in collaboration with Prof. Hoc Khiem Trieu and Deybith Venegas-Rojas (TUHH) [164], [198]. The fabrication of honeycomb liquid cells was based on the deep reactive ion etching of 100 μm thick single crystalline silicon wafer. The honeycomb pattern was transferred onto the wafer, which acts as a support structure for the 50 nm thin silicon nitride windows. The first batch of the honeycomb liquid cells fabricated was tested in the TEM by the author, see Figure 4.5. Part A shows a low magnification view of one large window area with several small multiple windows. Small

windows appear to be circular rather than hexagonal, a possible explanation for this could be the difference in the etch rates at the centre and the corners.

Moreover, due to the high aspect ratio of the feature wall, the sidewall passivation, discussed in section 3.1, reduces with the depth, thereby increasing the lateral etching. This occurs due to the ionic bombardment of the insulating silicon dioxide, resulting in charge accumulation near the wall, leading to further widening of the features. The phenomenon observed is the notching effect and is a standard problem encountered in silicon microfabrication [185]. The issue of not obtaining sharp hexagonal corners can be overlooked as circular shape structures can still be considered mechanically robust [198]. However, the problem of poor yield is significant; see Figure 4.5 (B), the silicon nitride layer been etched away in some regions. A better understanding of the residual stress in the silicon nitride-silicon dioxide stack layer is required to obtain defect-free liquid cells. Figure 4.5 displays TEM micrographs of gold nanorods sandwiched between two honeycomb liquid cell chips. The micrograph in part C shows one of the intact silicon nitride membranes with gold nanorods 25 x 85 nm.

(A) (B) (C)
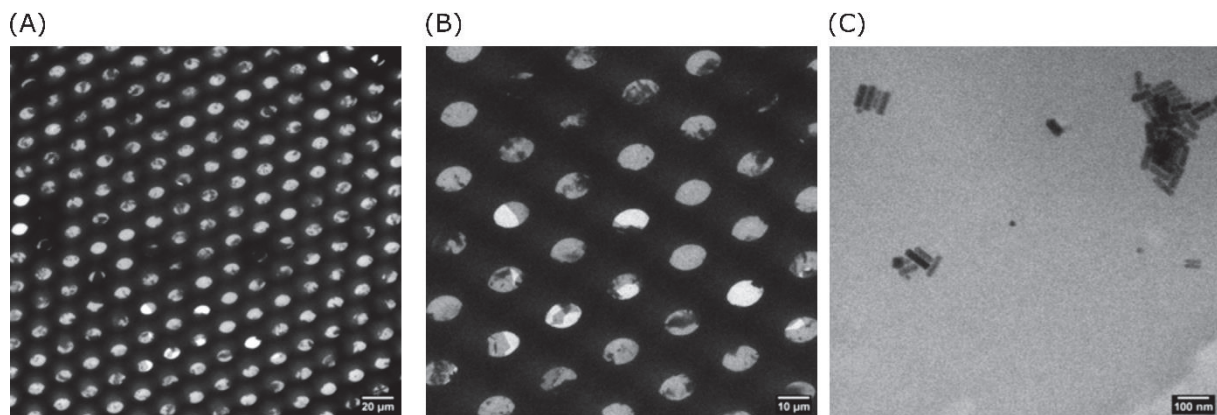
Figure 4.5: (A) low magnification view of a large (500 x 500 µm) window with multiple small windows, (B) higher magnification view of the left micrograph showing etched away nitride in some small windows, (C) gold Nanorods imaged in captured in one of the small intact windows.

The author has contributed towards a similar multiple small window liquid cell design which is being manufactured in collaboration with an external company. The fabrication design feasibility and stress and bulging characterization were done by the author, Mr. Josef Gonschior (Engineer, Miller group), Drs. Günther Kassier, Dr. Eike Christain Schulz, Ms. Lindsey Bultema and Dr. Robert Bücker. Thereafter, the author describes the design feasibility in terms

of fabrications steps involved, stress and bulging computation using Finite element method (FEM). The FEM simulations were performed by Mr. Josef Gonschior with inputs from the author.

The design idea for multiple small windows, called elliptical multi-window liquid cell, considers all the previous issues addressed by the honeycomb liquid cell such as bulging, mechanical stability and viewing area. Besides, it also aims to solve the background scattering problem by reducing the thickness of the silicon nitride film from 50 to 10 nm. According to the design, each liquid cell would comprise of a large rectangular window, with multiple small elliptical windows patterned on silicon which supports the very thin (10 nm) free-standing silicon nitride. The shape of small windows is chosen to be elliptical because such features are stable in terms of mechanical stability, can be easily fabricated, and additionally, they allow ease of alignment of top and bottom parts. The dimensions of the small elliptical windows and silicon support structures are chosen to minimize the bulging.

The deformation was calculated for the 10 nm silicon nitride on 30 μm thick silicon with lateral dimensions of 600 × 400 μm², having multiple miniature elliptical windows with sizes 30 μm × 5 μm, 30 μm × 10 μm, and 30 μm × 15 μm, where 30 μm was the diameter of the major axis and was kept constant. The maximum bulging for two such windows, Figure 4.6 (A), was found to be 44 nm. The maximum stress at the edge was 14 Mpa, see Figure 4.6 (B).

(A)
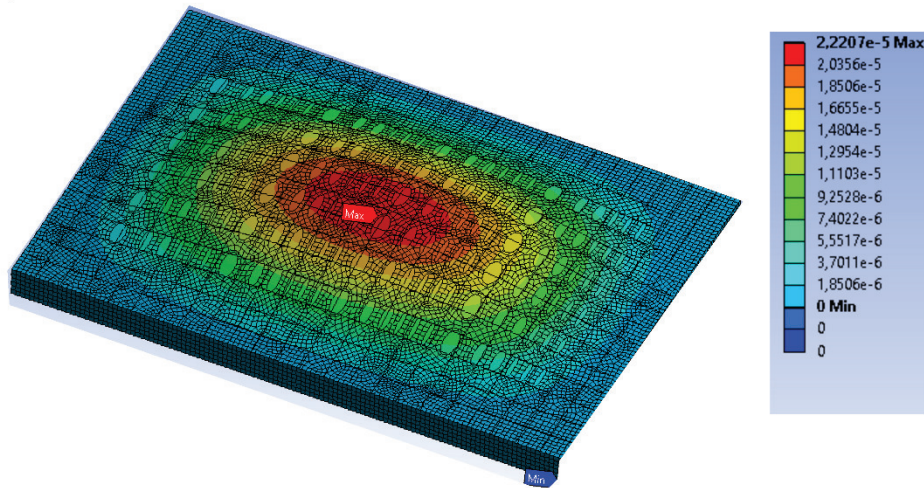
(B)
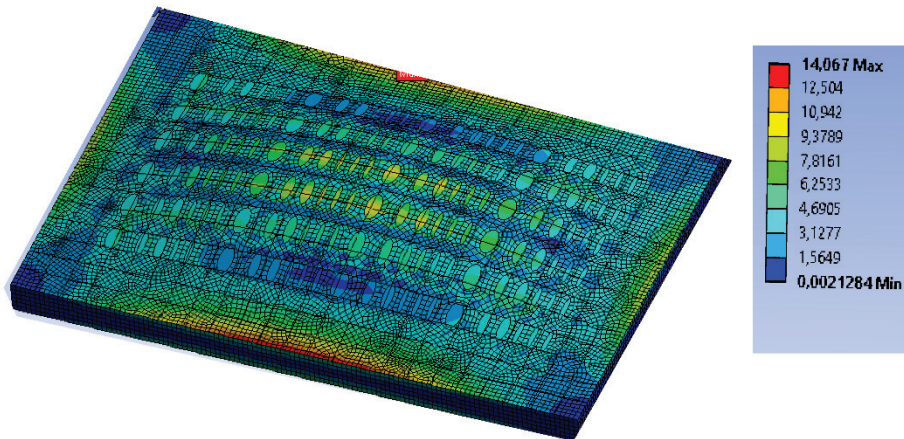
Figure 4.6 (A) is the deformation and (B) shows the stress on a single large window (600 × 400 µm2) with multiple elliptical windows and a 10 nm free-standing silicon nitride. The maximum bulging is seen at the centre of the window (red portion) which reduces as we move towards the edges. The maximum value of stress is seen in a small region near the centre edge.

The fabrication of the design is ongoing. Therefore, the details cannot be provided at this time. Figure 4.7 presents the design idea of multiple-window liquid cell showing top-bottom overlap in small elliptical windows.
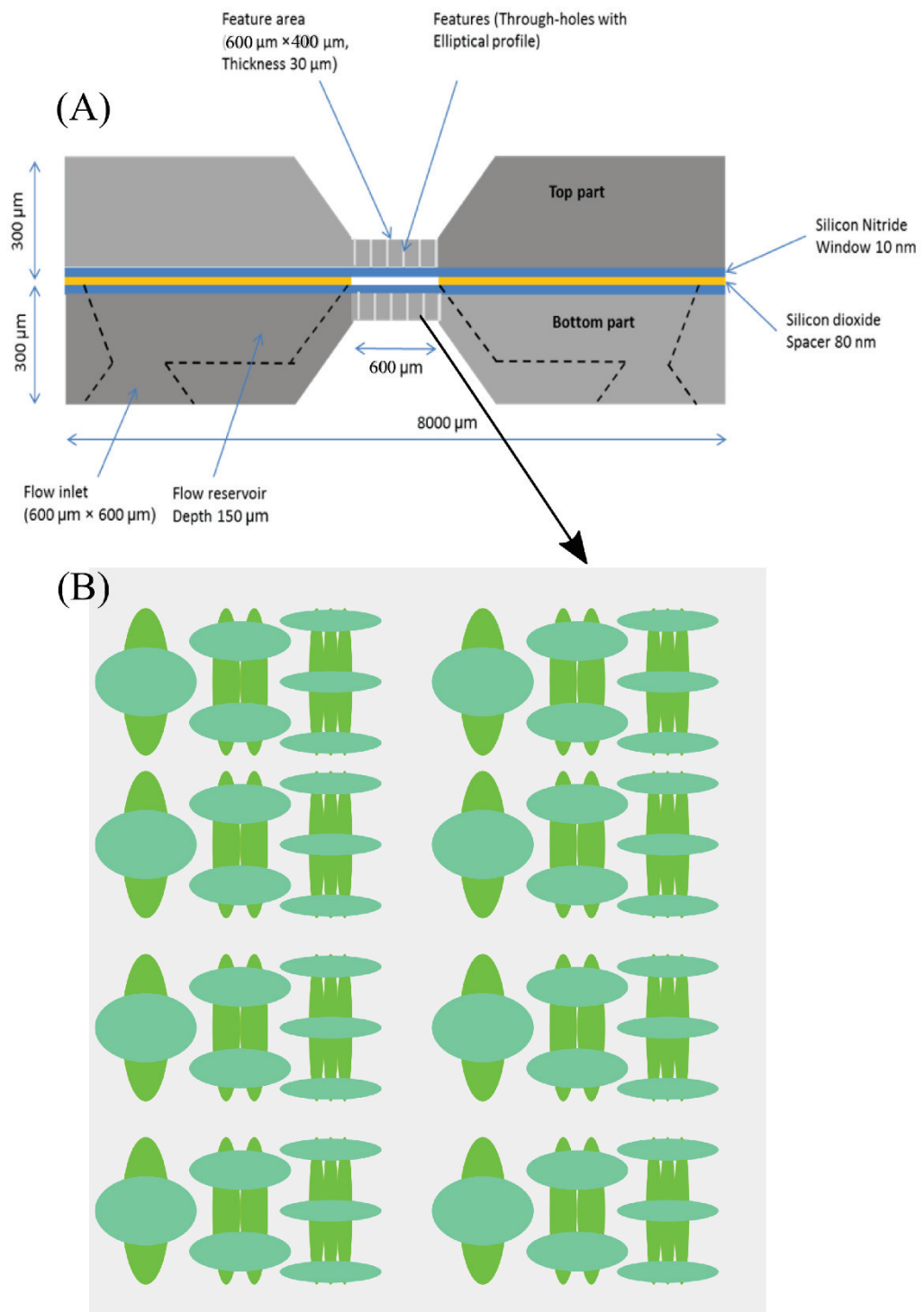
Figure 4.7 (A) schematic of multi-window liquid cell (B) set of small elliptical windows showing top-bottom overlap.

5 Development of environmental liquid cell for improved in-liquid imaging and diffraction

In this chapter, the author illustrates a technique developed to achieve the primary goal of her PhD work, i.e., performing in-liquid electron imaging and diffraction. The method is called the environmental liquid cell (ELC) TEM and was developed by the author with the help of a post-doctoral researcher Dr. Günther Kassier and members of Scientific Support Unit for Machine Physics (Friedjof Tellkamp and Jan-Philipp Leimkohl) of the Max Planck Institute for the Structure and Dynamics of Matter. Real-space imaging was possible for different types of specimens with improved resolution. Proof of principle measurements were done on gold nanoparticles, polystyrene, and ferritin molecules. The obtained results have been compared to previously reported work to demonstrate the success of this technique. Static diffraction on liquid water was also performed and has been presented by the author in chapter 6. A significant portion of this chapter is based on a submitted manuscript in which the author shares the first co-authorship with Lindsey Bultema. However, the work reported here does not include the part contributed by Lindsey Bultema.

The work has been portioned in six different parts. In the beginning, the idea of environmental liquid cell design and technical details are discussed. The sample preparation required with this method is slightly different from the conventional liquid phase TEM (LPTEM) and is discussed in the next part. Another very crucial concept is the estimation of liquid thickness, and data analysis performed to extract the useful information from obtained micrographs. This has been described in the third section. The analysis was performed with Dr. Michiel de Kock, who was a post-doctoral researcher in the theory division of the Miller group. LPTEM performed on different specimens are discussed in the next two parts. In the last section, the success of ELC TEM in terms of attainable resolution and dose sensitivity over the conventional LPTEM is highlighted.

Environmental TEM (ETEM) is one of the many ways to perform LPTEM. It allows the observation of catalytic reactions under low vacuum conditions [203], [204]. LPTEM keeps the specimen immersed in a liquid layer of a thickness equal to, or larger than, the specimen

dimensions, while ETEM merely engulfs it in a highly humid environment [54], [205]. Inayoshi *et al.* developed a modified environmental cell capable of maintaining a liquid layer of roughly 100 nm thickness in an assembly which consisted of two standard carbon TEM grids separated by a spacer of desired thickness (100-500 μm). The pressure between the grids was controlled by adjusting the flow rate of humid air, thereby adjusting the liquid layer thickness [162]. However, this design lacks the ability of *in-situ* flow, thus preventing the exchange and replenishment of the sample/liquid.

The ELC technique developed by the author, combines the approach of Ianoshi *et al.* with our liquid flow cell technology, thus merging the high resolution and contrast potential of ETEM with the ease of use and high reproducibility of silicon nitride-technology [57]. A key advantage of this approach is its simplicity since merely a 10 μm polyimide spacer (Kapton) is added between the silicon nitride nanofluidic cells. Additionally, our ELC TEM method enables the exchange of buffers or reagents during measurements through a syringe pump injection at the inlet port of the ELC (*in-situ loading)*. This feature has been demonstrated by establishingproper control of the liquid layer thickness in the ELC with gold particles (AuNPs). The resultant favourable imaging conditions were utilized to demonstrate imaging of weak mass thickness contrast specimens i.e., polystyrene (PS) particles and ferritin molecules at a maximum electron dose rate of 2 e/Å^2/s.

5.1 The environment liquid cell

ELC setup consists of the nanofluidic cell, the sample holder and the humidity control apparatus (Figure 5.1). The nanofluidic chips were produced by SiMPore Inc., USA using the design described in section 3.2. A fully assembled nanofluidic cell consists of two silicon chips with a silicon nitride window, one with flow openings (bottom) and one without (top). Similar to Muller *et al.*, a trench is running between the flow openings, to reduce flow resistance and improve window longevity [57]. The assembly of these custom nanofluidic cells into an ELC was done by first glow discharging the bottom chips for 30 seconds; details about this has been provided by the author in section 5.2. Next step was the placement of a 10 μm thick Kapton spacer between the silicon chips to allow airflow through the sample window area. The Kapton spacer was an essential modification over traditional liquid cell assembly. After placing the Kapton-spacer on the bottom-chip, 0.5 μl of sample is applied directly onto the silicon nitride window area with a pipette. Finally, the ELC is closed with a top-chip, and assembled in our custom-built ELC holder, consisting of a head land arm piece.

The ELC holder has an aluminium headpiece equipped with a lid for mounting the nanofluidic chip (3 x 8 mm), a port for the electron beam as well as inlet and outlet flow ports with internally machined flow channels. Fluoroelastomer (FPM) O-rings are placed on the three ports, and surrounding periphery of the cavity wherein the chip assembly is mounted (8.5 x 0.8 mm). The aluminum lid has three grooves for FPM O-rings (0.97 x 0.33 mm) and four screw holes. The ELC assembled bottom is covered with the lid and secured in place with four titanium screws (corners). Upon assembly, all O-rings are aligned, and connections are sealed for vacuum compatibility. A Polyether ether ketone (PEEK) piece joins the head to the arm of the ELC holder. The flow channels are connected to the outside via PEEK tubing (1/16 in. x 0.020 in.). Additionally, the head is equipped with a resistive heating element and two PEEK tubes connected to a water chiller enabling temperature control from 4-100 °C, an essential requirement for many biological specimens.
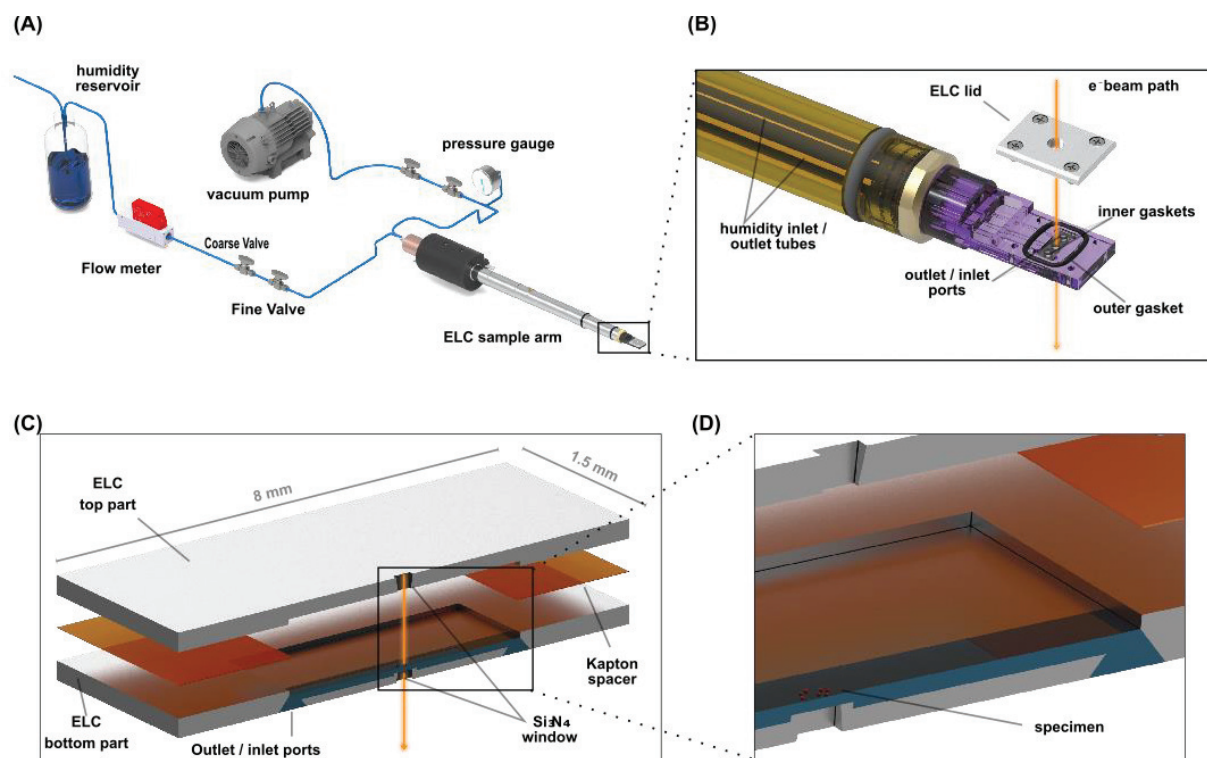
Figure 5.1: Environmental Liquid cell setup, (A), Schematic of the ELC setup which consists of a liquid cell specimen holder with an ELC inside. The inlet port of the holder is connected to a flowmeter and a humidity reservoir while the outlet is connected to a vacuum pump. Two fine-tuning valves are attached on both sides to control the flow precisely, (B) An expanded view of the specimen holder (C) An expanded view of the ELC and (D) Magnified view of the window area in the ELC.

Connecting the humid flow control apparatus to the ELC produces a moist air stream that engulfs the specimen, resulting in a liquid layer of a controllable thickness (Figure 5.1). PEEK tubing connects the inlet port to a humidity reservoir and the outlet to a vacuum pump. The pressure and humidity flow are observed with the connected vacuum gauge and a flow meter. By adjusting the flow speed and pressure with the two fine-tuning valves, the liquid layer thickness on the bottom silicon nitride-window is controlled via a combination of liquid displacement and condensation/evaporation effects. Specimen solutions and reagents can be loaded either by pre-assembly directly on the silicon nitride-window, or post-assembly via flow, thus opening the possibility of triggering *in-situ* reactions.

5.2   ELC sample preparation

Gold nanoparticles were purchased from Sigma Aldrich GmbH and were diluted 20 times in DI water before use. An aqueous suspension of polystyrene nanoparticles of size 0.1 μm was purchased from Sigma Aldrich. Horse spleen ferritin was procured form Serva Feinbiochemica, Heidelberg. Polyimide (Kapton) spacers were laser cut from 10 μm Kapton sheet into 3x 8 mm rectangles, with a 5.4x 0.5 mm cut-out in the centre. The outer dimension and inner cutout match the nanofluidic chip specifications. Laser cutting was conducted with a Protolaser U3 (LPKF, Hannover); the maximum power of the laser is 6 watts at a wavelength of 355 nm.

Before assembly, the nanofluidic (bottom) chips were selectively glow discharged in a custom-designed 3D-printed holder. The holder consisted of two parts, a base, and a lid. The chips were arranged 2x2 on the base and covered with the lid which selectively exposes the window and channel areas. Subsequently, the chips were glow-discharged for 30 s at 35 mA in a glow discharger (Balzers CTA 010, Balzers Union, Switzerland). This resulted in selective wetting of the window and channel areas. TEM imaging was performed in the bright-field mode in a JEOL JEM-2100 operated at 200 keV and fitted with a TVIPS TemCam F216 camera without an energy filter. All experiments were performed at room temperature (approximately 23°C). The dose calibration was done using the absolute count values of the camera image, which were calibrated from the phosphor screen current readout.

5.3   Liquid layer thickness determination

It is crucial to know the thickness of the liquid layer in any LPTEM measurement so that one can tune it as per the requirement. The liquid layer thickness determination in the ELC was done by measuring the bright field scattering contrast, which is the fraction of electrons

that are not scattered outside the objective aperture collection angle. In the single-scattering approximation, the ratio of detected electron intensity with sample layer in the beam path (I) to that without the layer (I_0) is given by:

$$\frac{I}{I_0} = exp\{-t/L(\theta)\} \tag{5.1}$$

where t is the thickness of the material. The effective mean free path $L\ (\theta)$ for scattering to an angle of θ or higher is given by:

$$L(\theta) = \frac{W}{\sigma(\theta)\rho N_A} \tag{5.2}$$

with Avogadro's number N_A, the mass density ρ, the atomic weight W, and the scattering cross-section $\sigma\ (\theta)$. Note that the scattering cross-section and the mean free path are dependent on the collection semi-angle θ. The mean free paths were calculated by numerical integration of the scattering cross-section for silicon nitride and water [97], [206]:

$$\sigma_{SiN,el} = (1 + E/E_o)^2(3/7\ f_N^2 + 4/7\ f_{Si}^2) \tag{5.3}$$

$$\sigma_{SiN,inel} = \frac{4(1 + E/E_o)^2}{a_H^2(Q^2 + Q_0^2)^2}(3/7\ S_N + 4/7\ S_{Si}) \tag{5.4}$$

where $a_H = 0.529 \times 10^{-10}$ m (Bohr radius), $\lambda = 2.51 \times 10^{-12}$ m (electron wavelength at 200 keV), $E_0 = 511$ keV (electron rest mass-energy), $E = 200$ keV (accelerating voltage of the TEM used). Elastic and inelastic scattering factors for nitrogen and silicon are denoted by f_N , S_N , f_{Si}, and S_{si}, respectively, and were taken from the literature [122], [206]. The momentum transfer $Q = 2\pi\theta/\lambda$ is determined by the characteristic value

$$Q_E = \frac{2\ \pi}{\lambda}\frac{13.5\ Z}{2\ E}\frac{E\ +\ E_0}{E\ +\ 2\ E_0} \tag{5.5}$$

where $Z = 10.6$ (effective atomic number for silicon nitride). Note that the scattering cross-sections and the mean free path are dependent on the collection semi angle θ and the electron energy. The collection semi angle of the objective aperture used in the present study is given

50

by θ = 12.6 mrad as determined by directly imaging the objective aperture in diffraction mode. The detector camera length was calibrated using diffraction rings from a polycrystalline aluminum film. The scattering cross-section in case of water was directly taken from Wang *et al.*, the elastic and inelastic cross-sections computed for silicon nitride and water are tabulated in **Table 2** [206]**.**

Collection semi-angle (mrad)	$\sigma_{SiN, el}$, $\sigma_{SiN, inel}$ (nm^2) $\times$ 10^{-5}	$\sigma_{water, el}$, $\sigma_{water, inel}$ (nm^2) $\times$ 10^{-5}	Total mfp Si$_3$ N$_4$ (nm)	Total mfpWater (nm)
0	10.9, 15.1	6.7, 13.0	40	152
12.6	4.71, 0.79	3.3, 0.91	190	718

Table 2. Scattering cross-section and mean free path of silicon nitride and water. It shows total (θ = 0) and effective (θ = 12.6 mrad) elastic and inelastic scattering cross-sections and mean free paths for silicon nitride and water.

For the ELC system, by comparison with parallax measurements, we found fair agreement with the values obtained by this method, where the thickness was underestimated by 21% if calculated form the intensity ratio [111], [114], [207]. Still, the intensity ratio method provides a feasible means for thickness estimation without requiring any special equipment.

The data analysis was performed to extract useful information from a micrograph which is a noisy image of multiple particles of roughly similar shape and no preferred orientation. To observe the average structure of the particles, the power spectrum of the micrographs was computed, i.e. the 2D Fourier transform of the images was multiplied with its conjugate. Its useful properties, such as insensitivity to particle locations and the noise contribution generally conforming to a uniform or power law, makes the power spectrum a beneficial data reduction and filtering tool. The spherical symmetry of the particles is preserved in the power spectrum, allowing further data reduction by computing the radial average of the 2D power spectrum. Assuming there are no correlations between signal and noise, these components become additive, and an empty micrograph can be utilized to estimate a spectral signal to noise ratio as a function of spatial frequency ω,

$$Signal\ Ratio[\omega] = \frac{|C[\omega]|^2 - |N[\omega]|^2}{|N[\omega]|^2} \qquad 5.6$$

Sana Azim

with the radial average of the Fourier transform of the micrograph with particles, $C[\omega]$, and the micrograph without particles, $N[\omega]$. As this quantity is computed on the whole image and not for individual particles of known or inferred shape, it does not represent a true signal-to-noise ratio. The true signal-to-noise ratio is dependent on the degradation of the signal due to the water layer, which we do not examine here. However, we can use it as a comparative measure of image quality, defining the total signal as the sum of the signal ratio.

ImageJ and Origin (Origin Lab Corp.) software was used to determine the particle size of the PS particles. Particle picking was done in ImageJ, and exported to Origin, where box plots were generated to determine the size of the particles.

5.4 Liquid layer thickness and spatial resolution

With standard LPTEM techniques, the bulging of the silicon nitride window, which has been described by the author in section 4.2, limits the viewing area to regions close to the edges. Pressure control setups can regulate the bulging, ensuring a path length optimal for imaging. However, the imaging area is still restricted to the boundaries [188]. In the ELC, bulging is irrelevant due to the 10 μm Kapton spacer dominating the expected deformation of a 200x30x0.02 μm^3 silicon nitride window [74]. Additionally, the pressure control system regulating the condensation of the humid air on the sample-containing bottom window allows for the imaging of the whole window. Adjusting the Z position of the specimen holder and focusing on the thin liquid layer at the bottom ensures the highest resolution with TEM [156].

To benchmark, the spatial resolution in ELC with respect to the water layer thickness, 10 nm Gold nanoparticles (AuNPs) was imaged. Since imaging of organic and biological specimens labelled with AuNPs cannot tolerate as high doses as AuNPs, which can easily take 1000 $e^-/Å^2$, a total dose of 5 ± 0.4 $e^-/Å^2$ was used to better approximate conditions for imaging the soft matter systems of interest. The dose and exposure time of 2 s, was employed to specifically illustrate the suitability for these imaging applications [208], [209] under typical conditions. The error in the electron dose value was calculated from the standard deviation of measured electron doses over a time of 40 minutes. The liquid layer thickness was calculated using equation (5.1), with the mean free path of water for scattering to an angle $\theta = 12.6$ mrad or greater taken as 718 nm according to **Table 2**. The liquid layer was thinned by setting the flow rate to 1 ml/min and the pressure to 400 mbar. To give a particular example, the intensity

ratios before thinning down were 0.62, indicating a thickness of 340 ± 71 nm. Following this, an intensity ratio of 0.79 was achieved, corresponding to a thickness of 160 ± 34 nm.

It is possible to get a resolution parameter by measuring the intensity distribution across the edge of the particle (AuNP). The width $x_{0.5}$ between the points at which the step reaches 0.25 and 0.75 of its total intensity and therefore, the edge width of the AuNPs was used to characterize the dependence of image resolution on the liquid layer thickness [57], [97], [188]. Assuming the AuNPs exhibit a perfectly sharp boundary and the images are taken in-focus, the average edge width of six selected AuNPs was calculated from an error function fit of the respective line profiles generated by averaging the signal over a width of 3 pixels. The assumed error function has the form erf $\left(\frac{x-\mu}{\sigma\sqrt{2}}\right)$, where μ is the position of the edge, and σ is the width in the measurement. The standard deviation in the mean value is shown as the error in the resolution estimation. A representative micrograph and line profile of an AuNP is shown in Figure 5.2. As the liquid layer was thinned from 340 ± 71 nm to 160 ± 34 nm, the edge width resolution at a dose of 5 ± 0.4 e$^-$/Å^2 improved from 1.7 ± 0.8 nm to 0.8 ± 0.06 nm.
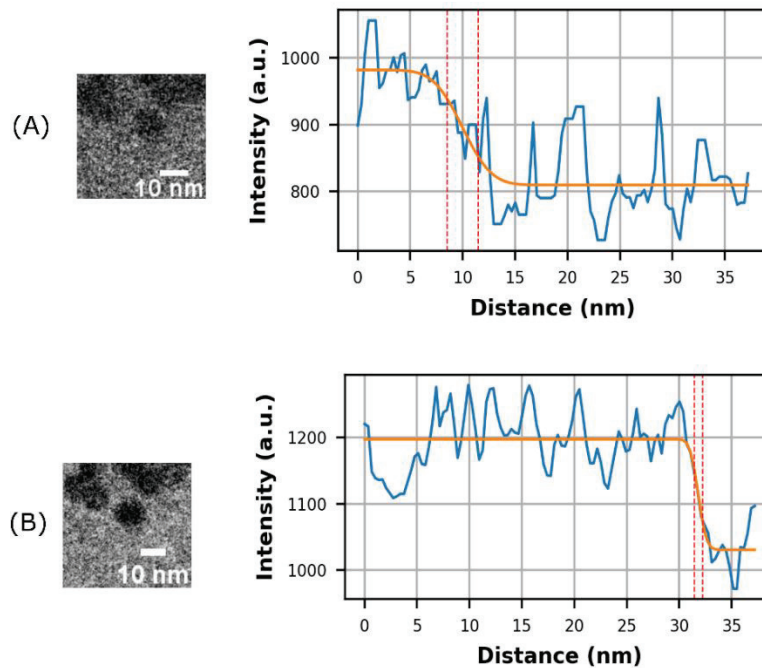
Figure 5.2: Water layer thickness optimization at two thicknesses. The water layer was thinned from 340 ± 71 nm (A) to 160 ± 34 nm (B) via the control of the vacuum and humid air source. The micrographs show a representative AuNP and a line profile (blue line) across the AuNP shown in the micrograph with an error function fit (orange line). Up to 6 AuNPs are averaged, and the error in the resolution is determined from the standard deviation of the mean value of

25-75% edge width resolution of these 6 AuNPs. The thinning of the liquid layer (A to B) improves the resolution from 1.7 ± 0.8 nm to 0.8 ± 006 nm.

Thereafter, the ELC capabilities were benchmarked with low mass-thickness contrast specimens. To this end, commercial polystyrene (PS) spheres (100 nm diameter) were imaged in liquid layer thicknesses of 0 and 40 ± 8 nm, the electron dose used was 0.4 e$^-$/Å^2 with an exposure time of 0.5 s, and the images were collected at -5 μm defocus (Figure 5.3). For liquid thickness greater than 100 nm, the PS particles were not clearly visible.
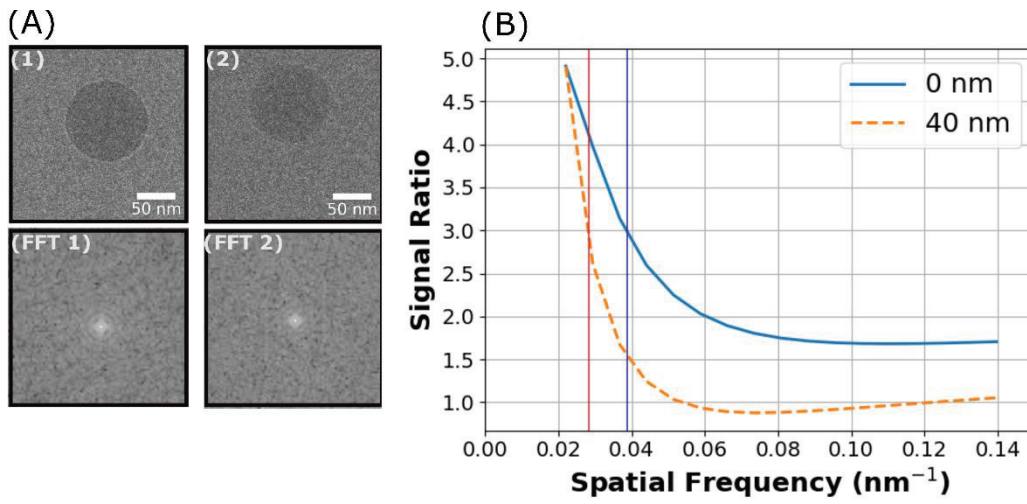
Figure 5.3: Liquid thickness optimization of Polystyrene (PS) particles in the ELC (A) TEM micrographs (1and 2) and their respective FFTs (FFT (1) and FFT (2)) for polystyrene beads in water layers of 0 (panel 1) and 40 ± 8 (panel 2) nm, respectively. The FFT fades away (1 to 2) as the water layer thickness increases from 0 to 40 ± 8 nm. (B) Signal ratio vs spatial frequency, where the data was interpolated with a third-order polynomial in 1/signal ratio. The blue and red line represents where the signal ratio drops below the Rose criterion (SNR 3) for the first time, which occurs at the spatial frequency of 0.038 and 0.028 nm^{-1} for water layer thicknesses of 0 and 40 ± 8 nm, respectively.

As with the AuNPs, the liquid layer was thinned by adjusting the flow speed, recording the transmitted intensity, and calculating the thickness estimate using equation 5.1. The intensity scales of the two PS micrographs were set to correspond to the same maximum intensities, with the maximum being full transmission. The decrease in liquid layer thickness is observed by recording an increase in signal intensity. Additionally, the power spectrum of the micrograph gradually fades from FFT 1 to FFT 2, with an increasing liquid layer thickness (Figure 5.3 A). Determining the edge width resolution was not possible due to phase contrast

fringes of PS particles. Previously, the spatial resolution of LPTEM samples was characterized by the radial FFT dropping below the Rose criterion [210]. The spatial frequency at which the signal ratio falls below 3, are 0.038 and 0.028 nm^{-1} for 0 and 40 $\pm$ 8 nm liquid layers, respectively, Figure 5.3 B.

5.5   Dose effects in ELC

Beam induced effects are rampant within LPTEM. The radiolysis of water results in many species, including hydrated electrons (e_h^-), hydrogen radicals ($H^.$), hydroxyl radicals ($OH^.$), and hydrogen gas (H_2) from hydrogen radical combination, as discussed in section 2.3 [211]. The effects of electron induced damage on LPTEM imaging have been studied extensively to find a suitable imaging regime [212]–[214]. Commercially available PS particles were utilized, to characterize imaging conditions for low-contrast, beam sensitive specimens in ELC.

Once a controllable liquid layer was obtained in the ELC, the effect of cumulative dose on dry and wet PS particles was observed at a dose of 1 ± 0.08 e$^-$/Å^2 per frame. Figure 5.4 shows the average particle size. The details of the size calculation are given in section 5.3. In the case of dry PS particles, the initial average particle size at 1 ± 0.08 e$^-$/Å^2 was 111$\pm$5, which gets reduced to 89$\pm$7 after 30 frames. In contrast, the initial average particle size for wet PS particles was 109 $\pm$4 nm, whereas, after a cumulative dose of 23 e$^-$/Å^2 or 23 frames it got reduced to 82$\pm$5 nm. Subsequently, after a cumulative dose of 30 e$^-$/Å^2 particles were indistinguishable from the background. See Figure 5.5. This dissolution of the particles indicates that the PS particles undergo radiation damage as a function of dose, presumably via the reduction of the original particle mass due to beam-induced bond breaking and radiolysis. This dissolution for the PS particles was comparatively less pronounced in the absence of water. Note that radiolysis of water produces radical species that can accelerate the process of beam-induced damage [130], [215], [216] and the very presence of water provides a means for dissolution of the particle, i.e. solvation driven breakup of the particle as various bond breaking events lower the barrier to solvation.

(A)

(B)
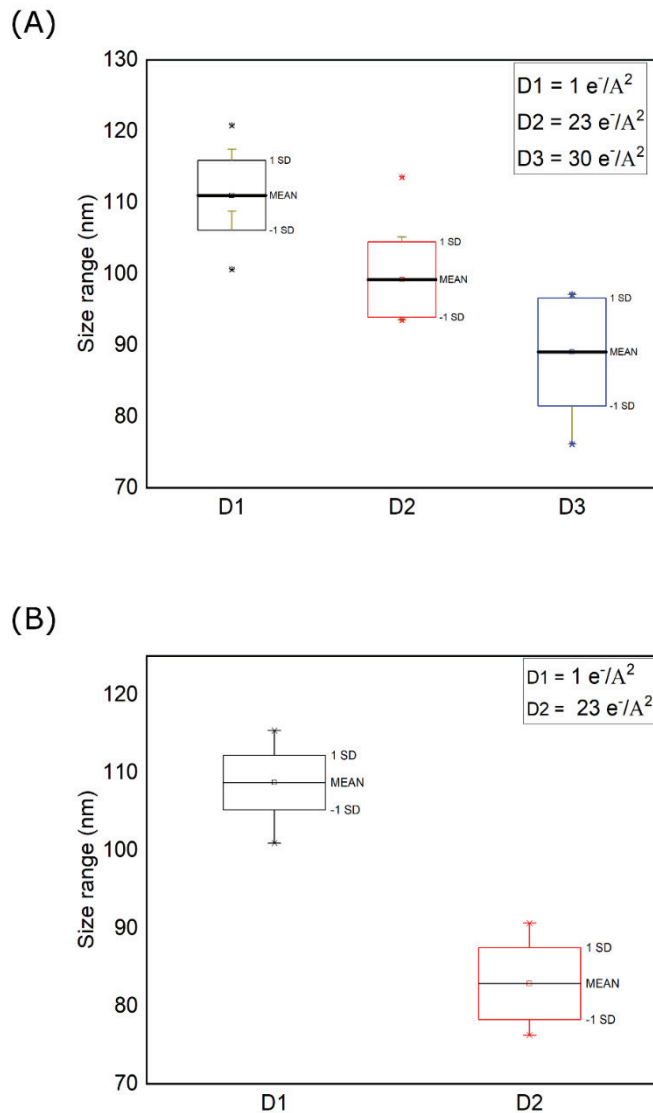
Figure 5.4: Average size estimation of dry and wet PS particles in the ELC. Whisker plots (A) for dry PS particles, (B) for PS particles with water.

To better quantify the cumulative dose effect on the degradation of the PS particles, the total signal and signal ratio was plotted against the spatial frequency. The details for calculating these quantities from the obtained micrographs are given in section 5.3. Figure 5.6 (A) shows how the total signal drops with respect to the cumulative electron dose. The dissolution of PS particles in water compared to its no water counterpart is evident from this data. Additionally, to show the degradation more quantitively, the signal ratio was plotted against spatial frequency in figure 5.6 (B). The spatial frequencies at which the signal ratio for the wet PS particles drops below its half value for the three different electron doses of 1, 23, and 30 $e^-/Å^2$ are 0.007 nm^{-1},

Sana Azim   Hamburg, 2020

0.006 nm^{-1}, and 0.004 nm^{-1}, respectively. The loss of spectral density indicates blurring of the particle edges and hence dissolution of PS particles which can be attributed to radiation damage as the cumulative electron-induced damage is increasing. These measurements on PS particles give an idea of the electron doses that can be used with organic and other low mass-thickness contrast samples in the ELC.
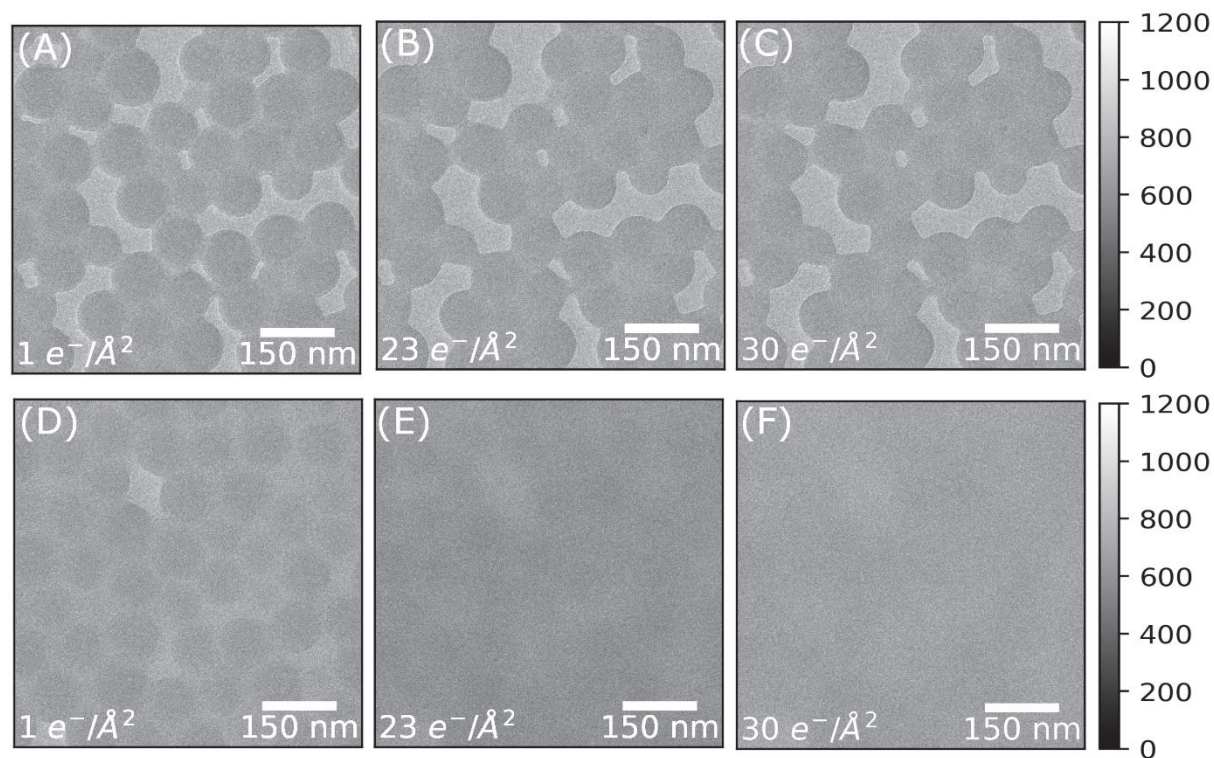
Figure 5.5: Polystyrene beads (100 nm) in the ELC without and with thin water layer.(A), (B) and (C) are micrographs of PS particles in the ELC without water. Panels(D), (E) and (F) show micrographs of PS particles with water at increasing cumulative electron dose. The images were captured at 1 e$^-$/Å^2 per frame, and a total of 30 frames were acquired.

(A)

(B)
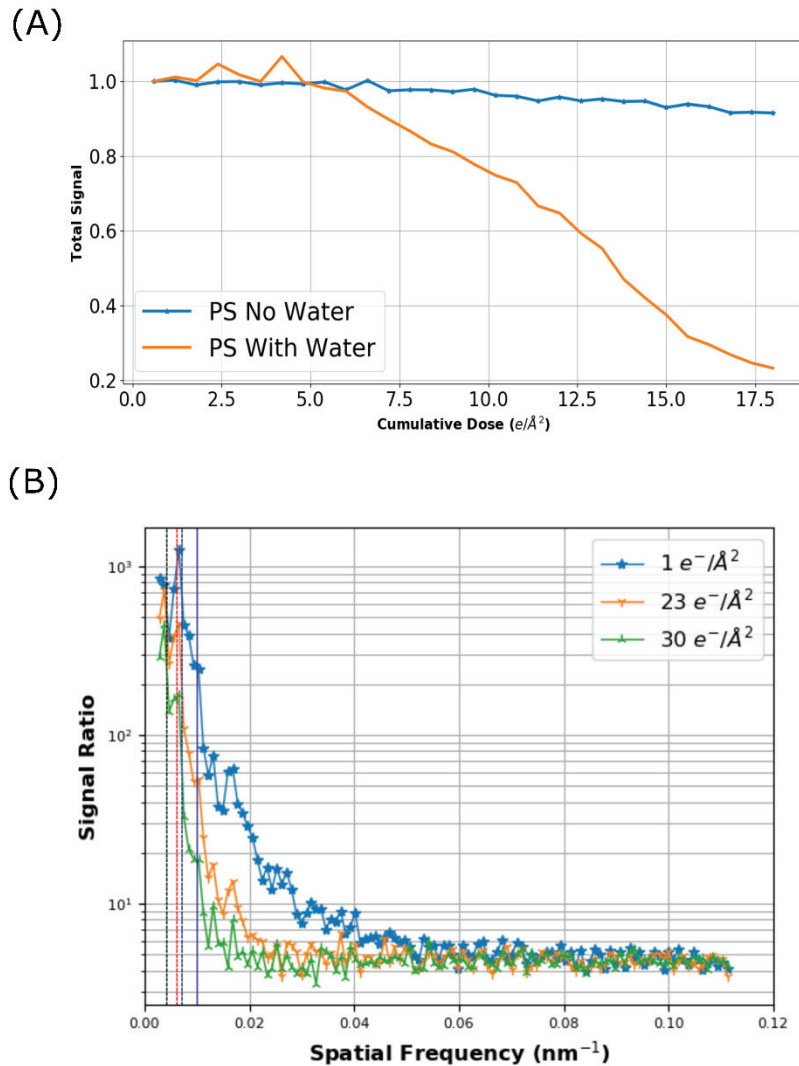
Figure 5.6: Total Signal and Signal ratio vs Spatial frequency for PS particles at increasing cumulative dose. (A) total signal for PS particles with and without water with respect to the cumulative electron dose. The graph illustrates the decay of the total signal for the two different cases as the cumulative electron dose is increased. No significant decay occurs when PS particles are dry while a considerable deterioration is observed for the wet case. Total signal drops to its half value at a cumulative electron dose of 23 e$^-$/Å^2, (B) Signal ratio with respect to the spatial frequency for wet PS particles, at three different (1 e$^-$/Å^2, 23 e$^-$/Å^2, and 30 e$^-$/Å^2) cumulative electron doses. It displays how the shape of the beads decays as the cumulative electron dose is increased, for the PS particles in-liquid. The signal drops below its half value at spatial frequencies of 0.007 nm^{-1}, 0.006 nm^{-1}, and 0.004 nm^{-1} for the electron doses 1 e$^-$/Å^2, 23 e$^-$/Å^2, and 30 e$^-$/Å^2, this decrease in the spatial frequencies for higher cumulative electron dose indicates the dissolution of the PS particles due to radiation damage.

After successfully imaging PS particles in ELC, the author performed in-liquid imaging of ferritin molecule, which is made up of 24 subunits, which form an octahedral sphere with an external diameter of 12 nm [217]. Micrographs of negatively stained ferritin dried on TEM grids and unstained ferritin in the ELC were collected. A dose of 0.3 e/Å^2 per frame was used in imaging ferritin in the ELC. The average particle size extracted from images of negatively stained ferritin is 12 nm, while the (unstained) ferritin in the ELC has a diameter of 8 nm. On measuring the inner core in the negatively stained micrograph, it turns out that the iron core is roughly 7.7 nm in size, which indicates that only the iron core is visible in the in-liquid micrographs recorded via ELC TEM.

Micrographs with horse spleen ferritin were recorded for two hours, the thin and homogeneous liquid layer allowed for the acquisition of 145 different locations over the whole viewing area. Representative micrographs at four-time points are shown in Figure 5.7. At each location, five micrographs were recorded with an exposure of time and dose of 250 ms and 0.3 e/Å^2 respectively, resulting in each region receiving a cumulative dose of 1.5 e/Å^2 after 1.2 seconds. The varying signal intensity with liquid layer thickness, as observed in the PS particles is used as a qualitative measurement of ELC liquid layer stability. The total signal of the ferritin micrographs as a function of time is shown in Figure 5.7 C.
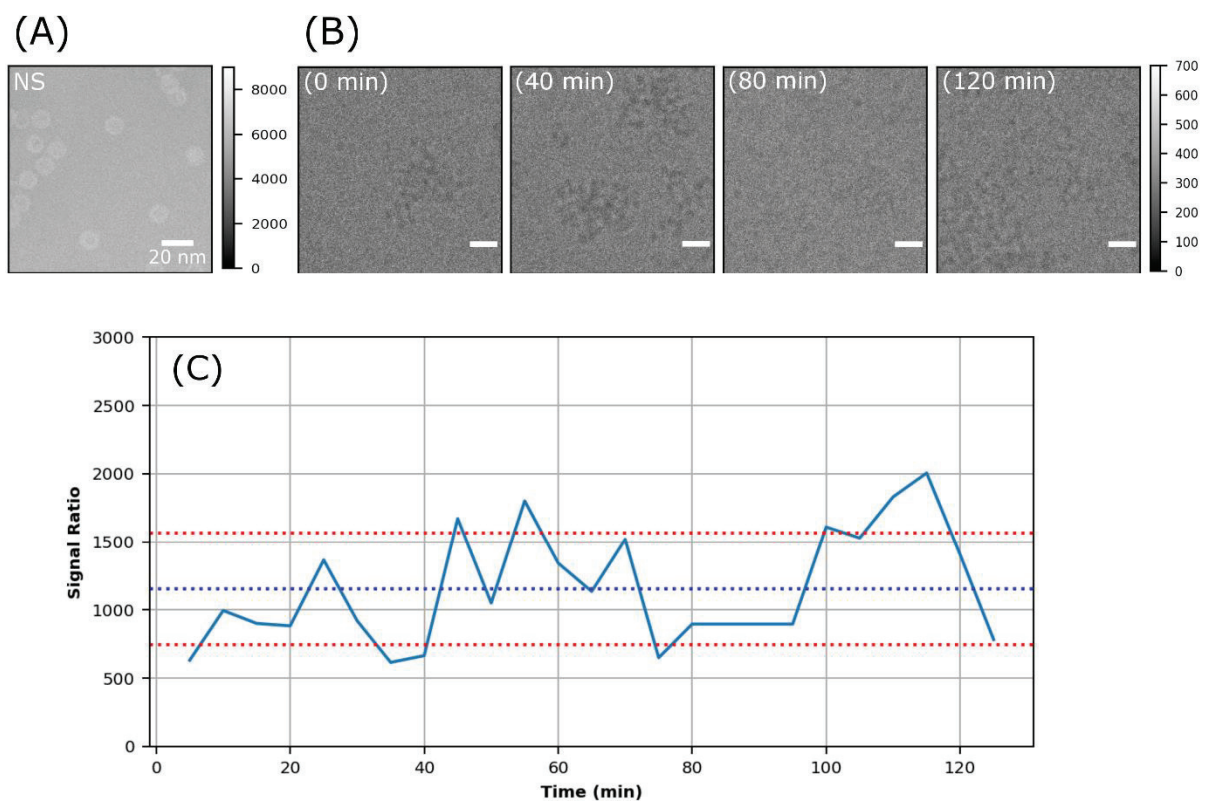
Figure 5.7: TEM micrographs of ferritin in ELC with a thin layer and Signal ratio vs time. (A) TEM micrographs of negative-stained ferritin on TEM Grid. & (B) Unstained ferritin in ELC. Micrographs in (B) show the ability of the ELC to maintain a thin liquid layer for 120 min., (C) Displays the stability in the signal ratio of ferritin micrographs vs time. The dotted red and blue lines mark the standard deviation and mean of the signal ratio 1156 ± 409).

The mean of the average signal intensity for signal ratio vs time plot is 1156 ± 409**.** The fluctuations in the signal ratio are within acceptable limits implying the liquid environment is stable for two hours.

5.6   ELC as an improvement to standard liquid cell

A traditional liquid flow cell setup was modified simply into an ELC via the addition of a 10 µm Kapton spacer and humidity control apparatus. The ELC enabled in-liquid imaging of different types of samples at doses not exceeding 30 e⁻/Å² per frame. The resolution improved with decreasing the liquid layer thickness. The resolution obtained with ELC for gold particles is better than previously reported LPTEM measurements at similar doses. The observations illustrate a great potential for using this approach to get nanometer resolution on hundreds of ms times scales. This setup can image structural dynamics on hundreds of ms timescales and longer, within electron dose limits. These results are in themselves an improvement over previously reported environmental cell designs. Additionally, ELC enables larger usable frames compared to standard LPEM with bulging, thereby opening up the possibility of larger dataset collection for applications such as ensemble averaging as well as capturing structural dynamics.

6 Determining the radial distribution of liquid water using electrons: A step towards solution chemistry

Water, as a simple molecule, one oxygen and two hydrogen atoms, has many exceptional properties, liquid at room temperature and expansion upon freezing being well-known. This atypical behaviour is due to the electrostatic attraction between hydrogen atoms and the negatively charged region of the oxygen atom, i.e. to form hydrogen bonds. The open, nearly tetrahedral geometry of the water molecule and the network formed by the hydrogen bonds are of great scientific interest. The hydrogen bond structure of liquid water is responsible for its special properties and ultimate for its support of all life on this planet. [218]. Additionally, hydrogen bonding is also responsible for the extraordinary solvent capabilities of water, which makes it popular in chemistry. Therefore, it is crucial to characterize the structure of liquid water and hydrogen bond dynamics at the molecular level. However, despite the recent progress in experimental and theoretical methodologies, a quantitative description of its structure has yet to be fully resolved.

In this chapter, the author presents the work from a submitted manuscript in which first authorship is shared with Dr. Michiel de Kock. The author developed the experimental setup, and the diffraction data were collected by the author in collaboration with Dr. Günther Kassier. Dr. Michiel de Kock analyzed the resulting data. This study aimed to determine the radial distribution functions for liquid water, to directly measure the hydrogen bond distribution, at ambient temperature using electrons. Unlike X-rays, electrons are charged particles and therefore interact with the nucleus of an atom and not the electronic orbitals. Therefore, electron diffraction does not impose a lower limit on the atomic numbers of the materials under investigation. For water, this would mean that electron scattering data is sensitive not only to the O-O pair distributions but also to O-H or even H-H. Obtaining such details can provide a better understanding of the hydrogen bond structure. In fact, we have the opportunity to directly measure the hydrogen bond distribution through the OH intramolecular pair distribution (bond length approximately 1 Å) and the O—H intermolecular pair distribution (bond length approximately 1.8 Å), as will be seen below.

Since the aim is to understand the network of hydrogen bond structure in liquid water, it is, therefore, essential to provide the theory of hydrogen bond formation, which is described in part 6.1. It is also of immense importance to understand how the hydrogen bonding maintains the liquid structure of water and gives it several peculiar properties not present in other liquids,

which is treated in section 6.2. In the last part of this chapter, the details of the electron diffraction experiments are discussed. A brief description of the analysis done to extract the radial distribution curves has also been provided. Lastly, the O-O and O-H peaks in the distribution curve is treated and compared to that reported in X-rays and previous electrons studies. A brief description is also given about the coordination number computed using the radial peaks.

6.1 Hydrogen bond concept

In order to understand the hydrogen-bond dynamics of water, one must first understand a hydrogen bond. The hydrogen bond (H-bonds) is a distinct type of dipole-dipole attraction between molecules. It is a bond between an electron-deficient hydrogen atom and a region of high electron density. To be precise, it is of type X–H•••Y, where X and Y are the electronegative elements with Y holding one or more electron lone pairs. H-bonds in which X, Y are N, F, or O, are the most studied [219]–[222]. There are two different types of H-bonds: intermolecular and intramolecular. An H-bond formed between two separate molecules X–H and another molecule containing Y atoms are called intermolecular H-bonds.

In contrast, a bond formed between X–H and Y, when they are part of the same molecule, is called an intramolecular H-bond. The former is responsible for the strong interactions between molecules in protonic liquids and can heavily influence the temperature magnitude and heat of evaporation of that liquid. This effect is especially marked in the case of liquid water [218], which has the highest number of possible H bonds per mass of any substance. The hydrogen bonding in water not only modifies the interactions between the molecules it becomes essential in defining global minima of active biological molecules, the active structures leading to living systems. This intimate connection is apparent in large molecules like DNA, protein or aromatic molecules such as Schiff base and even smaller molecular systems such as maleate anions [218], [223], [224]. In this chapter, the focus is kept on intermolecular hydrogen bonding as the aim is to determine the hydrogen bonded structure of liquid water that governs its special properties.

The electronic picture in case of H-bond (X–H•••Y) can be explained in terms of four crucial parts which are essential in its formation. The first step is the polarization of the nonbonding orbital of Y by the dipole moment of the X–H group. Thereafter is the deformation of that nonbonding orbital due to this dipole moment which is followed by the appearance of quantum forces due to the overlap of electronic orbitals X–H and Y. In the final step, the partial

transfer of an electron from the nonbonding orbital of the acceptor atom of Y to the donor molecule X–H take place. The transfer of electron in a first approximation occurs towards the antibonding orbital of X–H followed by an s-p rehybridization of the acceptor atom on Y. Because of this rehybridization, the X–H covalent bond is weakened inducing a weakening of the force constant that binds X and H. This also increases the equilibrium distance between X and H and as a consequence the variation of the electric dipole moment.
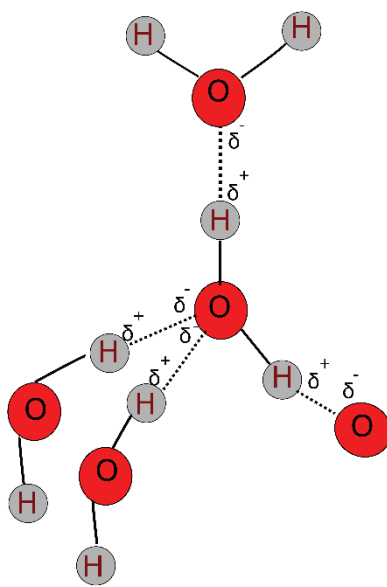
Figure 6.1: Schematic showing hydrogen formation in liquid water, where the dotted line shows the hydrogen bond and solid line the covalent bond. A slight positive charge on hydrogen is shown by δ^+ while δ^- is the small negative charge on the oxygen.

6.2 Hydrogen bonding and structure of liquid water

Water is the only compound that can exist in all three physical states of solid, liquid and gaseous under natural conditions. The unique properties of water come from the fact that water molecules have dipoles that assist it in making intermolecular hydrogen bonding its condensed phase, see Figure 6.1. Water has a dipole moment of 1.83D along its axis of symmetry. The H-O-H angle in it is 104.5° which is somewhat less than the 109.5° of a perfect tetrahedron.

In comparison, two nonbonding orbitals stay on its O-atom and are each occupied by two lone-pair electrons. It is because of this that the water molecule has two acceptor sites for H-bonds and two donor sites. This structure of the water molecules offers four sites for it to establish H-bonds with any of its neighbouring molecules. Consequently, a dense three-dimensional H-bond network is formed, which is responsible for the stability of the essential configurations of biologically active molecules at room temperature. Also, the flexibility

required in these configurations comes from the flexibility in the H-bond network. We can thus call the water molecule a paradoxical molecule as it is small, with many complicated ways to bind to other molecules, and yet it exerts its influence over relatively huge molecules up to the mesoscale of biological functions. There are long range dynamical effects at play, which ultimately are all determined by the hydrogen bond network of water. It is the long range correlations imposed by hydrogen bond that has made this problem so difficult to understand as well underscores the importance of resolving the hydrogen bond network of liquid water[218].

To be clear about structural relationships, water being a liquid at ambient conditions does not have a structure in terms of fixed average atomic positions as solids do. Nonetheless, they exhibit characteristics spatial and temporal coherence between atomic and molecular centres which are governed by intra and intermolecular interactions, respectively. Scattering from short-wavelength radiations such as X-rays, neutrons and electrons can directly measure these correlations. The signal from scattering measurements are comprised of both intra and intermolecular interactions. But as explained in section 6.1, only the intermolecular part is relevant for gaining insight about the structure of liquid water. Therefore, to evaluate the structure, the value for intramolecular interactions must be subtracted. The X-rays and electron scattering measurements cannot provide separate structure factors (e.g. O-O, O-H and H-H) as they are not sensitive to differentiate between the atoms. While the neutron scattering measurements can do this using isotope substitution [225], [226]. The neutron data is usually combined with the X-ray measurements to get high precision O-O pair distribution [227].

Electron scattering can support the X-ray and neutron measurements by providing a separate third piece of information for the determination of partial pair correlation functions. In regards to the molecular correlation functions sensitive to H atom scattering processes, it can reveal more information than X-rays but not as much as the neutrons. Another advantage of using electron diffraction lies in its short incident wavelength ($\lambda \sim 0.05$), which can provide a much more extensive range of scattering information ($k \sim 30 \, \text{Å}^{-1}$) or intrinsically much higher spatial resolution. This, in turn, can be useful in the determination of structures of more complicated liquids [228]. Despite the pros, that electrons have as a probe for structural determination of liquids, there have been very few studies so far. The reason for this lies in the fact that electrons have shallow penetration depths compared to X-rays. Thereby posing the restriction of very thin liquid samples in a high vacuum. In 1974, Lengyel and Kalman reported electron diffraction on liquid water in an environmental chamber with < 100keV electrons, but

their system lacked longevity as the water layer thickness could only be maintained for few seconds [228], [229]. As discussed in chapter 5, the ELC provides a thin and stable liquid environment for a longer time and therefore is a suitable tool to perform electron diffraction on liquid water.

Additionally, previously reported work failed to address the problem of multiple scattering, which is considerable [228]. The work presented here overcomes both these issues, thereby allowing the structural determination of all types of liquid samples. There has been a recent work reported by Nunes *et al*., overcoming some of the problems stated above using a mega-electron-volt setup to increase the penetration depth and allow high velocity liquid jets [149]. Still, the experimental setup is complicated, requiring liquid jets, which still have uncontrollable pathlengths, and significant multiple scattering effects that are difficult to separate. Whereas, the technique reported is a simple table-top approach easily adaptable to any commercial TEM.

6.3   Static electron diffraction on liquid water

As discussed above, the electron diffraction measurements were performed utilizing an in-house developed environmental liquid cell (ELC) assembly and technique, details about which are provided in chapter 5. The ELC setup includes silicon nitride flow-cell technology which is based on that of Mueller *et al*. [57]. The flow-cell comprised of a pair of freestanding rectangular windows (30×100 μm^2) on 3×8 mm^2 rectangular platform of silicon. The thickness of the silicon nitride film used was 20 nm, and cell incorporate flow ports (inlet/outlet) for easy exchange of liquid/gas. The silicon nitride/silicon chips were design in-house and fabricated to our specification by Inc.SiMPore Inc. USA.

The sample for the measurements was prepared by drop-casting 1 µl of deionized water on the bottom chip. A custom-shaped 10 µm thick polyimide (Kapton) spacer was placed in between the two chips. This ELC assembly was then sealed in our custom-built ELC sample transfer arm. One end of the flow outlets of the ELC transfer arm was connected to a humid air source controlled via a flow meter while the other was connected to vacuum pump. The setup has been described in Inayoshi *et al*., and in greater detail elsewhere [Azim *et al*., submitted].

The electron scattering measurements were collected on a JEOL JEM-2100 TEM operated at 200 keV and fitted with a TVIPS TemCam F216 camera. Darkfield and flatfield calibration was done on the camera before the data acquisition. The camera length was calibrated using a polycrystalline aluminium film. The electron dose rate for the scattering

measurements was measured to be 0.09 ± 0.01 e$^-$/Å^2. All the diffraction patterns were recorded with an exposure time of 1 s and an effective camera length of 33.3 cm. The thickness of the water layer was estimated during the in-situ measurement by recording real-space images and determining their total image intensity counts I and I_0, corresponding to the cases with and without an objective (half-angle of acceptance $\theta = 12.6$ mrad) aperture respectively. The intensity ratio was used to compute the thickness of silicon nitride and water layer by the log-ratio method and utilising the scattering model, which has been described at length in section 5.3 of the previous chapter.

The prepared ELC was transferred to the TEM using the sample transfer arm. To be able to measure an empty silicon nitride required for background subtraction, the pressure was set to -400 mbar and the flow rate to 30 ml/minute. To be sure that the silicon nitride was empty, the intensity ratio (I/I_0) was measured, which was 0.88 ± 0.01. The corresponding thickness computed using the scattering model was 24 ± 2 nm. The log-ratio method and the scattering model underestimates the thickness of silicon nitride by 21 % as described in section 5.3. Therefore, 40 nm film measures as 24 nm. Thereafter, the flow rate was reduced to about 1 ml/minute and adjusted until a stable scattering ratio of $I/I_0 = 0.70 \pm 0.02$ was obtained. The ratio corresponded to 160 ± 20 nm of water thickness. Twenty diffraction micrographs were collected under these conditions for analyzing the structure of liquid water.

This point onwards, the author provides details of the analysis involved in determining the structure of liquid water, i.e., finding the position and height of O-O and O-H pair distribution function. In electron diffraction, the most convenient quantity to describe the angular distribution of the scattered electrons is the differential cross-section and the mean free path length, a basic theory of which has been provided by the author in chapter 2. Electrons that pass through an element of area $d\sigma$ of the parallel incident beam area will be scattered into a cone of solid angle $d\Omega$. The ratio $d\sigma/d\Omega$ is the differential cross-section and is a function of the momentum transfer $Q = 4\pi \sin(\theta/2)/\lambda$, with the scattering angle θ and the electron wavelength λ. A liquid has no structure with respect to a fixed origin since the atoms are continually moving. Still, the atoms have well-defined sizes and closest distances of approach, hence liquids have a definite structure relative to the origin at the centre of the average atom. This type of structure is expressed by a radial distribution function $4\pi r^2 \rho(r)$ such that $4\pi r^2 \rho(r)dr$ is the average number of atomic centres between distances r and $r + dr$ from the centre of an average atom. The scattering cross-section for N independent atoms without interference, A(Q), is given by the following

$$\frac{1}{N}\frac{d\sigma}{d\Omega} = A(Q) + B(Q)\int_0^\infty 4\pi r^2 \rho[g(r)-1]\frac{\sin(Qr)}{Qr}dr, \qquad 6.3$$

Where B(Q) is the weighing factor and ρ is the average number density of the sample. Although the choice of the weighing factor, B(Q), is arbitrary, still, crucial. If neglected, the scattering cross-section will only show the correlations between the electrons and the nucleus and not the atoms themselves. In X-ray diffraction, Equation 6.1 was first derived by Zernike and Prins and applied by Debye and Menke on liquid mercury [226], [230], [231].

In the literature A(Q) and B(Q) have been defined in different ways depending upon the focus of the investigation, here they are defined as atomic and molecular [232]. In the atomic scheme only, the self-scattering and the incoherent scattering are subtracted and is defined as,

$$A_{at}(Q) = \sum_\alpha c_\alpha f_\alpha^2(Q) + \sum_\alpha c_\alpha S_\alpha(Q) \qquad 6.4$$

where the sum runs over the different atoms in the sample, with the electron coherent scattering factor, *f(Q)*, the incoherent scattering factor, *S(Q)*, and the atomic concentration c_α. The weighing factor, *B(Q)*, is given by

$$B(Q) = \left[\sum_\alpha c_\alpha f_\alpha\right]^2 \qquad 6.3$$

representing the electron scattering without interference. For the molecular scheme, the intra-molecular interference is also subtracted, and therefore A(Q) is constructed using the independent atom approximation or Debye model,

$$A_{mol}(Q) = \sum_{i,j} f_i(Q)f_j(Q)\frac{\sin(Qr_{i,j})e^{-b_{\alpha,\beta}Q^2}}{Qr_{i,j}} + \sum_\alpha c_\alpha S_\alpha(Q) \qquad 6.4$$

With the Debye-Waller factor, $b_{\alpha,\beta}$, and the molecular bond lengths $r_{i,j}$ between atom i and j. The atomic or molecular structure factor is defined as,

$$S_{at/mol}(Q) - 1 = \frac{\left(\frac{d\sigma}{d\Omega} - A_{at/mol}(Q)\right)}{B(Q)} \qquad 6.5$$

The relation in Equation 6.1 can be inverted via a Fourier transform connecting this structure factor to the radial distribution function, which is given as

$$g_{at/mol}(r) = 1 + \frac{1}{2\pi^2 r \rho} \int_0^\infty Q\big(S_{at/mol}(Q) - 1\big) \sin(Qr) dQ \qquad 6.6$$

The structure factor of water can be decomposed into individual contributions of different bond lengths,

$$S_{at/mol}(Q) = w_{OO}S_{OO} + w_{OH}S_{OH} + w_{HH}S_{HH} \qquad 6.7$$

The weighing factors are defined as,

$$w_{OO} = \frac{f_O^2(Q)}{9B(Q)}, w_{OH} = \frac{4f_O(Q)f_H(Q)}{9B(Q)}, w_{HH} = \frac{4f_H^2(Q)}{9B(Q)} \qquad 6.8$$

These partial structure factors can then be separately transformed to obtain the pair distribution functions g_{OO}, g_{OH}, g_{HH}. The decomposition requires different data sets which is not possible with X-rays or electron scattering measurements. The reason being their inability to distinguish between the atoms, and therefore usually the neutron scattering data is used in combination with X-rays measurements, as the latter can do so with isotope substitution [225], [232].

As stated in section 6.2, the work reported here takes into account multiple scattering in analyzing the electron diffraction data, while other similar electron studies failed to do so [228]. Thereafter, the author briefly describes the details involved in doing so. A detailed explanation for the same has been provided in our submitted manuscript [De Kock *et al.*]. Assuming that the scattering is concentrated on small-angle, i.e., $Q \approx 2\pi\theta/\lambda$, the scattering form factor can be normalized by dividing it by the total scattering,

$$\sigma = \frac{\lambda^2}{4\pi^2} \int_0^\infty 2\pi A(Q) Q dQ \qquad 6.9$$

Which gives,

$$A_1(Q) = \frac{\lambda^2}{4\pi^2\sigma} A(Q) \qquad 6.10$$

Sana Azim   Hamburg, 2020

The total scattering is related to the mean free path length with $L = 1/\rho\sigma$. The angular distribution for n scattering events is given by n two-dimensional convolutions of single scattering distribution, $A_1(Q)$, with itself [97].

$$A_n(Q) = A_{n-1}(Q) \otimes A_1(Q) \qquad \text{6.11}$$

The multiple scattering form factor is thus obtained by weighing all possible scattering events with their probability of occurrence and given as,

$$A^\star(t, Q) = exp\left(\frac{-x}{L}\right) \sum_{n=1}^{\infty} \left(\frac{t}{L}\right)^n A_n(Q)/n! \qquad \text{6.12}$$

The multiple scattering form factor depends on the specimen thickness, t. Therefore, Equation 6.1 can be re-written to include multiple scattering:

$$\frac{4\pi^2}{\lambda^2 I_0} \frac{dI_{exp}}{d\Omega} = \sigma_A A^\star(t, Q) + \sigma_B B^\star(t, Q) \int_0^{\infty} 4\pi r^2 \rho[g(r) - 1] \frac{sin(Qr)}{Qr} dr \qquad \text{6.13}$$

Where I_{exp} is the intensity observed in the detector, I_0 is the incident intensity, and $B^*(t, Q)$ is the multiple scattering version of the weighing factor. Also, the structure factor with multiple scattering contributions is given as,

$$S(Q) - 1 = \frac{\left(\frac{4\pi^2}{\lambda^2 I_0} \frac{dI_{exp}}{d\Omega} - \sigma_A A^\star(t, Q)\right)}{\sigma_B B^\star(t, Q)} \qquad \text{6.14}$$

After establishing the theoretical basis for separating the useful contributions (intermolecular) contained in an electron scattering signal, the author now utilizes the same to extract the pair distribution functions for silicon nitride. The contribution from silicon nitride can then be removed to obtain pair distributions for liquid water. Initially, the atomic scattering factors ($A_{SiN}(Q)$) and normalization factors ($B_{SiN}(Q)$) are constructed from the elastic form

Sana Azim   Hamburg, 2020

factors given in Kirkland [122], and the inelastic X-rays form factors as provided in Wang *et al.* [233].

$$A_{SiN}(Q) = \frac{3}{7}\,[S_{Si}(Q) + f_{Si}^2(Q)] + \frac{4}{7}[S_N(Q) + f_N^2(Q)]$$

$$B_{SiN}(Q) = [\frac{3}{7}\,f_{e,Si}(Q) + \frac{4}{7}\,f_{e,N}(Q)]^2$$

6.15

The elastic, inelastic and total mean free path (mfp) lengths for silicon nitride can thus be calculated to have values 96 nm, 69 nm and 40 nm respectively. Thereafter, an atomic scattering model is built by computing the atomic scattering factor and normalization factor with multiple scattering effects, utilizing the mfp and the known thickness of silicon nitride (25 nm). The experimental data collected with empty silicon nitride windows is fitted to this atomic scattering model by minimizing the fit function,

$$\left[\frac{a_0 I_{exp}(Q) - a_1 - a_2/Q - A_{SiN}^{\star}(t,Q)}{B_{SiN}^{\star}(t,Q)\delta I_{exp}(Q)}\right]^2$$

6.16

Where $I_{exp}(Q)$ and $\delta I_{exp}(Q)$ are the experimental error, respectively, the fitting has an electron dose scaling term, a_0, which is different for each diffraction micrograph. Two polynomial constants, a_1 and a_2 are included to compensate for dark current and non-linear effects in the camera response. These are kept the same for all the micrographs. The data from twenty diffraction micrographs are added together using weighted mean with the inverse variance as the weight. To estimate the error, half the square of the polynomial is added to the variance in each bin. Since the atomic model does not include any interference effects, therefore it does have the expected discrepancies for smaller Q, see Figure 6.2.

The atomic structure factor for silicon nitride is obtained by subtracting the atomic model from the experimental data and dividing with the normalization factor,

$$S'(Q) - 1 = [S^{\star}(Q) - 1]M(Q)$$

6.17

The atomic radial distribution function for silicon nitride is then calculated,

$$g_{SiN}(r) - 1 = \sum_{Q=Q_{min}}^{Q_{max}} \frac{1}{2\pi^2\, r\rho} Q(S'(Q) - 1)sin(Qr)\, \delta Q \qquad 6.18$$

The observed peaks for Si-N, N-N and Si-Si at 1.7 Å and 2.95 Å matches well to those obtained from X-ray measurements, which have a Si-N height at 1.75 Å while the N-N and Si-Si peaks lie at 3 Å [234].

(A)
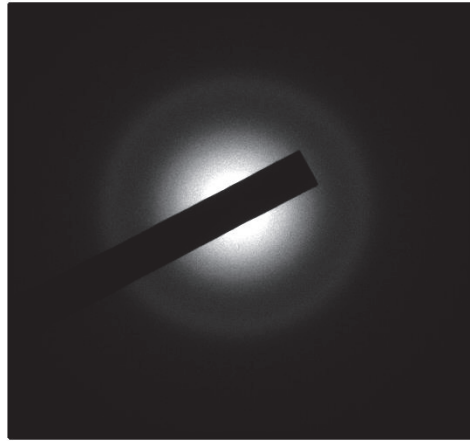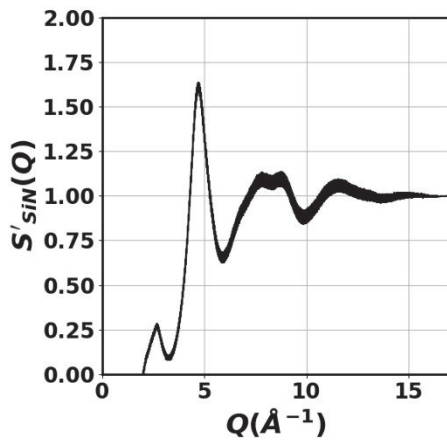
(B)   (C)
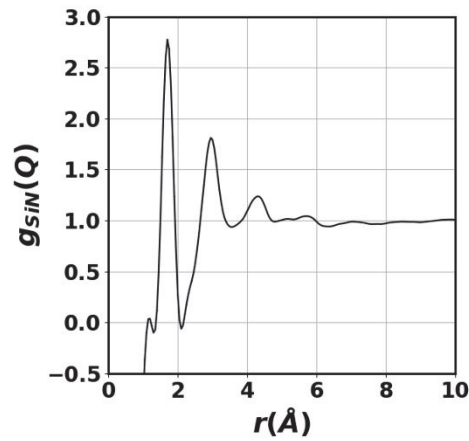
Figure 6.2: (A) Diffraction micrograph collected at 33.3 cm camera length, (B) Structure factor, (B) the corresponding radial distribution function for silicon nitride film. In (B) there is a sharp drop present below 1 Å which can be attributed to the errors originating from the theoretical model, luckily there is no bond length in that region. The Si-N peak is observed at 1.7 Å with a height of 2.7, while the N-N and Si-Si bond lengths combine at 2.9 Å having a height of 1.8. The Si-N-SI and N-Si-N bond length appear to be at 4.3 Å with a height of 1.2.

Sana Azim   Hamburg, 2020

Next step was the subtraction of this silicon nitride background from the experimental data, which comprises of signal from water and silicon nitride. For doing this, first, the radial distribution is transformed back to the diffraction space, where the atomic model is added to it, giving the silicon nitride diffraction data for smaller and larger Q values, $C_{SiN}(Q)$. The elastic and inelastic scattering values, $C_{water}(Q)$, for water can be directly imported from Wang *et al.* Therefore, the independent atom model for constructing the molecular scattering is not required [233]. The molecular scattering of the two can be added in the Fourier space as,

$$C_{\widetilde{water+SiN}} = c_{SiN}\widetilde{C_{water}} + \widetilde{C_{SiN}}c_{water} + \widetilde{C_{SiN}}\widetilde{C_{water}} \qquad 6.19$$

Here $\tilde{C}$ denotes Fourier space variable, c_{water} and c_{SiN} are the probabilities to not scatter in the water and silicon nitride layer respectively. For the normalization factor, one has to separate the effects of the hydrogen and water components. This is done by transforming the X-ray elastic scattering factors from Kirkland using the following equation from Sorenson [122], [235].

$$f'_{X,\alpha}(Q) = f_{X,\alpha}(Q)\left[1 - \frac{a_\alpha}{z_\alpha}exp\left(\frac{-Q^2}{2\delta^2}\right)\right] \qquad 6.20$$

Where α is the atom species, this is then transformed to get the electron scattering factors using the Mott-Bethe formula [122].

$$f'_e(Q) = \frac{2}{a_0}\left[\frac{Z - f'_X(Q)}{Q^2}\right] \qquad 6.21$$

The transformation was done to realize the amount of charge redistribution occurring in the individual form factors when the hydrogen bonds to the oxygen atom. The parameters used here are the same as used by Sorenson *et al.*[235]. Thereby, the modified form factor from which the normalization is constructed is,

$$B_{watre} = \left[\frac{1}{3}f'_O(Q) + \frac{2}{3}f'_H(Q)\right]^2 \qquad 6.22$$

The same procedure is applied to the normalization factors as applied for empty silicon nitride case to obtain, B^*_{water}, and $B^*_{water+SiN}$. The elastic, inelastic and total mean free path lengths computed for water are 436 *nm*, 230 *nm*, and 151 *nm*. The experimental data were fitted to the model by minimizing the loss function, as it was done for the silicon nitride. Still, for water, the exact thickness is not known, which is the most significant source of uncertainty for the outcome. The rest of the procedure of adding the micrographs together using weighted means, with weight given by the inverse variance, remains the same here as was done for the silicon nitride case. Taking the water thickness to be 130 *nm*, which is still close to of the computed value taking into account the error bar (160 ± 20), minimizes the structure below 1 Å in the radial distribution function.

(A)
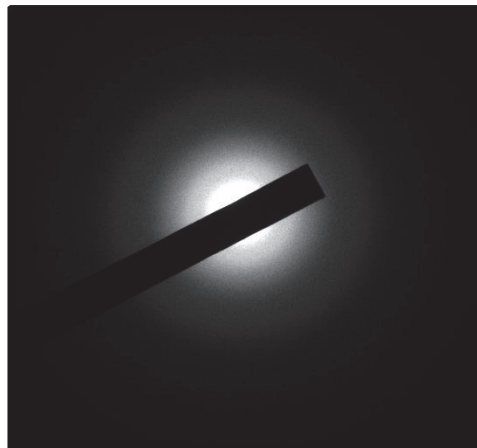
(B)
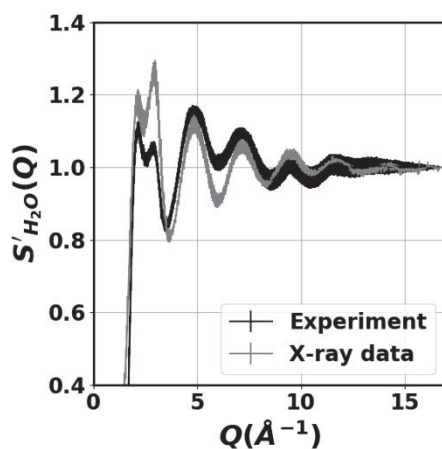
(C)
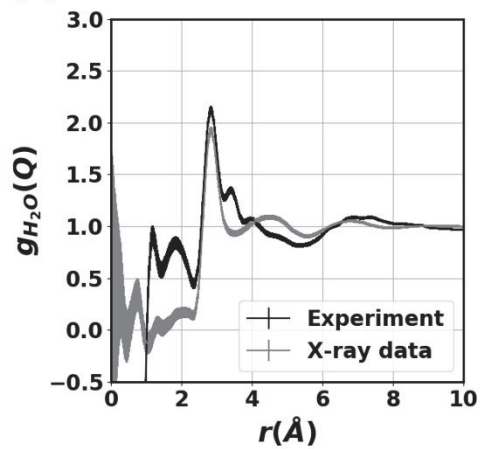
Figure 6.3: (A) Diffraction micrograph collected at 33.3 cm camera length, (B) Structure factor, (C) the corresponding radial distribution function for liquid water. Please note that the

micrograph is raw, i.e., silicon nitride background is not yet subtracted. B) compares the structure factor determined using the electron scattering to that of X-rays data taken from Soper *et al.* [236]. C) the drop below 0.8 Å, in the radial distribution function of the electron scattering data is expected to originate from the fitting procedure and the unknown silicon nitride scattering. The O-O peak at 2.8 Å in the electron data appears to be in good agreement with the X-ray scattering, while the intermolecular O-H bond length, the key hydrogen bond, is visible at 1.8 Å. This feature is not observable in the x-ray data

The structure factor and its corresponding radial distribution function obtained are compared to X-ray data from Soper, see Figure 6.5 [236]. In part A of figure 6.5, for the electron diffraction data, the first double peak observed between 2 Å and 3 Å is suppressed, and the dip at 6 Å is not as deep as compared to the X-ray data. The difference here can be explained in terms of the increased sensitivity of electron diffraction technique to the O-H bond length. In part B of the figure, the radial distribution of the electron and X-ray scattering data is compared.

6.4   Predicting the structure of liquid water

The structure of liquid water could be predicted in terms of the total number of hydrogen bonds a water monomer can form with its neighbouring water molecules. The radial distribution functions obtained from the scattering data contains information about intra- and intermolecular interaction occurring in liquid water at any instance of time. The intramolecular contributions have been subtracted. Therefore, we speculate the peak at 1.18 Å in Figure 6.5, to be an artefact caused by the sharp drop-off of the radial distribution function for electron scattering data below that value. The reason for this could be left-censoring of the silicon nitride data, and the fitting procedure adapted. In the radial distribution, we see two well-defined peaks. The first one at 1.84 Å can be attributed to the hydrogen bond between the hydrogen atom of the reference water monomer with the oxygen atom of its nearest neighbour. Neutron scattering data by Soper et al. gives the O•••H bond length as 1.85 Å. When this is compared to the electron scattering data presented here, a relative error of 0.5 per cent is seen, suggesting a good match [237].

On the other hand, recently reported electron diffraction measurement on the water by Nunes et al., do not observe a well-defined peak for the O•••H bond length. They report a shoulder at 1.8 Å, [155], [236], [237]. Detection of the O•••H peak with a reasonable accuracy highlights the superiority of electron scattering over X-rays. With ELC TEM, a spatial resolution ($2\pi/Q_{max}$) of 0.4 Å was achieved, and longer integration times could increase this range significantly. In comparison, Nunes et al. can only get 0.6 Å, corresponding to a Q_{max} of

10 Å^{-1} and will be limited, even with relativistic electrons, due to instabilities in the jet and its effect on multiple scattering contributions. Thus, we see that the ELC is a simple, robust, powerful tool to investigate in-liquid diffraction compared to liquid jet techniques [155]. The second well-defined peak at 2.84 Å displays the O•••O internuclear distance between two neighbouring water molecules. The peak width is related to the experimental parameter Q_{max} and the spread of atomic distances for a given structure. The intermolecular bond lengths in water are not well-defined due to the very nature of the hydrogen bonding, which affects charge distribution and bond strength. This effect leads to a wide range in the intramolecular and intermolecular bond lengths, which is why the peaks corresponding to the oxygen-hydrogen and oxygen-oxygen intermolecular distances are broad [238]. The presented results are in good agreement with molecular dynamics simulations as well as X-ray and neutron scattering experimental measurements [236], [238], [239]. The number of hydrogen and oxygen atoms around the reference water monomer can be calculated using the coordination number [236],

$$N_c = 4\pi\rho \int\limits_0^{r_{min}} r^2\, g_{ij}(r)dr \qquad\qquad 6.23$$

where r_{min} is the position of the first minima of the peaks, and ρ is the number density of water. Using Equation 6.23, and the radial distribution function which marks the peak positions and positions of the respective first minima for the O•••H (2.45 Å) and O•••O (3.45 Å), the coordination numbers obtained are 1.91 and 5.01, respectively. From these numbers, it is evident that the O•••H distribution with a peak at 1.84 Å comprises of around 1.91 hydrogen atoms out to a distance of 2.45 Å from the oxygen atom sitting at the origin. Further, the O•••O distribution with a peak at 2.84 Å has approximately 5.01 oxygen atoms out to a distance of 3.45 Å from the central oxygen atom. These numbers and ranges propose a tetrahedral structure, i.e., approximately four hydrogen bonds per water molecule at any instant of time. This structure is in a good agreement to the neutron scattering measurements reported by Soper *et al*. in 1986 and with the combined results obtained from X-rays, neutron and Monte Carlo simulations, by Soper *et al*. published in 2008 [237], [240]. The predicted value is somewhat above the maximum limit of 2 hydrogen bonds per molecules, as suggested by Wernet et al. [241], [242]. A comparative molecular dynamics simulation, in parallel with a temperature

dependence, can be done to get more insight into the dynamic nature of the hydrogen bonding of liquid water.

7   Observing aggregation dynamics in γS crystallin molecules

Protein aggregation is known to be the root cause of many prevalent diseases such as Alzheimer, Parkinson and sickle cell anaemia. Cataract, which is the disease responsible for 48% of the world's blindness, is caused by aggregation of lens crystallin proteins [243]–[245]. With the onset of ageing, covalent protein damage starts accumulating via specific pathways which are not entirely known [244]. The present research findings speculate these to be UV radiation, mutations or metallization.

There have been a few studies in the past focused on damaged caused in the eye lenses due to protein aggregation induced via various radiations [246]–[250]. Despite these studies, not much insight has been gained for the actual mechanism involved in aggregation. To this end, work has been done by the author in collaboration with Dr. Günther Kassier (MPSD) and a team from Department of Chemistry, UCI, to investigate the aggregation mechanism and the types of aggregates formed when human γS-crystallin is exposed to ultraviolet (UV) A and B radiations. The morphology of these aggregates is also compared to aggregates formed by acidic pH, mutation and metal binding. This chapter is based on the author's contribution to the recently reported work that Human γS-crystallin copper binding helps buffer against aggregation caused by oxidative damage [251].

In the first section, the author provides a short introduction to the different crystallin proteins present in the human eye lens and why is it necessary to study the aggregation mechanism involved. In this entire study, an important aspect was making the protein aggregates and being able to get TEM snapshots of them at several timepoints during their formation. The author has described the different methods and procedure involved in preparing the samples in section 7.2. Subsequently, in the next three sections, the author gives a thorough description of the experimental findings obtained. To elaborate, in section 7.3, the author compares the aggregates formed via UV to those of pH-induced. Thereafter, the aggregates formed due to the presence of point mutations are discussed by the author. The discussion is done keeping in mind the aggregates formed via the other two methods. Finally, the author presents the results on aggregation caused due to metal addition.

7.1   Importance of studying aggregation in γS-crystallin

The transparency in the human eye lens relies on the proteins present in there. Mainly, the responsible ones are α-crystallin and βγ-crystallins. These are present at a concentration as

Sana Azim   Hamburg, 2020

high as 400 mg/ml in a grown up's lens fibre cells [246], [252], [253]. The β- and γ-crystallins are supposedly the structural proteins. At the same time, α-crystallin is believed to be involved in additional chaperone activity which is to bind the misfolded proteins to avoid aggregation. When aggregates of such partially unfolded or covalently damaged proteins are formed, the lens loses its transparency, causing cataract. The focus of this study is γS-crystallin which is the main protein in the cortex of the lens. It is also believed to be the most stable one [245]. Despite the stable nature, a few of its variants G18V, D26G and G57W are known to cause hereditary cataract [245], [253]–[257]. Therefore, studying the mechanism involved in the aggregation of these proteins is very crucial in fighting the disease. In the past, there have been studies linking the disease to different modifications such as deamidation, methylation disulphide bonds, UV photodamage, mutations and metallization [254], [256], [258]–[263].

Here the author aims to study the morphological evolution of the aggregates formed via UV A and B radiation with time. The fact that the human eye lens is exposed to UV radiations from the sun regularly marks the importance of this study. Although incident UV light is efficiently quenched by the photo-protective molecules present in the cornea. Still, the lens is regularly exposed to 0.116-0.99 mW/cm^{-1} of UVA and 1.2×10^{-4}-4.4×10^{-4} mW/cm^{-1} UVB radiation [245], [264]. Over one's lifetime, this exposure eventually depletes the available photo-protective molecules, increasing the radiation stress on the crystallins. While exact physiological longer-term, low flux measurements are not easily studied, excess UVA or UVB radiation results in tryptophan degradation products such as N-formyl kynurenine and kynurenine, which destabilize their surrounding hydrophobic core [245], [246], [265].

There are a few protein-related hereditary diseases linked to point mutation. These mutations lead to reduced solubility in proteins and consequently, aggregation. Aggregates formed can be either amyloid type, which is the case in the early on-set of Alzheimer diseases [245], [266]. These could also be assembled aggregates from the monomeric unit as is the case in sickle cell anaemia [245], [267]. Therefore, it was crucial to understanding the nature of aggregates formed via mutation and how much it differed if any with UV induced aggregates. Additionally, the mutated γS-crystallin (G18V, D26G and V42M) were irradiated with UV. The last step was to check if any different morphology or increment in the population of the already formed aggregates occur.

Metal ions have been known to cause amyloid type aggregation responsible for Parkinson and Alzheimer via metal-induced conformational changes and metal-catalysed oxidative damage [268]–[270]. Therefore, it was intriguing to investigate the effect of metal

78

addition (Cu^{2+}, Zn^{2+}) to the γS-crystallin protein and compare the morphology of aggregates with those formed with UV irradiation or mutation.

7.2   Sample preparation

UVA and UVB radiation were studied separately to deduce potential differences in the resulting aggregates. UVB is readily absorbed via tryptophan residues whereas UVA is not; however, both wavelength ranges have been demonstrated of oxidizing γ-crystallins. Additionally, native aggregates of cataractous mutants γS-G18V, γS-D26G, and γS-V42M were measured to access the effect of UV-radiation on proteins with reduced stability. Copper and zinc-mediated aggregates were also studied. Elevated levels of copper have been observed in diabetic lenses, and copper has been shown to induce γ-crystallin aggregation via oxidation and disulfide cross-linking. Zinc-mediated aggregation is driven almost exclusively through intermolecular bridging of cysteine side chains and therefore provides an aggregation model in which no structural modifications occur.

All samples were prepared by Kyle W. Roskamp, Department of Chemistry, UC Irvine. The mutants γS-G18V, γS-D26G, and γS-V42M were made using site-directed mutagenesis of the γS-WT construct. All proteins were expressed via high density auto-induction and purification, as previously described in Roskamp *et al.* [245], [271]. Briefly, proteins were removed from the lysate via nickel affinity, N-terminal his-tags were cleaved using TEV protease (produced in-house), re-run over a nickel affinity column, and purified using size exclusion chromatography. Samples were store at 4 ℃ until measurements or further preparation.

The UVA irradiation was performed in the Department of Chemistry, UC Irvine. Therefore, the author only provides a very brief detail for it. Protein solutions at 6 mg/mL (2.5 mL) or 100 mg/mL (1.5 mL) were irradiated with 355 nm light generated using a 10 Hz Nd: YAG laser. The author performed UV B irradiation for the protein samples with an in-house build setup. Aggregation of 6 mg/mL or 100 mg/mL γS-crystallins via 278 nm UVB radiation was accomplished using two 70mW light-emitting diodes (LEUVA66H70HF00, Seoul, Korea) at 5 mm distances (120-degree view angle) yielding a mean power density of 58 mW/cm^2.

To study the effect of metals on γS-crystallins, Protein samples were extensively dialyzed against demetallized 10 mM HEPES buffer and concentrated to 6 mg/ml. 10 equivalents of $CuCl_2$ or $ZnCl_2$ were added to 1 ml samples and allow to incubate at room temperature overnight.

The morphology of the γS-crystallin aggregates formed subject to acidic buffer, UV irradiation, mutation, and metal ion treatment were investigated by transmission electron microscopy (TEM). Negatively stained samples for TEM were prepared on commercial Carbon-coated 400 mesh Copper grids (Plano GmbH, Wetzlar, Germany). The grids were made hydrophilic by glow discharge treatment, whereupon 2 µl of sample solution was applied and allowed to soak for 45 seconds before blotting. The grids were then rinsed twice with 50 µl deionized water, followed by blotting. Negative staining was performed in Dr. Dominik Oberthuer's laboratory. The procedure includes applying 4 µl of a 1 percent Uranyl Acetate solution, followed by immediate blotting. Application of 4 µl of Uranyl acetate was then repeated, this time being allowed to soak for 20 seconds before a final blotting step.

TEM micrographs were then recorded in a JEOL JEM 2100, in bright field mode, with an accelerating voltage setting of 120 kV. To get the size distribution for the aggregates, to each micrograph a bandpass filter was applied manually followed by automatic thresholding using the ImageJ software and finally the whisker plots were prepared in Origin software. Apart from TEM, other methods like Absorbance, Fluorescence, FTIR (Fourier-transform infrared spectroscopy), Mass-Spectroscopy, SDS-PAGE and PEGylation were also performed to study the aggregation behaviour of γS-crystallin. These measurements were performed by Dr. Kyle W. Roskamp, UCI and are described in Roskamp *et al.,* which is an accepted manuscript.

7.3 Aggregates formed via UV A/UV B compared to those by low pH

Work by King *et al.,* on the exceptional fluorescence quenching efficiency of γ-crystallin has strongly evidenced their photoreactive capacity against UVB. The quenching capacity of γ-crystallins due to rapid electron transfer between the tryptophan ring and proximal N-3 backbone carbonyl is disrupted upon tryptophan oxidation [272]–[274]. Mimics of tryptophan oxidation products in γD-crystallin exhibit dramatically reduced structural stability and increased aggregation; however, tryptophan posttranslational modifications (PTMs) represent a fraction of all observed lens crystallin PTMs [275]–[277]. How deamidation, isomerization, oxidation and other accumulated non-enzymatic PTMs lead to light scattering aggregates has remained elusive, in part due to a lack of structural data. Here we have investigated how UVB and UVA irradiation of γS-crystallin leads to protein aggregation. Tryptophan and other aromatic residues do not absorb UVA radiation. Therefore, sufficient UVA (or UVB) radiation may generate reactive oxygen species or damage susceptible amino acids. Characterization of γS-crystallin aggregates from UVB and UVA irradiation, therefore,

provides a method to assess how different UV wavelengths and indirectly the extent of aromatic oxidation, may alter γS-crystallin aggregates.

UVA and UVB treatments were applied to 6 mg/ml and 100 mg/ml samples of γS-WT and measured over 90 minutes, to investigate aggregation from UV irradiation. While no discernible difference was visible between the aggregates from both treatments, UVB exposure induced aggregation more rapidly. In both treatments at 6 mg/ml, sphere-like aggregates between 20-40 nm formed initially. These aggregates grew large and less defined in shape with increasing UV exposure. Although smaller aggregates remain present at all times, see Figure 7.1. Extrapolating from the observed distribution of aggregates which are assumed to represent the various stages of aggregation under UV irradiation, nucleation resulting in small spherical clusters, appear to be the first stage of aggregation. As aggregate size increases, the shape of the aggregates becomes highly diverse. Remarkably, both irradiation treatments at 6 mg/ml and 100 mg/ml did not affect the observed size and distribution of aggregates, see Figure 7.2. Aggregates formed under low pH condition mostly have fibril nature which is not the case with UV induced aggregates. The latter leads to amorphous aggregates. Figure 7.3 illustrates the difference between the two different types of aggregation [245].
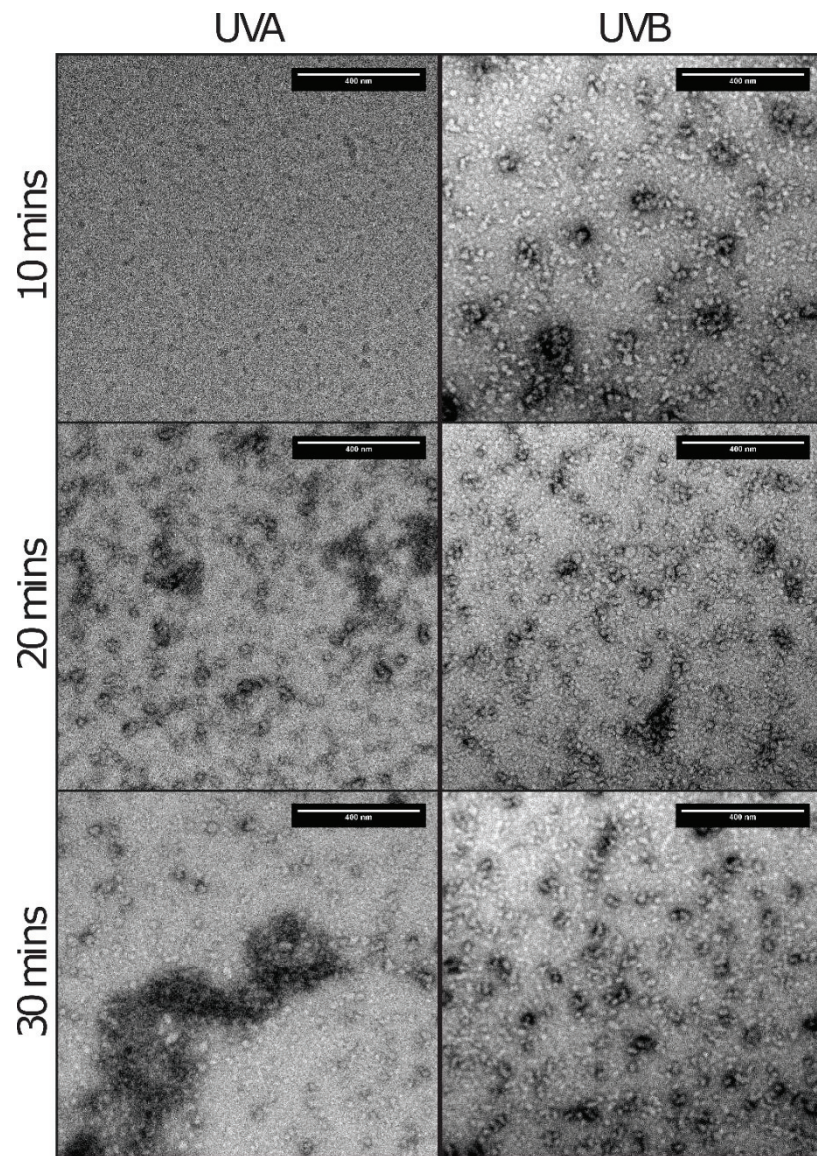
Figure 7.1: γS-WT irradiated using UVA and UVB for 10 min (0.5 KJ/cm^2, 34.8 J/cm^2), 20 min (1.1 KJ/cm^2, 69.6 J/cm^2) and 30 min (1.6 KJ/cm^2, 104.4 J/cm^2). Under both treatments, globular aggregates form and these constituents associate to generate larger aggregates.
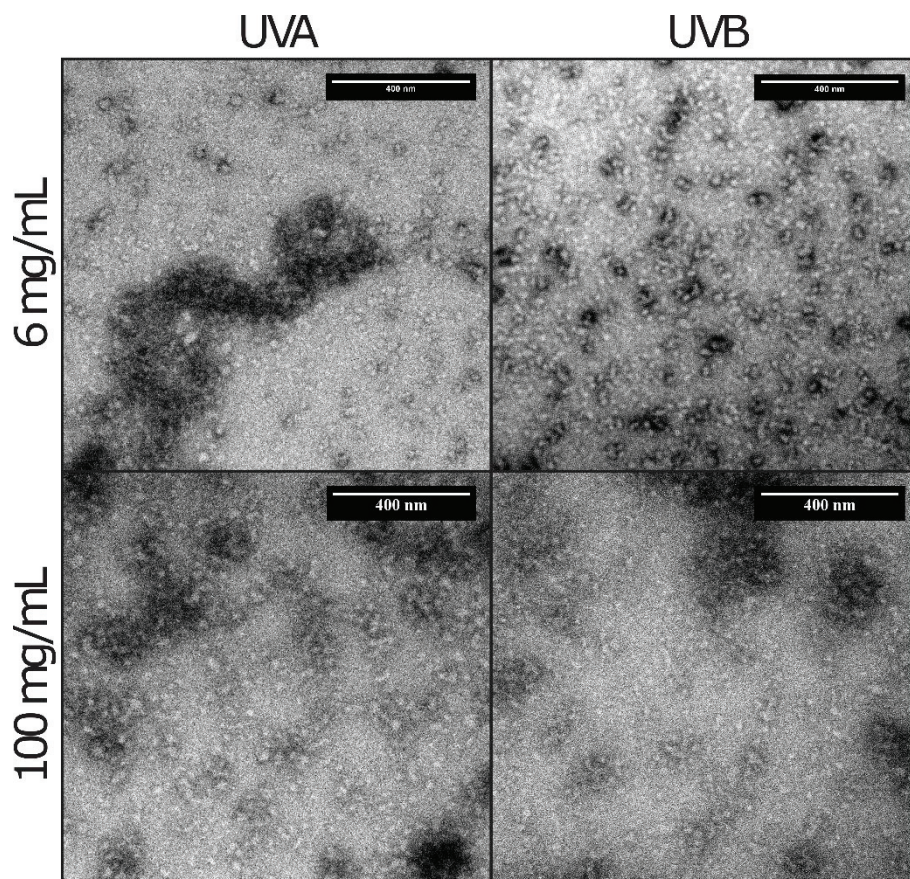
Figure 7.2: Irradiation of γS-WT from UVA (1.6kJ/cm^2) and UVB (104.4 J/cm^2) produces aggregates with similar morphology independent of sample concentration during irradiation.

7.4 Aggregation from mutation compared to UV irradiation

While the accumulation of nonspecific PTM's from UV radiation, reactive oxygen species and other exogenous factors eventually culminate in γ-crystallin aggregation, cataractous mutations provide insight about the minimum change necessary for aggregation. Hydrophobic-hydrophilic core residue conversions (γD-W43R), seemingly innocuous substitutions (γS-S39C, γS-V42M), side-chain removal (γS-D26G, γD-E107A), and charged residue swaps (γC-R48H, γD-R58H) are sufficient for cataract formation.
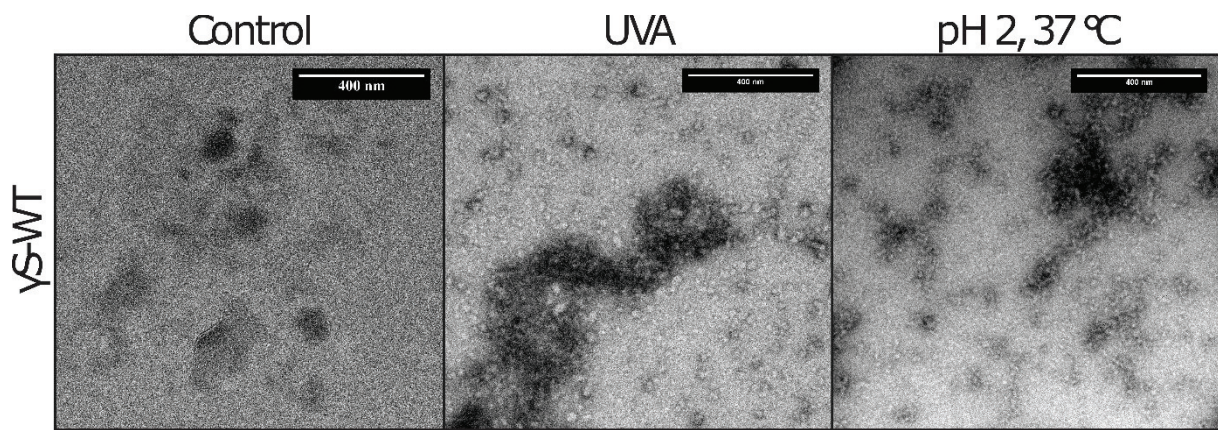
Figure 7.3: Samples of γS-WT without treatment, after UVA irradiation, and after incubation at 37 ∘C at pH 2. UVA aggregates are globular while those prepared at low pH exhibit fibrillar morphology

Cataractous γ-crystallin point mutants are useful references for investigating the effect of site-specific modifications and provide a basis for understanding how PTMs from UV radiation and other exogenous sources may induce cataract. Aggregates of γS-G18V, γS-D26G, and γS-V42M were allowed to form without external provocation (native) and compared to samples irradiated with UVA for 30 minutes, see Figure 7.4. Both mutant and UVA irradiated aggregate morphologies are primarily spherical, with coarse edges that bare no characteristic features. To get the size distribution for the aggregates, to each micrograph, a bandpass as described earlier in this chapter.
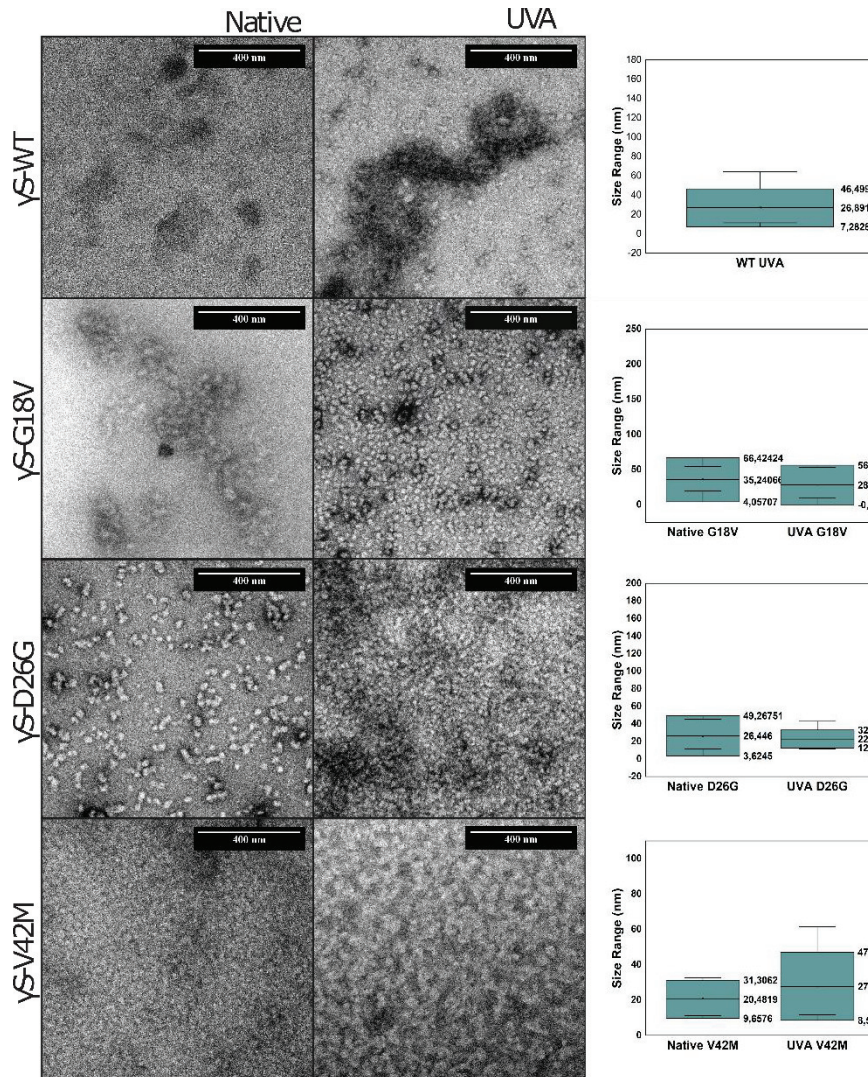
Figure 7.4: Aggregates of resulting from cataractous mutations are comparable in size to those formed via UVA photodamage

The particles were assumed to be roughly circular for calculating the particle diameter, and then box whisker was plotted in Origin software. γS-WT aggregates were only observed following UVA irradiation, with an average aggregate diameter near 26 nm. For γS-D26G, γS-V42M, and γS-G18V, the native sample aggregate diameters were observed at 26, 20, and 35 nm while UVA-irradiated sample diameters were 22, 27, and 28 nm respectively. It is worth noting that the size estimates here may be subjective to the imaged sample areas; however, all samples exhibit homogeneity in aggregate particles sizes, with a primarily 20-40 nm diameter aggregates. Larger aggregates can be readily observed within the measured samples, in which the constituents are particles within these ranges. Although it is not discernible why the aggregates populate this size range, both native and UV-induced aggregates behave similarly

7.5   Aggregates induced by the mixing zinc and copper ions

Exogenous factors such as α-crystallins chaperones and antioxidant metabolites play an important role in buffering the environment of lens fibre cells for γ-crystallins. In addition to calcium homeostasis, the regulation of zinc and copper levels are essential as cofactors for α-crystallins. Elevated levels of these and other metal cations concentrations are observed in lenses of smokers, diabetics, and cataract patients, and have been shown to aggregate γ-crystallins [263], [278], [279]. Excess of zinc ions results in γ-crystallin aggregation through intermolecular bridging, which is reversible via the addition of metal chelating agents [263], [278], [279]. Incubation of copper with γ-crystallins produces similar effects, but also, weakly reduce protein stability and causes PTMs.

Further, the addition of metal chelating agents only partial reverses Cu(II)-mediated aggregation, evidencing other mechanisms of aggregation [263], [278], [279]. Both zinc and copper-mediated aggregation serve as useful references for UV induced aggregation. This comes from the fact that zinc aggregates occur strictly through bridging interactions and copper-induced oxidation of sidechains strongly parallels the high levels of oxidation observed in senile cataract γ-crystallins.

TEM images of γS-WT treated with Cu^{2+} and Zn^{2+}, shown in Figure 7.5, demonstrate similar morphology to γD-WT aggregates previously reported [263]. While clusters of Cu(II) induced particles tend to be smaller than Zn(II) induced ones, the constituents are similarly sized and amorphous in morphology. In comparison to UV-induced aggregates, clusters of Cu(II) and Zn(II) aggregates are observed with more homogenous sizes. This is consistent with the ability of the metal cations to interact with any protein available, leading to similarly-sized aggregate forming concurrently. In contrast, UV-induced damage is likely far more inhomogeneous. The uneven distribution of aggregates most likely leads to nucleation, enabling some clusters to develop early and grow larger, leading to a broader range of aggregate sizes.
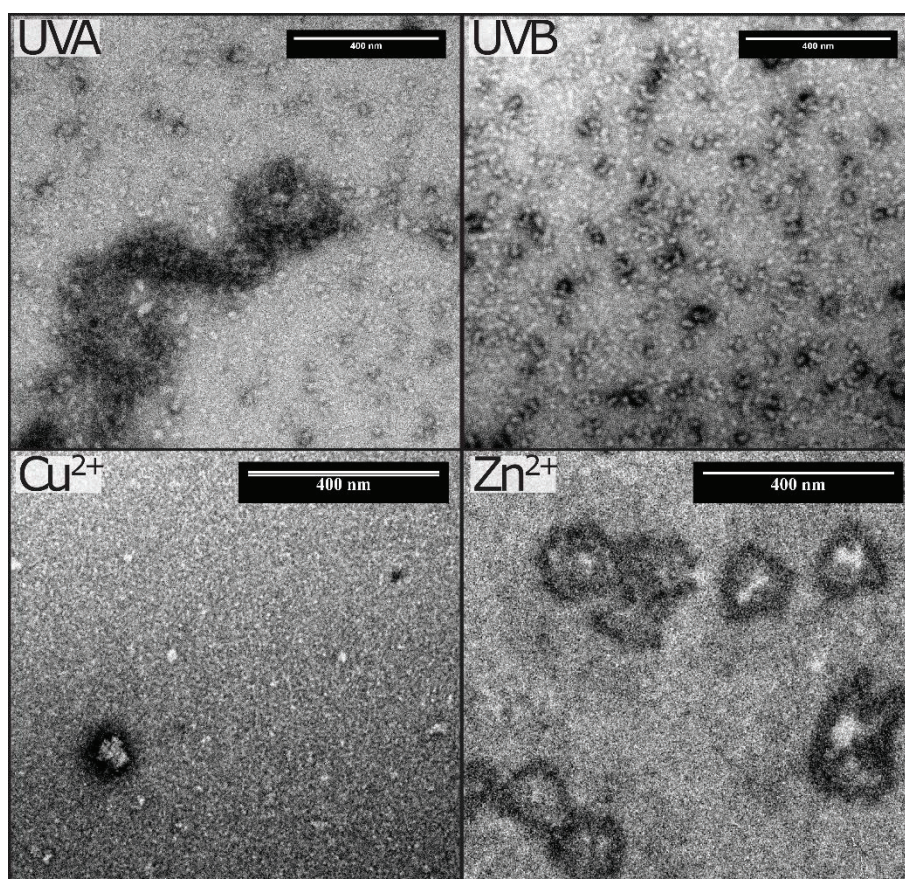
Figure 7.5: Radiation and metal-induced aggregates of γS-WT

7.6   Predicting the possible aggregation mechanism

Comparing the morphology and size of the distribution of the aggregates, it could be inferred that UV radiations have a similar impact as the point mutations because they form similarly sized (20 - 40 nm) primarily spherical aggregates which appear amorphous. While an acidic pH produces fibril type aggregates. The mechanism of UV induced aggregates becomes more apparent when they are compared to homogeneous metal-induced aggregation, consistent with the ability of metal cations to interact with any protein available. In contrast, the UV radiation produces inhomogeneous damage, similar to point mutations. Therefore, explaining the uneven distribution of the aggregates which most likely leads to nucleation enabling some clusters to develop early and grow, thereby giving a broader size range.

8   Conclusion and prospects

This PhD work represents a contribution to the development of liquid cells and their application in TEM to perform real space imaging and diffraction of inorganic, organic and biological specimens in liquid. During this Ph.D., work was done on both development and application fronts. The author was actively involved in the fabrication and characterization of existing liquid cell technology in the group. In addition to this, the author was involved in designing the elliptical multi-window liquid cell for phase-contrast imaging. The most important achievement of the work presented here is the development of the environmental liquid cell technique, which has excellent potential in performing a wide range of real space imaging and diffraction measurements in solution phase. Hereafter, a chapter-wise summary of the work done by the author during this thesis is provided

20 nm thin silicon nitride windows for nanofluidic cells were fabricated, as described in section 3.2. Performing imaging/diffraction with these cells was very challenging as can be seen from the work presented in Appendix 1. The main factor for the poor imaging conditions of these cells was the window bulging, which was characterized and found to be ~ 3 μm, as described in section 4.2. The problem of micron thick specimen due to window deformation was resolved by the development of the environmental liquid cell (ELC) setup, which worked by combing the idea of an environmental cell with the nanofluidic cell technology as presented in chapter 5.

The ELC setup, discussed in section 5.1, is capable of maintaining a stable liquid environment and can perform in-liquid imaging and diffraction of different types of specimens such as metal nanoparticles, polymers or biological macromolecules. Proof of principle measurements conducted on gold nanoparticles, polystyrene beads and ferritin molecules were successful and a controllable liquid thickness as thin as 160 nm was possible, which led to a spatial resolution of 0.8 nm on imaging of gold nanoparticles.

The ELC TEM technique was also utilized to obtain electron scattering data from liquid water at ambient temperature as presented in chapter 6. Minimal multiple scattering was ensured by maintaining a liquid thickness below 200 nm. Scattering data was sufficiently good to enable the O•••H and O•••O bonds to be determined as 1.84 Å and 2.84 Å respectively with a spatial resolution of 0.4 Å. These bond lengths were further utilized to estimate the total number of

hydrogen bonds per water molecule which was found to 3.8, implying a nearly tetrahedral structure.

Neither the standard liquid cell technology nor the ELC TEM was able to capture the aggregation of small protein molecules, human γS-crystallin, as they were exposed to different external stimuli. Negative stain electron microscopy was used to investigate the mechanism and type of aggregation taking place in these proteins, as discussed in chapter 7. The important inference from the measurements is that the UV radiations produces inhomogeneous damage to γS-crystallin, which is similar to the point mutations, and this mechanism is different from acid-induced and metal-invoked aggregation.

Although the ELC system was able to resolve the issues of uncontrolled liquid thickness and bulging, still the background scattering from 20 nm thick silicon nitride was significant, section 6.3. Additionally, this system was based on free-standing large single-window design without any support structure, thereby prone to rupture. To be able to solve all the above-said problems, a new liquid cell has been designed. This comprises of small elliptical multiple windows (minor axis = 5 µm, 10 µm, and 15 µm) inside a large 400×600 µm^2, with 10 nm thin silicon nitride supported by 30 µm thick silicon support structure. The fabrication is in progress, as discussed in section 4.3. This new design, elliptical multi-window liquid cell, will be available for imaging and diffraction applications in a few months.

Outlook

It has been shown that the ELC offers controllable liquid thickness, full viewing area and sub-nm spatial resolution. These features of the ELC can be utilized to perform ensemble averaging on molecules such as ferritin and obtain high-resolution 3-D structures of them in their native state. The environmental liquid cell also resolves issues such as bulging, uncontrolled liquid thickness and difficulty in specimen/reagent exchange. Nonetheless, the technique does not work very well at elevated temperature. At high temperatures (>40°C), the condensation phenomenon of the moist air on the window is slowed down, resulting in drying out of the specimen. A possible solution could be to mount an on-chip heater/cooler in close vicinity to the silicon nitride window, which will only elevate the local temperature and leave minimal effect on the humid air flowing through the holder. The cooler will help in instant cooling down after acquiring the micrographs at a particular temperature.

Sana Azim   Hamburg, 2020

The author has successfully reported the structure of liquid water at room temperature using the ELC TEM technique. Provided that the temperature control in the ELC works as described above, static diffraction on liquid water at different temperatures ranging from 4°C – 90°C can be performed. These measurements will help in estimating the fluctuations in the dense hydrogen-bonded network upon a change in temperature, which in turn would be reflected in the atom-atom pair distribution function. For a deeper understanding of the thermal fluctuations in liquid water, and how it affects the hydrogen bonding network present in it, an optical pump-electron probe measurement is needed. Such an experiment will require a fast sample refreshing rate (above 1 kHz), and an optical pump laser to excite the OH stretching vibrations centred at 3400 cm^{-1} as these vibrations are very sensitive to hydrogen bonds [189]. The existing liquid cell sample transfer arm in the Miller group has provision to include an optical fibre which can be connected to a laser to carry-out *in situ* laser excitation.

The ability to excite specimens *in situ* can be used as a platform for several other measurements where an optical trigger can activate the reaction dynamics, for instance removing the photoprotective layer of caged molecules to stimulate them [280], [281].

The idea of the elliptical multi-window design for phase-contrast imaging holds a lot of potential in unravelling the structure and dynamics of numerous biological macromolecules at very high resolutions. These new generation liquid cells along with a high-speed camera having two orders of magnitude faster readout speed and an ultra-bright electron source for capturing structural dynamics in a single shot, avoiding beam-induced damage, could provide the missing link in the field. The faster camera and the ultra-bright source are being developed in the Miller group [282]–[284].

Appendix

Appendix 1: Measurements performed using 20 nm thin liquid cell, without ELC system

As stated in chapter 4, the bulging of the as-fabricated 20 nm thin liquid cells was significant (3 µm), and therefore it was challenging to perform imaging on organic/biological specimens. This difficulty was realized by the author while studying the interaction mechanism of liposomes and DNA in real-time using these liquid cells. Further details about this are provided henceforth.

Cationic liposomes and DNA (deoxyribonucleic acid) are known to form complexes called lipoplexes, in a process known as lipofection. These lipoplexes find application in gene delivery to cells. Therefore, it is of scientific interest to learn the morphology of the complexes formed and mechanism involved. Different conformations of lipoplexes have been mentioned in the literature, such as the configuration with a short-range lamellar structure composed of flat lipid bilayers and DNA packed between them [285]–[291], or a conformation where the DNA molecules are captured inside a lipid bilayer forming cylindrical complexes which are closely packed on a hexagonal network [287]. Another possible structure is one where the positively charged vesicles confer to the extended DNA molecule, the so-called beads on a string model [292]–[296]. The last conformation predicted is the one where DNA is expected to collapse and attach in the form of a globule into the outer surface of positively charged vesicles [297], [298].

In order to understand the interaction mechanism between liposomes and DNA, a mixture of 9 µl lipofection reagent, which is a 1:1 (w/w) liposome formulation of the cationic lipid N-[1-(2,3dioleyloxy)propyl]-n,n,n-trimethylammonium chloride (DOTMA) and dioleoyl - phosphatidylethanolamine (DOPE) in membrane filtered water and 4 µg DNA was incubated for three hours, drop casted on a no flow liquid cell and imaged in TEM. Liposomes without any DNA were imaged as a control; on the comparison, a clear difference can be observed. Figure 1 shows the in-liquid micrograph. Although the quality of the images in terms of resolution is not ideal, it was possible to take a few snapshots of the larger complexes formed on the edges of the liquid cell window. The liposomes with no DNA do not show any interaction and appear smaller in size (30-50 nm). In the presence of negatively charged DNA, the cationic liposomes interact with the DNA molecules to form beads on a string structure.

These results are not conclusive, and further measurements are required to make any strong claim. Moreover, it was also not possible to capture the complex formation in real-time, the reason being the damage caused due to the electron beam. Therefore, one may observe the interaction *in-situ* by refreshing the liposome sample rapidly during imaging. Although the demonstrated resolution and flow capability of the ELC TEM may allow such measurements, the author has kept this out of the scope of this PhD work.
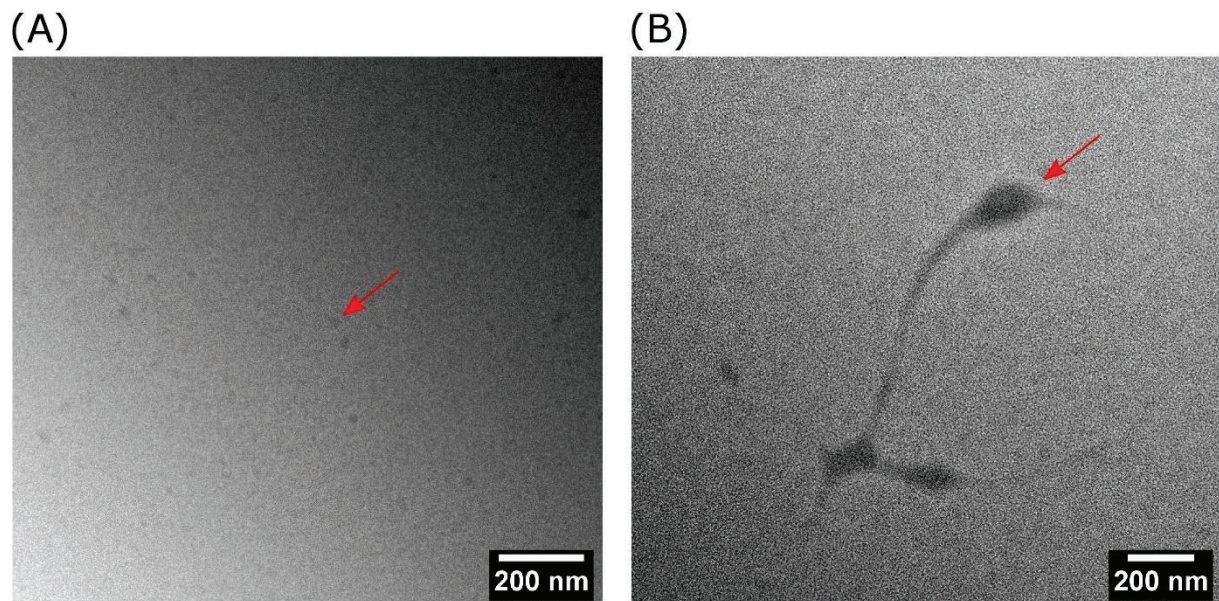
Figure 1: In-liquid TEM micrographs (A) only liposomes, (B) liposomes mixed with 4 µg DNA and incubated for three hours at room temperature.

Sana Azim   Hamburg, 2020

Appendix 2: Imaging performed using ELC TEM to utilize the idea of single-particle ensemble averaging

The author has mentioned in chapter 5 about utilizing ELC TEM for in-liquid single-particle ensemble averaging. Single-particle algorithms are commonly used with cryo-EM to acquire high-resolution three-dimensional structures of beam-sensitive specimens with poor mass-thickness contrast. The same concept can be applied to LPTEM and attain atomic resolution for small biological molecules which is otherwise hard to achieve. The author performed initial measurements on two systems (T7 bacteriophages and gold-labelled antibody) very commonly used in the cryo-EM community. The author hereafter provides the preliminary results obtained.

Bacteriophage T7 is a virus that infects vulnerable bacterial cells. Morphologically, these have an icosahedral head (60 nm) and a short tail. T7 samples were received from a collaborator and were used as received. The ELC sample preparation was done, as described in section 5.2. Briefly, the bottom chip was hydrophilized, and 0.5 µl of the sample was drop cast onto it. Micrographs were recorded; for comparison, the same sample was loaded onto a TEM grid. Figure 2 shows the T7 virus dried on a grid (A) and in a thin layer of liquid in the ELC (B).
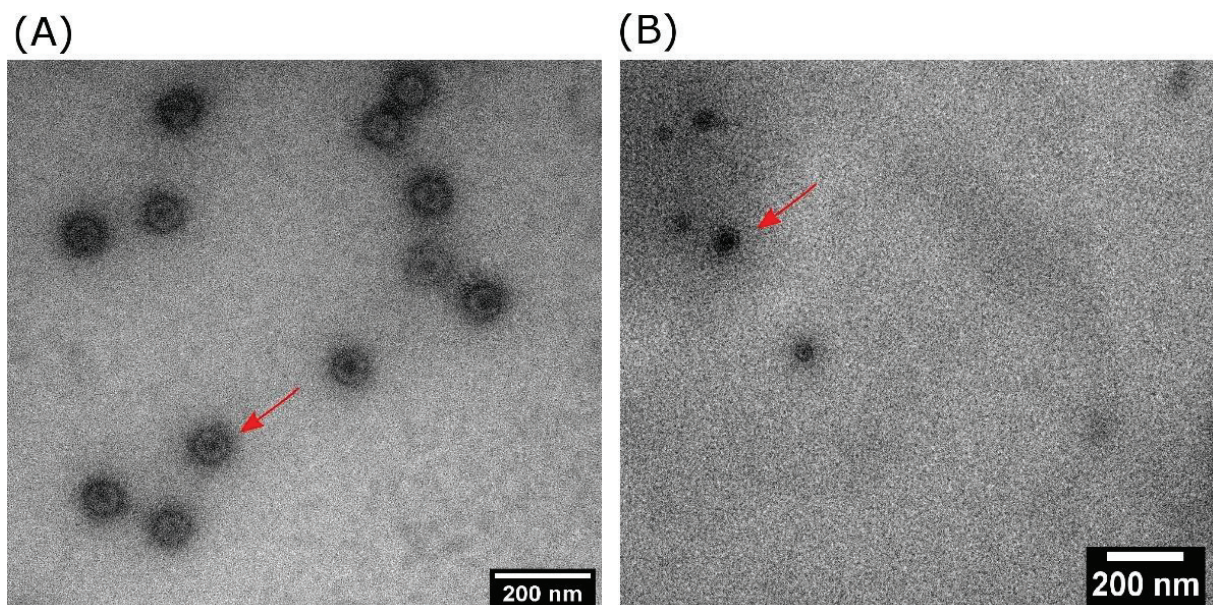
Figure 2: TEM micrographs of bacteriophage T7, (A) on a TEM grid, (B) in a thin layer of liquid inside an ELC.

A single particle algorithm requires a few hundred frames, each with at least 10 particles. Upon exposing the virus to a total electron dose of 1.6 e/$\mathring{A}^2$, substantial damage was observed due to which these could not be used as a model system to obtain high-resolution structures in-liquid.

As the second system gold-labelled antibodies (goat anti-mouse IgG, with 1.4 nm nanogold) procured from Nanoprobes, Yaphank NY was considered. Zhang *et al.* reported a "Y" shape of antibodies with dimensions of 15-18 nm. Most of the antibody particles have three ring-shaped domains with diameters 5.5-7.5 nm, which linked to two F_{ab} domain and one F_c domain [299]. Gold labelled antibody samples were used as received, and an ELC sample preparation was done as previously described. The negatively stained sample was also prepared as a reference by using 2% Sodium silicotungstate. Negative stained (A) and in-liquid micrographs (B) were recorded at a total electron dose of 62 e/$\mathring{A}^2$ and 5.6 e/$\mathring{A}^{2,}$ respectively (figure 8.4).

Sana Azim   Hamburg, 2020
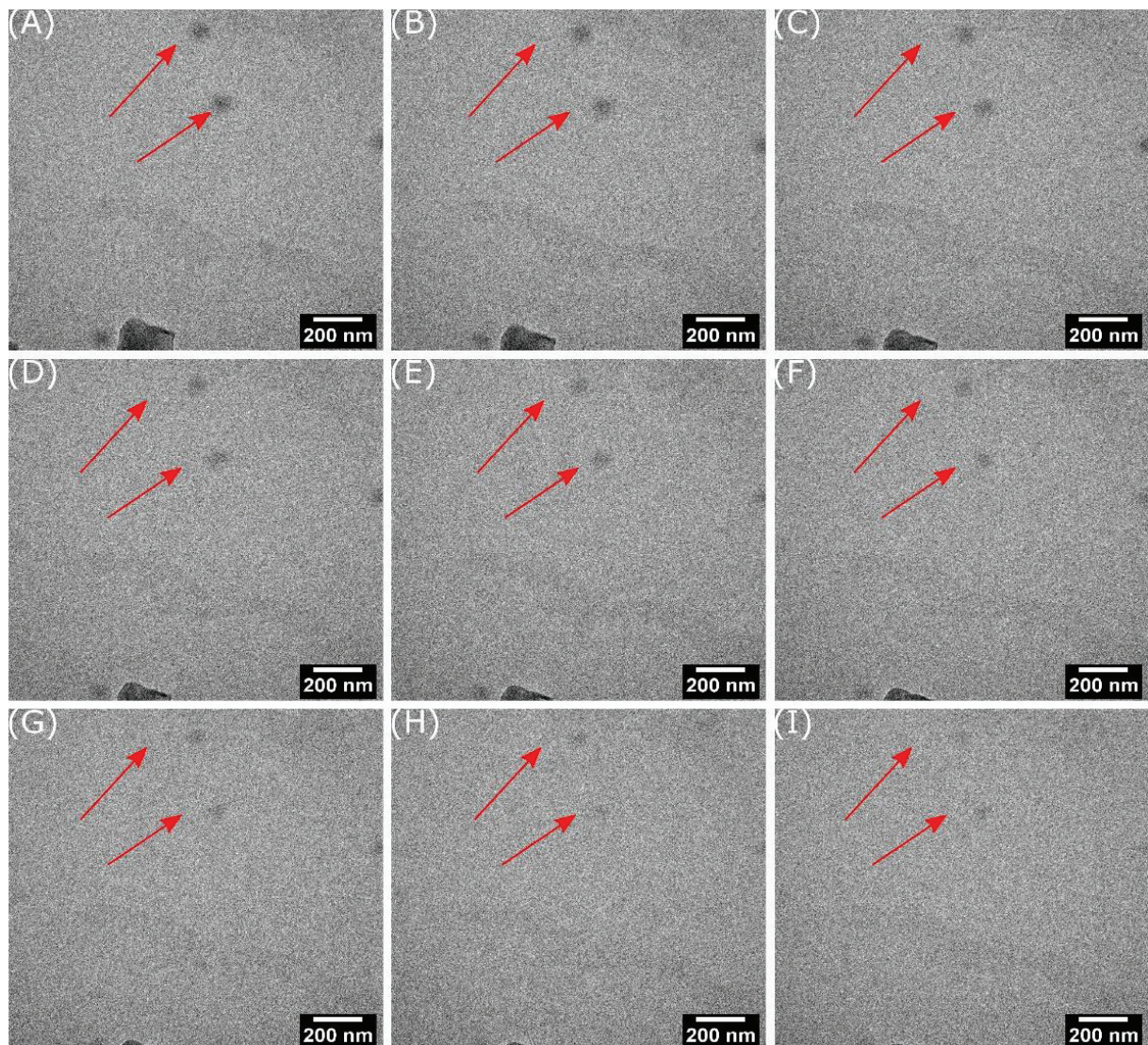
Figure 2: In-liquid TEM micrographs showing the degradation of the T7 virus as the cumulative electron dose increase from 0.16 e/Å^2 (A) to 1.6 e/Å^2 (I).

Because of reduced contrast and small size of the antibodies, the actual structure of them was not visible in the in-liquid micrographs. Still, the nanogold which acted as a marker displayed "Y" shape indicating the presence and orientation of the antibodies. A dataset of a few hundred frames was successfully collected, but the analysis here is challenging because of poor contrast from the particles.

(A)   (B)
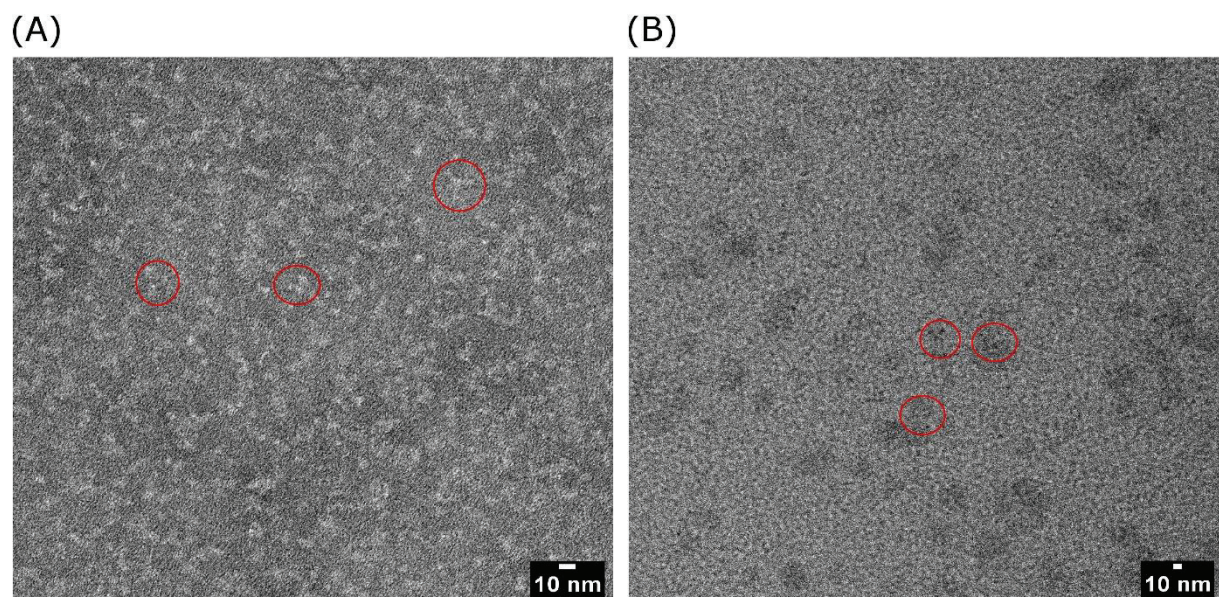
Figure 3: Micrographs showing gold-labelled antibodies, (A) negative stained, (B) in ELC with a thin layer of liquid. In the stained micrograph, the particles are densely packed and difficult to separate individual ones. The particles marked with red circles have a roughly Y-shaped structure and size in the range 18 nm. The in-liquid micrograph fails to show the actual antibody, but the nanogold particles can be observed with a somewhat "Y" shape structure with size in the range 15-18 nm.

Contribution of the author

Scientific publications

- Submitted - Sana Azim, Lindsey Bultema *et al.* "The environmental liquid cell technique for improved electron microscopic imaging of soft matter in solution"

- In preparation - Michiel de Kock, Sana Azim *et al.* "Determining the radial distribution function of water using electron scattering: A key to solution-phase chemistry"

- Kyle W. Roskamp, Sana Azim, Günther Kassier, Brenna Norton-Baker, Marc A. Sprague-Piercy, R. J. Dwyane Miller, and Rachel W. Martin, "Human γS-Crystallin– Copper Binding Helps Buffer against Aggregation Caused by Oxidative Damage", Biochemistry Article ASAP DOI: 10.1021/acs.biochem.0c00293

Conference proceedings

- D. Venegas-Rojas, S. Keskin, S. Azim, S. Manz, R. J. D. Miller and H. K. Trieu, "Multi-window Transmission Electron Microscopy liquid cell to improve imaging performance," MikroSystemTechnik 2017; Congress, Munich, Germany, 2017, pp. 1-4.

- S. Azim, G. Kassier , S. Keskin , S. Manz , R. Bücker , A. Casandruc , E. Schulz , K. Roskamp R. W. Martin, D. V. Rojas , H. K. Trieu , R. J. D. Miller, "Capturing the aggregation dynamics of ϒS Crystallin with in-liquid electron microscopy", "Microscopy Conference 2017; Lausanne, Switzerland, pp. 560-562.

Own poster/oral presentation

- S. Azim, G. Kassier, R. Bucker, E. Schulz and R.J.D. Miller, "The environmental liquid cell technique for imaging biological structures," presented at Microscience Microscopy Congress, Manchester Central, UK, July 2019

- S. Azim, L. Bultema, M. de Kock, E. Schulz, R. Buecker, S. Keskin, N. de Jonge, G. Kassier and R.J.D. Miller, "The Environmental liquid cell technique for TEM,"

Sana Azim   Hamburg, 2020

presented at 1st Gordon Research Conference on Liquid Phase Electron Microscopy,

January 2020, Lucca (Barga), Italy

9 References

[1]   S. J. Lai-Fook and M. R. Kaplowitz, "Pleural space thickness in situ by light microscopy in five mammalian species," *J. Appl. Physiol.*, vol. 59, no. 2, pp. 603–610, Aug. 1985.

[2]   T. Raap, "In situ Hybridization in Light Microscopy," *J. Microsc.*, vol. 210, no. 2, pp. 187–188, May 2003.

[3]   J. Steiger, D. Kramer, and R. Mönig, "Mechanisms of dendritic growth investigated by in situ light microscopy during electrodeposition and dissolution of lithium," *J. Power Sources*, vol. 261, pp. 112–119, 2014.

[4]   K. Stanislav, "Light Microscopy in Biological Research," *Biophys. J.*, vol. 88, no. 6, p. 3741, Jun. 2005.

[5]   P. Dedecker, J. Hofkens, and J. Hotta, "Diffraction-unlimited optical microscopy," *Mater. Today*, vol. 11, pp. 12–21, 2008.

[6]   J. Vangindertael, R. Camacho, W. Sempels, H. Mizuno, P. Dedecker, and K. P. F. Janssen, "An introduction to optical super-resolution microscopy for the adventurous biologist," *Methods Appl. Fluoresc.*, vol. 6, no. 2, p. 22003, 2018.

[7]   S. W. Hell and J. Wichmann, "Breaking the diffraction resolution limit by stimulated emission: stimulated-emission-depletion fluorescence microscopy," *Opt. Lett.*, vol. 19, no. 11, pp. 780–782, 1994.

[8]   M. Bates, S. A. Jones, and X. Zhuang, "Stochastic Optical Reconstruction Microscopy (STORM): A Method for Superresolution Fluorescence Imaging," *Cold Spring Harb. Protoc.* , vol. 2013, no. 6, p. pdb.top075143, Jun. 2013.

[9]   J. Hanne *et al.*, "STED nanoscopy with fluorescent quantum dots," *Nat. Commun.*, vol. 6, May 2015.

[10]   K. I. Willig, S. O. Rizzoli, V. Westphal, R. Jahn, and S. W. Hell, "STED microscopy reveals that synaptotagmin remains clustered after synaptic vesicle exocytosis," *Nature*, vol. 440, no. 7086, pp. 935–939, Apr. 2006.

[11]   B. Huang, W. Wang, M. Bates, and X. Zhuang, "Three-Dimensional Super-Resolution Imaging by Stochastic Optical Reconstruction Microscopy," *Science (80-.).*, vol. 319,

Sana Azim   Hamburg, 2020

no. 5864, pp. 810–813, Feb. 2008.

[12] W. Friedrich, P. Knipping, and M. Laue, "Interferenzerscheinungen bei Röntgenstrahlen," *Ann. Phys.*, vol. 346, no. 10, pp. 971–988, Jan. 1913.

[13] L. Martiradonna, "A photograph of crystal order," *Nature*, vol. 511, no. S7509, pp. 7–7, Aug. 2014.

[14] D. W. Green, V. M. Ingram, M. F. Perutz, and W. L. Bragg, "The structure of haemoglobin - IV. Sign determination by the isomorphous replacement method," *Proc. R. Soc. London. Ser. A. Math. Phys. Sci.*, vol. 225, no. 1162, pp. 287–307, Sep. 1954.

[15] M. Perutz, M. Rossmann, A. F. Cullis, H. Muirhead, G. Will, and A. C. T. North, "Structure of hoemoglobin," *Nature*, vol. 185, pp. 416–422, 1960.

[16] J. C. KENDREW *et al.*, "Structure of Myoglobin: A Three-Dimensional Fourier Synthesis at 2 Å. Resolution," *Nature*, vol. 185, no. 4711, pp. 422–427, 1960.

[17] J. D. WATSON and F. H. C. CRICK, "Molecular Structure of Nucleic Acids: A Structure for Deoxyribose Nucleic Acid," *Nature*, vol. 171, no. 4356, pp. 737–738, 1953.

[18] V. Šrajer and M. Schmidt, "Watching proteins function with time-resolved x-ray crystallography," *J. Phys. D. Appl. Phys.*, vol. 50, no. 37, p. 373001, 2017.

[19] H. Cao and J. Skolnick, "Time-resolved x-ray crystallography capture of a slow reaction tetrahydrofolate intermediate," *Struct. Dyn.*, vol. 6, no. 2, p. 24701, Mar. 2019.

[20] P. Mehrabi *et al.*, "Liquid application method for time-resolved analyses by serial synchrotron crystallography," *Nat. Methods*, vol. 16, no. 10, pp. 979–982, 2019.

[21] R. H. Von Dreele, R. B., Stephens, P. W., Smith, G. D., & Blessing, "The First Protein Crystal Structure Determined From High-Resolution X-ray Powder Diffraction Data: A Variant of T3R3 Human Insulin-Zinc Complex Produced by Grinding," *Acta Crystallogr. D. Biol. Crystallogr.*, vol. 56, pp. 1549–1553, 2000.

[22] H. D. T. Mertens and D. I. Svergun, "Structural characterization of proteins and complexes using small-angle X-ray solution scattering," *J. Struct. Biol.*, vol. 172, no. 1, pp. 128–141, 2010.

[23] W. Wan, J. Sun, J. Su, S. Hovmöller, and X. Zou, "Three-dimensional rotation electron

Sana Azim   Hamburg, 2020

diffraction: software {\it RED} for automated data collection and data processing," *J. Appl. Crystallogr.*, vol. 46, no. 6, pp. 1863–1873, Dec. 2013.

[24] A. A. Ischenko and S. A. Aseyev, "Chapter Three - Ultrafast Electron Crystallography and Nanocrystallography," in *Time-Resolved Electron Diffraction*, vol. 184, A. A. Ischenko and S. A. B. T.-A. in I. and E. P. Aseyev, Eds. Elsevier, 2014, pp. 101–143.

[25] S. Smeets, X. Zou, and W. Wan, "Serial electron crystallography for structure determination and phase analysis of nanocrystalline materials," *J. Appl. Crystallogr.*, vol. 51, no. 5, pp. 1262–1273, Oct. 2018.

[26] M. Gemmi *et al.*, "3D Electron Diffraction: The Nanocrystallography Revolution," *ACS Cent. Sci.*, vol. 5, no. 8, pp. 1315–1329, Aug. 2019.

[27] R. Bücker *et al.*, "Serial protein crystallography in an electron microscope," *Nat. Commun.*, vol. 11, no. 1, Dec. 2020.

[28] B. J. Siwick, J. R. Dwyer, R. E. Jordan, and R. J. D. Miller, "An Atomic-Level View of Melting Using Femtosecond Electron Diffraction," *Science (80-.).*, vol. 302, no. 5649, pp. 1382–1385, 2003.

[29] R. J. D. Miller, "Mapping Atomic Motions with Ultrabright Electrons: The Chemists' Gedanken Experiment Enters the Lab Frame," *Annu. Rev. Phys. Chem.*, vol. 65, no. 1, pp. 583–604, 2014.

[30] T. Ishikawa *et al.*, "Direct observation of collective modes coupled to molecular orbital–driven charge transfer," *Science (80-.).*, vol. 350, no. 6267, pp. 1501 LP – 1505, Dec. 2015.

[31] N. Grigorieff and S. C. Harrison, "Near-atomic resolution reconstructions of icosahedral viruses from electron cryo-microscopy," *Current Opinion in Structural Biology*, vol. 21, no. 2. pp. 265–273, 2011.

[32] R. A. Crowther, "From envelopes to atoms: The remarkable progress of biological electron microscopy," in *Advances in Protein Chemistry and Structural Biology*, vol. 81, no. C, Academic Press, 2010, pp. 1–32.

[33] G. Jensen, Ed., *Cryo-EM Part A: Sample Preparation and Data Collection*. Academic, San Diego, 2010.

Sana Azim   Hamburg, 2020

[34] G. Jensen, Ed., *Cryo-EM Part B: 3-D reconstruction.* Academic, San Diego, 2010.

[35] J. Frank, *Three-Dimensional Electron Microscopy of Macromolecular Assemblies*. Oxford University Press, New York, 2006.

[36] M. Adrian, J. Dubochet, J. Lepault, and A. W. McDowall, "Cryo-electron microscopy of viruses," *Nature*, vol. 308, no. 5954, pp. 32–36, 1984.

[37] W. F. Tivol, A. Briegel, and G. J. Jensen, "An Improved Cryogen for Plunge Freezing," *Microsc. Microanal.*, vol. 14, no. 5, pp. 375–379, 2008.

[38] M. J. Dobro, L. A. Melanson, G. J. Jensen, and A. W. McDowall, "Chapter Three - Plunge Freezing for Electron Cryomicroscopy," in *Cryo-EM Part A Sample Preparation and Data Collection*, vol. 481, G. J. B. T.-M. in E. Jensen, Ed. Academic Press, 2010, pp. 63–82.

[39] Y. Cheng, N. Grigorieff, P. A. Penczek, and T. Walz, "A primer to single-particle cryo-electron microscopy," *Cell*, vol. 161, no. 3, pp. 438–449, Apr. 2015.

[40] G. W. Stewart, "Theory of x-ray diffraction in liquids," *Phys. Rev.*, vol. 32, no. 4, pp. 558–563, 1928.

[41] C. V RAMAN and C. M. SOGANI, "X-ray Diffraction in Liquids," *Nature*, vol. 119, no. 2999, p. 601, 1927.

[42] K. Moffat, "Time-Resolved Macromolecular Crystallography," *Annu. Rev. Biophys. Biophys. Chem.*, vol. 18, no. 1, pp. 309–332, Jun. 1989.

[43] R. Neutze and K. Moffat, "Time-resolved structural studies at synchrotrons and X-ray free electron lasers: opportunities and challenges," *Curr. Opin. Struct. Biol.*, vol. 22, no. 5, pp. 651–659, 2012.

[44] E. C. Schulz *et al.*, "The hit-and-return system enables efficient time-resolved serial synchrotron crystallography," *Nat. Methods*, vol. 15, no. 11, pp. 901–904, 2018.

[45] Marton L., "La microscopie electronique des objets biologiques," *Acad. R. Belg. Bull. Cl. Sci.*, vol. 20, pp. 439–446, 1934.

[46] I. M. Abrams and J. W. McBain, "A Closed Cell for Electron Microscopy," *J. Appl. Phys.*, vol. 15, no. 8, pp. 607–609, Aug. 1944.

Sana Azim   Hamburg, 2020

[47]   D. L. Dupouy G, Perrier F, "Microscopie électronique—l'observation des objets en milieu gazeux—application à l'étude de la contamination dans le microscope électronique.," *C. R.*, vol. 254, pp. 3786–91, 1962.

[48]   J. A. Swift and A. C. Brown, "An environmental cell for the examination of wet biological specimens at atmospheric pressure by transmission scanning electron microscopy," *J. Phys. E.*, vol. 3, no. 11, pp. 924–926, 1970.

[49]   Allinson DL., "Environmental cell for use in a high voltage electron microscope," in *In Proc. 7th Int. Congr. Electron Microsc.*, 1970, vol. 1, pp. 169–70.

[50]   F. K. Fukami A, Etoh T, Ishihara N, Katoh M, "Pressurized specimen chamber for electron microscope," in *In Proc. 7th Int. Congr. Electron Microsc.*, 1970, pp. 171–72.

[51]   E. F. Fullam, "A Closed Wet Cell for the Electron Microscope," *Rev. Sci. Instrum.*, vol. 43, no. 2, pp. 245–247, Feb. 1972.

[52]   E. P. Butler, "In situ experiments in the transmission electron microscope," *Reports Prog. Phys.*, vol. 42, no. 5, pp. 833–895, 1979.

[53]   H.-G. Liao and H. Zheng, "Liquid Cell Transmission Electron Microscopy," *Annu. Rev. Phys. Chem.*, vol. 67, no. 1, pp. 719–747, May 2016.

[54]   M. J. Williamson, R. M. Tromp, P. M. Vereecken, R. Hull, and F. M. Ross, "Dynamic microscopy of nanoscale cluster growth at the solid-liquid interface," *Nature Materials*, vol. 2, no. 8. European Association for Cardio-Thoracic Surgery, pp. 532–536, 2003.

[55]   N. de Jonge, D. B. Peckys, G. J. Kremers, and D. W. Piston, "Electron microscopy of whole cells in liquid with nanometer resolution," *Proc. Natl. Acad. Sci.*, vol. 106, no. 7, pp. 2159 LP – 2164, Feb. 2009.

[56]   E. A. Ring and N. de Jonge, "Microfluidic System for Transmission Electron Microscopy," *Microsc. Microanal.*, vol. 16, no. 5, pp. 622–629, 2010.

[57]   Mueller. C., Harb. M., Dwyer. J. R., and Miller. R. J. D., "Nanofluidic Cells with Controlled Pathlength and Liquid Flow for Rapid, High-Resolution In Situ Imaging with Electrons," *J. Phys. Chem. Lett.*, vol. 4, no. 14, pp. 2339–2347, Jul. 2013.

[58]   J. M. Yuk *et al.*, "High-Resolution EM of Colloidal Nanocrystal Growth Using Graphene Liquid Cells," *Science (80-.).*, vol. 336, no. 6077, pp. 61 LP – 64, Apr. 2012.

Sana Azim   Hamburg, 2020

[59] M. Textor and N. de Jonge, "Strategies for Preparing Graphene Liquid Cells for Transmission Electron Microscopy," *Nano Lett.*, vol. 18, no. 6, pp. 3313–3321, Jun. 2018.

[60] H. L. Xin and H. Zheng, "In Situ Observation of Oscillatory Growth of Bismuth Nanoparticles," *Nano Lett.*, vol. 12, no. 3, pp. 1470–1474, Mar. 2012.

[61] K.-Y. Niu, J. Park, H. Zheng, and A. P. Alivisatos, "Revealing Bismuth Oxide Hollow Nanoparticle Formation by the Kirkendall Effect," *Nano Lett.*, vol. 13, no. 11, pp. 5715–5719, Nov. 2013.

[62] K. Tai, Y. Liu, and S. J. Dillon, "In situ cryogenic transmission electron microscopy for characterizing the evolution of solidifying water ice in colloidal systems," *Microsc. Microanal.*, vol. 20, no. 2, pp. 330–337, 2014.

[63] D. B. Peckys, G. M. Veith, D. C. Joy, and N. de Jonge, "Nanoscale imaging of whole cells using a liquid enclosure and a scanning transmission electron microscope," *PLoS One*, vol. 4, no. 12, 2009.

[64] Besztejan S. *et al.*, "Visualization of Cellular Components in a Mammalian Cell with Liquid-Cell Transmission Electron Microscopy," *Microsc. Microanal.*, vol. 23, no. 1, pp. 46–55, 2017.

[65] S. M. Rehn and M. R. Jones, "New Strategies for Probing Energy Systems with In Situ Liquid-Phase Transmission Electron Microscopy," *ACS Energy Lett.*, vol. 3, pp. 1269–1278, 2018.

[66] F. M. Ross, "Opportunities and challenges in liquid cell electron microscopy," *Science (80-.).*, vol. 350, no. 6267, pp. aaa9886–aaa9886, 2015.

[67] H. G. Liao and H. Zheng, "Liquid cell transmission electron microscopy study of platinum iron nanocrystal growth and shape evolution," *J. Am. Chem. Soc.*, 2013.

[68] H. Zheng, S. A. Claridge, A. M. Minor, A. P. Alivisatos, and U. Dahmen, "Nanocrystal Diffusion in a Liquid Thin Film Observed by in Situ Transmission Electron Microscopy," *Nano Lett.*, vol. 9, no. 6, pp. 2460–2465, Jun. 2009.

[69] H. Zheng, R. K. Smith, Y. Jun, C. Kisielowski, U. Dahmen, and A. P. Alivisatos, "Observation of Single Colloidal Platinum Nanocrystal Growth Trajectories," *Science*

Sana Azim   Hamburg, 2020

(80-.)., vol. 324, no. 5932, pp. 1309 LP – 1312, Jun. 2009.

[70] J. E. Evans, K. L. Jungjohann, N. D. Browning, and I. Arslan, "Controlled Growth of Nanoparticles from Solution with In Situ Liquid Transmission Electron Microscopy," *Nano Lett.*, vol. 11, no. 7, pp. 2809–2813, Jul. 2011.

[71] H.-G. Liao, L. Cui, S. Whitelam, and H. Zheng, "Real-Time Imaging of Pt<sub>3</sub>Fe Nanorod Growth in Solution," *Science (80-.).*, vol. 336, no. 6084, pp. 1011 LP – 1014, May 2012.

[72] H.-G. Liao and H. Zheng, "Liquid Cell Transmission Electron Microscopy," *Annu. Rev. Phys. Chem.*, 2016.

[73] Chen. Q. *et al.*, "3D motion of DNA-Au nanoconjugates in graphene liquid cell electron microscopy," *Nano Lett.*, vol. 13, no. 9, pp. 4556–4561, Sep. 2013.

[74] S. Keskin *et al.*, "Visualization of Multimerization and Self-Assembly of DNA-Functionalized Gold Nanoparticles Using In-Liquid Transmission Electron Microscopy," *J. Phys. Chem. Lett.*, vol. 6, no. 22, pp. 4487–4492, 2015.

[75] J. Park, H. Zheng, W. C. Lee, P. L. Geissler, E. Rabani, and A. P. Alivisatos, "Direct Observation of Nanoparticle Superlattice Formation by Using Liquid Cell Transmission Electron Microscopy," *ACS Nano*, vol. 6, no. 3, pp. 2078–2085, Mar. 2012.

[76] Y. Liu, X. M. Lin, Y. Sun, and T. Rajh, "In situ visualization of self-assembly of charged gold nanoparticles," *J. Am. Chem. Soc.*, vol. 135, no. 10, pp. 3764–3767, Mar. 2013.

[77] E. R. White *et al.*, "In Situ Transmission Electron Microscopy of Lead Dendrites and Lead Ions in Aqueous Solution," *ACS Nano*, vol. 6, no. 7, pp. 6308–6317, Jul. 2012.

[78] X. Chen, K. W. Noh, J. G. Wen, and S. J. Dillon, "In situ electrochemical wet cell transmission electron microscopy characterization of solid–liquid interactions between Ni and aqueous NiCl2," *Acta Mater.*, vol. 60, no. 1, pp. 192–198, 2012.

[79] M. Gu *et al.*, "Demonstration of an Electrochemical Liquid Cell for Operando Transmission Electron Microscopy Observation of the Lithiation/Delithiation Behavior of Si Nanowire Battery Anodes," *Nano Lett.*, vol. 13, no. 12, pp. 6106–6112, Dec. 2013.

[80] M. E. Holtz *et al.*, "Nanoscale Imaging of Lithium Ion Distribution During In Situ Operation of Battery Electrode and Electrolyte," *Nano Lett.*, vol. 14, no. 3, pp. 1453–

Sana Azim   Hamburg, 2020

1459, Mar. 2014.

[81] T.-W. Huang *et al.*, "Self-aligned wet-cell for hydrated microbiology observation in TEM," *Lab Chip*, vol. 12, no. 2, pp. 340–347, 2012.

[82] U. M. Mirsaidov, H. Zheng, Y. Casana, and P. Matsudaira, "Imaging protein structure in water at 2.7 nm resolution by transmission electron microscopy," *Biophys. J.*, vol. 102, no. 4, 2012.

[83] A. Cameron Varano, A. Rahimi, M. J. Dukes, S. Poelzing, S. M. McDonald, and D. F. Kelly, "Visualizing virus particle mobility in liquid at the nanoscale," *Chem. Commun.*, vol. 51, no. 90, pp. 16176–16179, 2015.

[84] J. J. Vlassak and W. D. Nix, "A new bulge test technique for the determination of Young's modulus and Poisson's ratio of thin films," *J. Mater. Res.*, vol. 7, pp. 3242–3249, 1992.

[85] J. M. Cowley, P. Goodman, B. K. Vainshtein, B. B. Zvyagin, and D. L. Dorset, "2.5. Electron diffraction and electron microscopy in structure determination," 2006.

[86] L. A. Bendersky and F. W. Gayle, "Electron diffraction using transmission electron microscopy," *J. Res. Natl. Inst. Stand. Technol.*, 2001.

[87] G. Sciaini and R. J. D. Miller, "Femtosecond electron diffraction: Heralding the era of atomically resolved dynamics," *Reports on Progress in Physics*, vol. 74, no. 9. Sep-2011.

[88] S. Tavernier, *Experimental Techniques in Nuclear and Particle Physics*. Springer, Berlin, Heidelberg, 2010.

[89] Jonge N. D., Houben L., Dunin-Borkowski R. E., and Ross F. M., "Resolution and aberration correction in liquid cell transmission electron microscopy, Nature Reviews Materials, 4, 2019," *Nature Reviews Materials*. 2019.

[90] E. Bauer, "Low energy electron microscopy," *Reports on Progress in Physics*, vol. 57, no. 9. pp. 895–938, 01-Sep-1994.

[91] R. F. Egerton, *Physical Principles of Electron Microscopy: An Introduction to TEM, SEM, and AEM*. Springer Science+Business Media, Inc. , 2005.

[92] D. P. Divincenzo, "Interaction of X-rays , Neutrons and Electrons with Matter," vol. 33,

2012.

[93] D. B. Williams and C. B. Carter, *Transmission electron microscopy : a textbook for materials science*. Springer Science+Business Media LLC, 2009.

[94] Peter W. Hawkes John C .H. Spence, "Science of microscopy," *Mater. Today*, vol. 9, no. 7–8, p. 52, 2006.

[95] M. Knoll and E. Z. Ruska, "Das Elektronenmikroskop," *Zeitschrift für Phys.*, vol. 78, no. 5–6, pp. 318–339, 1932.

[96] Relnhold Ruedenberg, "Anordnung zum vergroesserten Abbilden von Gegenstaenden mittels Elektronenstrahlen," DE906737 (C) 1954-03-18, 1931.

[97] Reimer. L and Kohl. H, *Transmission Electron Microscopy*. Springer Science + Business Media, LLC, 2008.

[98] A. Merk *et al.*, "Breaking Cryo-EM Resolution Barriers to Facilitate Drug Discovery," *Cell*, vol. 165, no. 7, pp. 1698–1707, 2016.

[99] X. Yu *et al.*, "Cryo-EM structure of human adenovirus D26 reveals the conservation of structural organization among human adenoviruses," *Sci. Adv.*, vol. 3, no. 5, pp. 1–13, 2017.

[100] X. Agirrezabala *et al.*, "Ribosome rearrangements at the onset of translational bypassing," *Sci. Adv.*, vol. 3, no. 6, pp. 1–9, 2017.

[101] P. Ercius *et al.*, "In-situ Observations of Pt Nanoparticle Growth at Atomic Resolution Using Graphene Liquid Cells and Cc Correction," *Microsc. Microanal.*, vol. 18, no. S2, pp. 1096–1097, 2012.

[102] N. De Jonge, D. B. Peckys, G. J. Kremers, and D. W. Piston, "Electron microscopy of whole cells in liquid with nanometer resolution," *Proc. Natl. Acad. Sci. U. S. A.*, vol. 106, no. 7, pp. 2159–2164, 2009.

[103] Yuk. J .M. *et al.*, "High-Resolution EM of Colloidal Nanocrystal Growth Using Graphene Liquid Cells," *Science (80-.).*, vol. 336, no. 6077, pp. 61–64, Apr. 2012.

[104] H. G. Liao, K. Niu, and H. Zheng, "Observation of growth of metal nanoparticles," *Chem. Commun.*, vol. 49, no. 100, pp. 11720–11727, Nov. 2013.

Sana Azim   Hamburg, 2020

[105] Y. Cheng, "Single-Particle Cryo-EM at Crystallographic Resolution," *Cell*, vol. 161, no. 3, pp. 450–457, Apr. 2015.

[106] B. J. Bradbury, S., Joy, D. C., Ford, "Transmission electron microscope," *Encyclopædia Britannica*. Encyclopædia Britannica, inc., 2019.

[107] B. Hafner, "Introductory Transmission Electron Microscopy Primer," *EM*, no. October, pp. 1–31, 2011.

[108] J. M. Zuo and J. C. H. Spence, *Advanced Transmission Electron Microscopy:Imaging and Diffraction in Nanoscience*. Springer-Verlag New York, 2017.

[109] D. J. Smith, "Ultimate resolution in the electron microscope?," *Materials Today*, vol. 11, no. SUPPL. Elsevier, pp. 30–38, 2008.

[110] Lord Rayleigh, "XII. On the manufacture and theory of diffraction-gratings," *London, Edinburgh, Dublin Philos. Mag. J. Sci.*, vol. 47, no. 310, pp. 81–93, Feb. 1874.

[111] F. M. Ross, *Liquid Cell Electron Microscopy*. Cambridge University Press, Cambridge, 2017.

[112] S. W. Hell, "Far-field optical nanoscopy," *Science*, vol. 316, no. 5828. pp. 1153–1158, 25-May-2007.

[113] A. Rose, "Television Pickup Tubes and the Problem of Vision," *Adv. Electron. Electron Phys.*, vol. 1, no. C, pp. 131–166, 1948.

[114] Y. Liao, *Practical Electron Microscopy and Database*. 2018.

[115] F. Winkler *et al.*, "Quantitative measurement of mean inner potential and specimen thickness from high-resolution off-axis electron holograms of ultra-thin layered WSe2," *Ultramicroscopy*, vol. 178, pp. 38–47, 2017.

[116] O. Scherzer, "The theoretical resolution limit of the electron microscope," *J. Appl. Phys.*, vol. 20, no. 1, pp. 20–29, 1949.

[117] K. Schultheiß, F. Pérez-Willard, B. Barton, D. Gerthsen, and R. R. Schröder, "Fabrication of a Boersch phase plate for phase contrast imaging in a transmission electron microscope," *Rev. Sci. Instrum.*, vol. 77, no. 3, p. 33701, Mar. 2006.

[118] M. Dries *et al.*, "Application of a Hilbert phase plate in transmission electron microscopy

Sana Azim   Hamburg, 2020

of materials science samples."

[119] K. Nagayama and R. Danev, "Phase contrast electron microscopy: development of thin-film phase plates and biological applications," *Philos. Trans. R. Soc. B Biol. Sci.*, vol. 363, no. 1500, pp. 2153–2162, Jun. 2008.

[120] K. Nagayama and R. Danev, "Phase-plate electron microscopy: A novel imaging tool to reveal close-to-life nano-structures," *Biophys. Rev.*, vol. 1, no. 1, pp. 37–42, 2009.

[121] R. Pretzsch, M. Dries, S. Hettler, M. Spiecker, M. Obermair, and D. Gerthsen, "Investigation of hole-free phase plate performance in transmission electron microscopy under different operation conditions by experiments and simulations," *Adv. Struct. Chem. Imaging*, vol. 5, no. 1, p. 5, 2019.

[122] E. J. Kirkland, *Advanced Computing in Electron Microscopy Second Edition*, Second. Springer Science+Business Media, LLC, 2010.

[123] R. Danev and K. Nagayama, "Transmission electron microscopy with Zernike phase plate," *Ultramicroscopy*, vol. 88, no. 4, pp. 243–252, 2001.

[124] R. Danev, B. Buijsse, M. Khoshouei, J. M. Plitzko, and W. Baumeister, "Volta potential phase plate for in-focus phase contrast transmission electron microscopy," *PNAS*, vol. 111, no. 44, pp. 15635–15640, Nov. 2014.

[125] R. F. Egerton, P. Li, and M. Malac, "Radiation damage in the TEM and SEM," in *Micron*, 2004, vol. 35, no. 6, pp. 399–409.

[126] N. Jiang, "Electron beam damage in oxides: A review," *Reports Prog. Phys.*, vol. 79, no. 1, Dec. 2015.

[127] R. F. Egerton, "Mechanisms of radiation damage in beam-sensitive specimens, for TEM accelerating voltages between 10 and 300 kV," *Microsc. Res. Tech.*, vol. 75, no. 11, pp. 1550–1556, Nov. 2012.

[128] D. C. Bell, C. J. Russo, and D. V Kolmykov, "40keV atomic resolution TEM," *Ultramicroscopy*, vol. 114, pp. 31–37, 2012.

[129] U. Kaiser *et al.*, "Transmission electron microscopy at 20kV for imaging and spectroscopy," *Ultramicroscopy*, vol. 111, no. 8, pp. 1239–1246, 2011.

Sana Azim   Hamburg, 2020

[130] R. A. Steinbrecht, K. Zierold, S.-V. Berlin, H. New, Y. London, and P. Tokyo, *Cryotechniques in Biological Electron Microscopy*. Springer, Berlin, Heidelberg, 1987.

[131] J. G. Burr, "Radiation chemistry," in *Science*, 1971, vol. 174, no. 4009, p. 616.

[132] O. W. van Assendelft, G. A. Mook, and W. G. Zijlstra, "International System of Units (SI) in physiology," *Pflügers Arch. Eur. J. Physiol.*, vol. 339, no. 4, pp. 265–272, 1973.

[133] K. Sader *et al.*, "Smart acquisition EELS," in *Journal of Physics: Conference Series*, 2010, vol. 241.

[134] P. N. T. Unwin and R. Henderson, "Molecular structure determination by electron microscopy of unstained crystalline specimens," *J. Mol. Biol.*, vol. 94, no. 3, May 1975.

[135] H. N. Chapman *et al.*, "Femtosecond X-ray protein nanocrystallography," *Nature*, vol. 470, no. 7332, pp. 73–78, Feb. 2011.

[136] A. J. Koster, H. Chen, J. W. Sedat, and D. A. Agard, "Automated microscopy for electron tomography," *Ultramicroscopy*, vol. 46, no. 1, pp. 207–227, 1992.

[137] R. Henderson, "Image contrast in high-resolution electron microscopy of biological macromolecules: TMV in ice," *Ultramicroscopy*, vol. 46, no. 1, pp. 1–18, 1992.

[138] R. F. Egerton, "Control of radiation damage in the TEM," *Ultramicroscopy*, vol. 127, pp. 100–108, 2013.

[139] R. Zan, Q. M. Ramasse, R. Jalil, T. Georgiou, U. Bangert, and K. S. Novoselov, "Control of Radiation Damage in MoS2 by Graphene Encapsulation," *ACS Nano*, vol. 7, no. 11, pp. 10167–10174, Nov. 2013.

[140] J. Reyes-Gasga and R. García-García, "Analysis of the electron-beam radiation damage of TEM samples in the acceleration energy range from 0.1 to 2MeV using the standard theory for fast electrons," *Radiat. Phys. Chem.*, vol. 64, pp. 359–367, 2002.

[141] S. M. Salih and V. E. Cosslett, "Reduction in electron irradiation damage to organic compounds by conducting coatings," *Philos. Mag. A J. Theor. Exp. Appl. Phys.*, vol. 30, no. 1, pp. 225–228, Jul. 1974.

[142] C. Wang, Q. Qiao, R. F. Klie, and T. Shokuhfar, "High resolution in-situ study of reactions in graphene liquid cells," in *Microscopy and Microanalysis*, 2014, vol. 20, no.

Sana Azim   Hamburg, 2020

3, pp. 1520–1521.

[143] Mauricio G. Mateu, Ed., *Structure and Physics of Viruses An Integrated Textbook*. Springer, Dordrecht, 2013.

[144] J. C. Doultree *et al.*, "A new electron microscope positive staining method for viruses in suspension," *J. Virol. Methods*, vol. 37, no. 3, pp. 321–335, 1992.

[145] D. F. Barreto-Vieira and O. M. Barth, "Negative and Positive Staining in Transmission Electron Microscopy for Virus Diagnosis," in *Microbiology in Agriculture and Human Health*, InTech, 2015.

[146] C. A. Scarff, M. J. G. Fuller, R. F. Thompson, and M. G. Iadaza, "Variations on negative stain electron microscopy methods: Tools for tackling challenging systems," *J. Vis. Exp.*, vol. 57199, no. 132, Feb. 2018.

[147] H. Wen, Y. Lin, D. N. Seidman, J. M. Schoenung, I. J. Van Rooyen, and E. J. Lavernia, "An Efficient and Cost-Effective Method for Preparing Transmission Electron Microscopy Samples from Powders," *Microsc. Microanal.*, vol. 21, no. 5, pp. 1184–1194, Mar. 2015.

[148] A. Yamaguchi, M. Shibata, and T. Hashinaga, "Transmission electron microscopy specimen preparation technique using focused ion beam fabrication: Application to GaAs metal–semiconductor field effect transistors," *J. Vac. Sci. Technol. B Microelectron. Nanom. Struct.*, vol. 11, no. 6, pp. 2016–2020, Nov. 1993.

[149] J. M. Grogan and H. H. Bau, "The Nanoaquarium: A Platform for In Situ Transmission Electron Microscopy in Liquid Media," *J. MICROELECTROMECHANICAL Syst.*, vol. 19, no. 4, 2010.

[150] J. M. Yuk, H. K. Seo, J. W. Choi, and J. Y. Lee, "Anisotropic Lithiation Onset in Silicon Nanoparticle Anode Revealed by in Situ Graphene Liquid Cell Electron Microscopy," *ACS Nano*, vol. 8, no. 7, pp. 7478–7485, Jul. 2014.

[151] H. G. Liao *et al.*, "Facet development during platinum nanocube growth," *Science (80-.).*, vol. 345, no. 6199, 2014.

[152] T. Lehnert *et al.*, "In Situ Crystallization of the Insoluble Anhydrite AII Phase in Graphene Pockets," *ACS Nano*, vol. 11, no. 8, pp. 7967–7973, Aug. 2017.

[153] D. J. Kelly *et al.*, "Nanometer Resolution Elemental Mapping in Graphene-Based TEM Liquid Cells," *Nano Lett.*, vol. 18, no. 2, pp. 1168–1174, Feb. 2018.

[154] M. T. Proetto *et al.*, "Dynamics of soft nanomaterials captured by transmission electron microscopy in liquid water," *J. Am. Chem. Soc.*, vol. 136, no. 4, pp. 1162–1165, 2014.

[155] J. P. F. Nunes *et al.*, "Liquid-phase mega-electron-volt ultrafast electron diffraction," *Struct. Dyn.*, vol. 7, no. 2, p. 24301, Mar. 2020.

[156] N. De Jonge and F. M. Ross, "Electron microscopy of specimens in liquid," *Nature Nanotechnology*, vol. 6, no. 11. pp. 695–704, 2011.

[157] A. De Clercq, W. Dachraoui, O. Margeat, K. Pelzer, C. R. Henry, and S. Giorgio, "Growth of Pt–Pd Nanoparticles Studied In Situ by HRTEM in a Liquid Cell," *J. Phys. Chem. Lett.*, vol. 5, no. 12, pp. 2126–2130, Jun. 2014.

[158] T. W. Hansen, J. B. Wagner, and R. E. Dunin-Borkowski, "Aberration corrected and monochromated environmental transmission electron microscopy: challenges and prospects for materials science," *Mater. Sci. Technol.*, vol. 26, no. 11, pp. 1338–1344, Nov. 2010.

[159] S. Pu, C. Gong, and A. W. Robertson, "Liquid cell transmission electron microscopy and its applications," *R. Soc. Open Sci.*, vol. 7, no. 1, p. 191204, May 2020.

[160] J. M. Howe and H. Saka, "In Situ Transmission Electron Microscopy Studies of the Solid–Liquid Interface," *MRS Bull.*, vol. 29, no. 12, pp. 951–957, 2004.

[161] L. L. Dai, R. Sharma, and C. Wu, "Self-Assembled Structure of Nanoparticles at a Liquid−Liquid Interface," *Langmuir*, vol. 21, no. 7, pp. 2641–2643, Mar. 2005.

[162] Y. Inayoshi, H. Minoda, Y. Arai, and K. Nagayama, "Direct Observation of biological molecules in liquid by environmental phase-plate transmission electron microscopy," *Micron*, vol. 43, pp. 1091–1098, 2012.

[163] C. Mueller, "In Situ Techniques for Structure Determination in the Liquid Phase," pp. 1–146, 2014.

[164] Sercan Keskin, "In-liquid Electron Microscopy and Diffraction for real-time observation and structural analysis," 2016.

[165] M. Tilli and A. Haapalinna, "Chapter 1 - Properties of Silicon," in *Micro and Nano Technologies*, M. Tilli, T. Motooka, V.-M. Airaksinen, S. Franssila, M. Paulasto-Kröckel, and V. B. T.-H. of S. B. M. M. and T. (Second E. Lindroos, Eds. Boston: William Andrew Publishing, 2015, pp. 3–17.

[166] U. Helmersson, M. Lattemann, J. Bohlmark, A. P. Ehiasarian, and J. T. Gudmundsson, "A review of technology and applications. Thin Solid Films," *Thin Solid Films*, vol. 513, no. 1–2. pp. 1–24, 2006.

[167] D. M. Mattox, *Handbook of Physical Vapor Deposition (PVD) Processing*. William Andrew, 2010.

[168] S. Franssila, *Introduction to Microfabrication Second Edition*, Second. John Wiley & Sons Ltd, 2010.

[169] Ghannama. M. Y. and Nijsb. J. F., "Encyclopedia of Materials: Science and Technology." pp. 7728–7735, 2001.

[170] Campbell. S. A., *The Science and Engineering of Microelectronic fabrication*. Oxford University Press, 2013.

[171] C. Yang and J. Pham, "Characteristic Study of Silicon Nitride Films Deposited by LPCVD and PECVD," *Silicon*, vol. 10, no. 6, pp. 2561–2567, Nov. 2018.

[172] M. J. Madou, *Fundamentals of microfabrication : the science of miniaturization*. 2002.

[173] G. T. A. Kovacs, N. I. Maluf, and K. E. Petersen, "Bulk Micromachining of Silicon," *Proc. IEEE*, vol. 86, no. 8, pp. 1536–1551, 1998.

[174] W. C. Madou M., "Photolithography," in *Encyclopedia of Nanotechnology*, Bhushan B., Ed. Springer, Dordrecht, 2012.

[175] K. M. Pala N., "Electron Beam Lithography (EBL)," in *Encyclopedia of Nanotechnology*, B. B., Ed. Springer, Dordrecht, 2016.

[176] M. C. King and D. H. Berry, "Photolithographic Mask Alignment Using Moire Techniques," *Appl. Opt.*, vol. 11, no. 11, pp. 2455–2459, 1972.

[177] K. Ronse, "Optical lithography-a historical perspective," *Comptes Rendus Phys.*, vol. 7, pp. 844–857, 2006.

[178] C. Wu, H. Hsieh, and Y. Lee, "Contact Photolithography at Sub-Micrometer Scale Using a Soft Photomask," *Micromachines*, vol. 10, no. 8, p. 547, Aug. 2019.

[179] F. H. Dill, W. P. Hornberger, P. S. Hauge, and J. M. Shaw, "Characterization of positive photoresist," *IEEE Trans. Electron Devices*, vol. 22, no. 7, pp. 445–452, 1975.

[180] R. O. Lussow, "Photoresist Materials and Applications," *J. Vac. Sci. Technol.*, vol. 6, no. 1, pp. 18–24, Jan. 1969.

[181] S. J. Shaw, J. M., Gelorme, J.D., LaBianca, N.C., Conley, W.E., Holmes, "Negative photoresists for optical lithography," *IBM J. Res. Dev.*, vol. 41, no. 1.2, pp. 81–94, 1997.

[182] N. P. Pham, E. Boellaard, J. N. Burghartz, and P. M. Sarro, "Photoresist coating methods for the integration of novel 3-D RF microstructures," *J. Microelectromechanical Syst.*, vol. 13, no. 3, pp. 491–499, Jun. 2004.

[183] P. Y. P. Adelyn *et al.*, "Transparent mask design and fabrication of interdigitated electrodes," in *IEEE Regional Symposium on Micro and Nanoelectronics (RSM) Kuala Terengganu*, 2015, pp. 1–4.

[184] M. Aslam, "Bulk etching of silicon wafer and development of a polyimide membrane," in *Journal of Physics: Conference Series*, 2013, vol. 439, no. 1.

[185] B. Wu, A. Kumar, and S. Pamarthy, "High aspect ratio silicon etch: A review," *J. Appl. Phys.*, vol. 108, no. 5, Sep. 2010.

[186] F. Marty *et al.*, "Advanced etching of silicon based on deep reactive ion etching for silicon high aspect ratio microstructures and three-dimensional micro- and nanostructures," *Microelectronics J.*, vol. 36, no. 7, pp. 673–677, 2005.

[187] T. Ray, H. Zhu, and D. R. Meldrum, "Deep reactive ion etching of fused silica using a single-coated soft mask layer for bio-analytical applications," *J. Micromechanics Microengineering*, vol. 20, no. 9, Sep. 2010.

[188] S. Keskin, P. Kunnas, and N. de Jonge, "Liquid-Phase Electron Microscopy with Controllable Liquid Thickness," *Nano Lett.*, 2019.

[189] A. A. Petruk, C. Allen, N. Rivas, K. Pichugin, and G. Sciaini, "High flow rate nanofluidics for in-liquid electron microscopy and diffraction," *Nanotechnology*, vol. 30, no. 39, p. 395703, 2019.

Sana Azim

[190] J. R. Dwyer and M. Harb, "Through a Window, Brightly: A Review of Selected Nanofabricated Thin-Film Platforms for Spectroscopy, Imaging, and Detection," *Applied Spectroscopy*, vol. 71, no. 9. SAGE Publications Inc., pp. 2051–2075, 01-Sep-2017.

[191] D. R. Ciarlo, "Silicon Nitride Thin Windows for Biomedical Microdevices," *Biomed. Microdevices*, vol. 4, no. 1, pp. 63–68, 2002.

[192] H. W. Lefevre, R. M. S. Schofield, and D. R. Ciarlo, "Thin Si3N4 windows for energy loss STIM in air," *Nucl. Inst. Methods Phys. Res. B*, vol. 54, no. 1, pp. 47–51, 1991.

[193] M. L. Cowan *et al.*, "Ultrafast memory loss and energy redistribution in the hydrogen bond network of liquid H2O," *Nature*, vol. 434, no. 7030, pp. 199–202, Mar. 2005.

[194] R. Ghodssi and P. Lin, Eds., *MEMS Materials and Processes Handbook*. Springer, Boston, MA, 2011.

[195] M. Harb, "Investigating photoinduced structural changes in silicon using femtosecond electron diffraction," *Ph.D. Thesis*. 01-Jan-2009.

[196] Keskin S. *et al.*, "Direct Observation of Multimerization and Self-Assembly of DNA Functionalized Gold Nanoparticles using In-Liquid Transmission Electron Microscopy."

[197] D. W. Burns and H. Guckel, "Thin films for micromechanical sensors," *J. Vac. Sci. Technol. A*, vol. 8, no. 4, pp. 3606–3613, Jul. 1990.

[198] Venegas-Rojas D., Keskin S., Azim S., Manz S., Miller R. J. D., and Trieu H. K., "Multi-window Transmission Electron Microscopy liquid cell to improve imaging performance," 2017.

[199] J. W. Beams, "Mechanical properties of thin films of gold and silver," *Structure and properties of thin films*. John Wiley and Sons, pp. 183–192, 1959.

[200] M. K. Small and W. D. Nix, "Analysis of the accuracy of the bulge test in determining the mechanical properties of thin films," *J. Mater. Res.*, vol. 7, no. 6, pp. 1553–1563, 1992.

[201] N. Huse *et al.*, "Probing the hydrogen-bond network of water via time-resolved soft X-ray spectroscopy," *Phys. Chem. Chem. Phys.*, vol. 11, no. 20, pp. 3951–3957, 2009.

[202] Q. Zhang *et al.*, "Bioinspired engineering of honeycomb structure - Using nature to inspire human innovation," *Prog. Mater. Sci.*, vol. 74, pp. 332–400, 2015.

[203] S. Giorgio, S. Sao Joao, S. Nitsche, D. Chaudanson, G. Sitja, and C. R. Henry, "Environmental electron microscopy (ETEM) for catalysts with a closed E-cell with carbon windows," *Ultramicroscopy*, 2006.

[204] J. Wu *et al.*, "In Situ Environmental TEM in Imaging Gas and Liquid Phase Chemical Reactions for Materials Research," *Advanced Materials*. 2016.

[205] S. W. Hui and D. F. Parsons, "Electron Diffraction of Wet Biological Membranes," *Science (80-.).*, vol. 184, no. 4132, pp. 77–78, 1974.

[206] J. H. Wang, R. P. Sagar, H. Schmider, and V. H. Smith, "X-Ray Elastic and Inelastic Scattering Factors for Neutral Atoms Z = 2-92," *At. Data Nucl. Data Tables*, vol. 53, no. 2, pp. 233–269, 1993.

[207] M. Zhang, H., Egerton, R.F., and Malac, "Local Thickness Measurement in TEM," *Microsc. Microanal.*, vol. 16, no. Suppl 2, pp. 6–7, 2010.

[208] J. Park *et al.*, "Direct Observation of Wet Biological Samples by Graphene Liquid Cell Transmission Electron Microscopy," *Nano Lett.*, 2015.

[209] J. Hermannsdörfer, V. Tinnemann, D. B. Peckys, and N. De Jonge, "The Effect of Electron Beam Irradiation in Environmental Scanning Transmission Electron Microscopy of Whole Cells in Liquid," *Microsc. Microanal.*, vol. 22, no. 3, pp. 656–665, Feb. 2016.

[210] S. Keskin, P. Kunnas, and N. de Jonge, "Liquid-Phase Electron Microscopy with Controllable Liquid Thickness," *Nano Lett.*, vol. 19, no. 7, pp. 4608–4613, 2019.

[211] S. Le Caër, "Water Radiolysis: Influence of Oxide Surfaces on H2 Production under Ionizing Radiation," *Water*, vol. 3, no. 1, pp. 235–253, 2011.

[212] N. M. Schneider, M. M. Norton, B. J. Mendel, J. M. Grogan, F. M. Ross, and H. H. Bau, "Electron-Water interactions and implications for liquid cell electron microscopy," *J. Phys. Chem. C*, vol. 118, no. 38, pp. 22373–22382, Sep. 2014.

[213] T. J. Woehl and P. Abellan, "Defining the radiation chemistry during liquid cell electron microscopy to enable visualization of nanomaterial growth and degradation dynamics,"

Sana Azim   Hamburg, 2020

J. Microsc., vol. 265, no. 2, pp. 135–147, 2017.

[214] T. Gupta, N. M. Schneider, J. H. Park, D. Steingart, and F. M. Ross, "Spatially dependent dose rate in liquid cell transmission electron microscopy," *Nanoscale*, vol. 10, no. 16, pp. 7702–7710, 2018.

[215] M. R. Libera and R. F. Egerton, "Advances in the transmission electron microscopy of polymers," *Polym. Rev.*, vol. 50, no. 3, pp. 321–339, 2010.

[216] K. H. Nagamanasa, H. Wang, and S. Granick, "Liquid-Cell Electron Microscopy of Adsorbed Polymers," *Adv. Mater.*, vol. 29, no. 41, 2017.

[217] R. Fan, S. W. Chew, V. V. Cheong, and B. P. Orner, "Fabrication of gold nanoparticles inside unmodified horse spleen apoferritin," *Small*, vol. 6, no. 14, pp. 1483–1487, Jul. 2010.

[218] Y. Marechal, *The Hydrogen Bond and the Water Molecule*. Elsevier, 2007.

[219] S. Scheiner, *Hydrogen Bonding*. Oxford University Press: New York, 1997.

[220] G. A. Jeffrey, *An Introduction to Hydrogen Bonding*. Oxford University Press, 1997.

[221] T. Desiraju, G. R.; Steiner, *The Weak Hydrogen Bond*. Oxford University Press: Oxford, 1999.

[222] P. Hobza and Z. Havlas, "Blue-Shifting Hydrogen Bonds," *Chem. Rev.*, vol. 100, no. 11, pp. 4253–4264, Nov. 2000.

[223] P. E. Hansen, F. S. Kamounah, B. A. Saeed, M. J. MacLachlan, and J. Spanget-Larsen, "Intramolecular hydrogen bonds in normal and sterically compressed o-hydroxy aromatic aldehydes. Isotope effects on chemical shifts and hydrogen bond strength," *Molecules*, vol. 24, no. 24, Dec. 2019.

[224] F. Fillaux, N. Leygue, J. Tomkinson, A. Cousson, and W. Paulus, "Structure and dynamics of the symmetric hydrogen bond in potassium hydrogen maleate: A neutron scattering study," *Chem. Phys.*, vol. 244, no. 2–3, pp. 387–403, 1999.

[225] A. H. Narten, W. E. Thiessen, and L. Blum, "Atom pair distribution functions of liquid water at 25°C from neutron diffraction," *Science (80-.).*, vol. 217, no. 4564, pp. 1033–1034, 1982.

[226] A. K. Soper, "The Radial Distribution Functions of Water as Derived from Radiation Total Scattering Experiments: Is There Anything We Can Say for Sure?," *ISRN Phys. Chem.*, vol. 2013, pp. 1–67, 2013.

[227] L. B. Skinner, C. Huang, D. Schlesinger, L. G. M. Pettersson, A. Nilsson, and C. J. Benmore, "Benchmark oxygen-oxygen pair-distribution function of ambient water from x-ray diffraction measurements with a wide Q-range," *J. Chem. Phys.*, vol. 138, no. 7, 2013.

[228] E. Kálman, G. Pálinkás, and P. Kovács, "Liquid water," *Mol. Phys.*, vol. 34, no. 2, pp. 505–524, 1977.

[229] S. Lengyel and E. Kalman, "Electron diffraction in liquid water," *Nature*, vol. 248, pp. 405–406, 1974.

[230] J. A. Zernike, F., Prins, "Die Beugung von Röntgenstrahlen in Flüssigkeiten als Effekt der Molekülanordnung," *Zeitschrift für Phys.*, vol. 41, no. 6–7, pp. 184–194, 1927.

[231] H. Debye, P. and Menke, "The determination of the inner structure of liquids by x-ray means," *Phys Z*, vol. 31, pp. 797–798, 1930.

[232] K. Amann-Winkel *et al.*, "X-ray and Neutron Scattering of Water," *Chemical Reviews*, vol. 116, no. 13. American Chemical Society, pp. 7570–7589, 13-Jul-2016.

[233] J. H. Wang, R. P. Sagar, H. Schmider, and V. H. Smith, "X-ray elastic and inelastic scattering factors for neutral atoms Z = 2-92," *At. Data Nucl. Data Tables*, 1993.

[234] T. Aiyama, T. Fukunaga, K. Niihara, T. Hirai, and K. Suzuki, "An X-ray diffraction study of the amorphous structure of chemically vapor-deposited silicon nitride," *J. Non. Cryst. Solids*, vol. 33, no. 2, pp. 131–139, 1979.

[235] J. M. Sorenson, G. Hura, R. M. Glaeser, and T. Head-Gordon, "What can X-ray scattering tell us about the radial distribution functions of water?," *J. Chem. Phys.*, vol. 113, no. 20, pp. 9149–9161, Nov. 2000.

[236] A. K. Soper, "The Radial Distribution Functions of Water as Derived from Radiation Total Scattering Experiments: Is There Anything We Can Say for Sure?," *ISRN Phys. Chem.*, vol. 2013, p. 279463, 2013.

[237] A. K. Soper and M. G. Phillips, "A new determination of the structure of water at 25°C,"

Sana Azim   Hamburg, 2020

Chem. Phys., vol. 107, no. 1, pp. 47–60, 1986.

[238] T. E. Gorelik, "Electron Pair-Distribution Function (ePDF) Analysis," pp. 1–18.

[239] T. E. Gorelik *et al.*, "Towards quantitative treatment of electron pair distribution function," *Acta Crystallogr. Sect. B*, vol. 75, no. 4, pp. 532–549, Aug. 2019.

[240] A. K. Soper and C. J. Benmore, "Quantum differences between heavy and light water," *Phys. Rev. Lett.*, vol. 101, no. 6, pp. 1–4, 2008.

[241] S. Myneni *et al.*, "Spectroscopic probing of local hydrogen-bonding structures in liquid water," *J. Phys. Condens. Matter*, vol. 14, no. 8, pp. L213–L219, 2002.

[242] C. Huang *et al.*, "The inhomogeneous structure of water at ambient conditions," *Proc. Natl. Acad. Sci.*, vol. 106, no. 36, pp. 15214 LP – 15218, Sep. 2009.

[243] P. Das, J. A. King, and R. Zhou, "Aggregation of -crystallins associated with human cataracts via domain swapping at the C-terminal -strands," *Proc. Natl. Acad. Sci.*, 2011.

[244] K. L. Moreau and J. A. King, "Protein misfolding and aggregation in cataract disease and prospects for prevention," *Trends in Molecular Medicine*, vol. 18, no. 5. pp. 273–282, 2012.

[245] K. W. Roskamp *et al.*, "Multiple aggregation pathways in human γS-crystallin and its aggregation-prone G18V variant," *Investig. Ophthalmol. Vis. Sci.*, vol. 58, no. 4, pp. 2397–2405, 2017.

[246] L. Rivillas-Acevedo, A. Fernández-Silva, and C. Amero, "Function, structure and stability of human gamma d crystallins: A review," in *Physical Biology of Proteins and Peptides: Theory, Experiment, and Simulation*, L. Olivares-Quiroz, O. Guzmán-López, and H. Jardón-Valadez, Eds. Springer International Publishing, 2015, pp. 81–98.

[247] K. N. Liem-The, A. L. H. Stols, P. H. K. Jap, and H. J. Hoenders, "X-ray induced cataract in rabbit lens," *Exp. Eye Res.*, vol. 20, no. 4, pp. 317–328, 1975.

[248] J. Zhang, H. Yan, S. Löfgren, X. Tian, and M. F. Lou, "Ultraviolet Radiation–Induced Cataract in Mice: The Effect of Age and the Potential Biochemical Mechanism," *Invest. Ophthalmol. Vis. Sci.*, vol. 53, no. 11, pp. 7276–7285, Oct. 2012.

[249] A. R. Wegener, "In vivo studies on the effect of UV-radiation on the eye lens in animals,"

Doc Ophthalmol , vol. 88, pp. 221–232, 1995.

[250] K. Wu, Y. B. Shui, M. Kojima, H. Murano, K. Sasaki, and O. Hockwin, "Location and Severity of UVB Irradiation Damage in the Rat Lens," *Jpn. J. Ophthalmol.*, vol. 41, no. 6, pp. 381–387, 1997.

[251] K. W. Roskamp *et al.*, "Human γS-crystallin copper binding helps buffer against aggregation caused by oxidative damage," *Biochemistry*, Jun. 2020.

[252] I. Amenti, R. Mills-Henry, and M. S. Biology, "STABILITY, UNFOLDING, AND AGGREGATION OF THE GAMMA D AND GAMMA S HUMAN EYE LENS CRYSTALLINS," 2007.

[253] W. D. Brubaker *et al.*, "Separating instability from aggregation propensity in γS-crystallin variants," *Biophys. J.*, vol. 100, no. 2, pp. 498–506, Jan. 2011.

[254] H. Sun *et al.*, "Gamma-S crystallin gene (CRYGS) mutation causes dominant progressive cortical cataract in humans," *J. Med. Genet.*, vol. 42, no. 9, pp. 706 LP – 710, Sep. 2005.

[255] I. Khan, S. Chandani, and D. Balasubramanian, "Structural study of the G57W mutant of human gamma-S-crystallin, associated with congenital cataract," *Mol. Vis.*, vol. 22, pp. 771–782, Jul. 2016.

[256] S. Karri, R. B. Kasetti, V. P. R. Vendra, S. Chandani, and D. Balasubramanian, "Structural analysis of the mutant protein D26G of human γS-crystallin, associated with Coppock cataract," *Mol. Vis.*, vol. 19, pp. 1231–1237, 2013.

[257] Z. Ma, G. Piszczek, P. T. Wingfield, Y. V. Sergeev, and J. F. Hejtmancik, "The G18V CRYGS mutation associated with human cataracts increases γS-crystallin sensitivity to thermal and chemical stress," *Biochemistry*, vol. 48, no. 30, pp. 7334–7341, 2009.

[258] S. R. A. HANSON, D. L. SMITH, and J. B. SMITH, "Deamidation and Disulfide Bonding in Human Lens γ-Crystallins," *Exp. Eye Res.*, vol. 67, no. 3, pp. 301–312, 1998.

[259] V. N. Lapko, D. L. Smith, and J. B. Smith, "Methylation and carbamylation of human γ-crystallins," *Protein Sci.*, vol. 12, no. 8, pp. 1762–1774, Aug. 2003.

[260] D.-Y. Li, R. F. Borkman, R.-H. Wang, and J. Dillon, "Mechanisms of photochemically produced turbidity in lens protein solutions," *Exp. Eye Res.*, vol. 51, no. 6, pp. 663–669,

1990.

[261] V. P. R. Vendra, S. Chandani, and D. Balasubramanian, "The Mutation V42M Distorts the Compact Packing of the Human Gamma-S-Crystallin Molecule, Resulting in Congenital Cataract," *PLoS One*, 2012.

[262] D. Balasubramanian, V. P. Vendra, G. Agarwal, S. Chandani, V. Talla, and N. Srinivasan, "Effect of mutations on the structure and stability of lens βγ crystallins and their phenotypic relevance," *Invest. Ophthalmol. Vis. Sci.*, vol. 55, no. 13, p. 4050, Apr. 2014.

[263] L. Quintanar *et al.*, "Copper and Zinc Ions Specifically Promote Nonamyloid Aggregation of the Highly Stable Human γ-D Crystallin," *ACS Chem. Biol.*, vol. 11, no. 1, pp. 263–272, Jan. 2016.

[264] S. ZIGMAN, "Environmental near-UV radiation and cataracts," *Optom. Vis. Sci.*, vol. 72, no. 12, pp. 899–901, 1995.

[265] P. Das, J. A. King, and R. Zhou, "Aggregation of γ-crystallins associated with human cataracts via domain swapping at the C-terminal β-strands," *Proc. Natl. Acad. Sci. U. S. A.*, vol. 108, no. 26, pp. 10514–10519, 2011.

[266] R. Cacace, K. Sleegers, and C. Van Broeckhoven, "Molecular genetics of early-onset Alzheimer's disease revisited," *Alzheimer's Dement.*, vol. 12, no. 6, pp. 733–748, Jun. 2016.

[267] L. Pauling, H. A. Itano, S. J. Singer, and I. C. Wells, "Sickle Cell Anemia, a Molecular Disease," *Science (80-.).*, vol. 110, no. 2865, pp. 543 LP – 548, Nov. 1949.

[268] A. Binolfi, L. Quintanar, C. W. Bertoncini, C. Griesinger, and C. O. Fernández, "Bioinorganic chemistry of copper coordination to alpha-synuclein: Relevance to Parkinson's disease," *Coord. Chem. Rev.*, vol. 256, no. 19, pp. 2188–2201, 2012.

[269] A. I. Bush, "The metallobiology of Alzheimer's disease," *Trends Neurosci.*, vol. 26, no. 4, pp. 207–214, Apr. 2003.

[270] P. Faller, C. Hureau, and G. La Penna, "Metal Ions and Intrinsically Disordered Proteins and Peptides: From Cu/Zn Amyloid-β to General Principles," *Acc. Chem. Res.*, vol. 47, no. 8, pp. 2252–2259, Aug. 2014.

Sana Azim   Hamburg, 2020

[271] F. W. Studier, "Protein production by auto-induction in high-density shaking cultures," *Protein Expr. puri_cation*, vol. 41, pp. 207–234, 2005.

[272] J. Chen, P. R. Callis, and J. King, "Mechanism of the very efficient quenching of tryptophan fluorescence in human γD- and γS-crystallins: The γ-crystallin fold may have evolved to protect tryptophan residues from ultraviolet photodamage," *Biochemistry*, vol. 48, no. 17, pp. 3708–3716, May 2009.

[273] J. Chen, S. L. Flaugh, P. R. Callis, and J. King, "Mechanism of the highly efficient quenching of tryptophan fluorescence in human γD-crystallin," *Biochemistry*, vol. 45, no. 38, pp. 11552–11563, Sep. 2006.

[274] J. Xu *et al.*, "Femtosecond fluorescence spectra of tryptophan in human γ-Crystallin mutants: Site-dependent ultrafast quenching," *J. Am. Chem. Soc.*, vol. 131, no. 46, pp. 16751–16757, 2009.

[275] E. Serebryany and J. A. King, "Wild-type human γD-crystallin promotes aggregation of its oxidation-mimicking, misfolding-prone W42Q mutant.," *J. Biol. Chem.*, vol. 290, no. 18, pp. 11491–503, May 2015.

[276] K. J. Lampi *et al.*, "Age-related Changes in Human Lens Crystallins Identified by Two-dimensional Electrophoresis and Mass Spectrometry," Article Number, 1998.

[277] P. A. Wilmarth *et al.*, "Age-related changes in human crystalline determined from comparative analysis of post-translational modifications in young and aged lens: Does deamidation contribute to crystallin insolubility?," *J. Proteome Res.*, vol. 5, no. 10, pp. 2554–2566, Oct. 2006.

[278] J. A. Domínguez-Calva, M. L. Pérez-Vázquez, E. Serebryany, J. A. King, and L. Quintanar, "Mercury-induced aggregation of human lens γ-crystallins reveals a potential role in cataract disease," *J. Biol. Inorg. Chem.*, vol. 23, no. 7, pp. 1105–1118, Oct. 2018.

[279] K. W. Roskamp, N. Kozlyuk, S. Sengupta, J. C. Bierma, and R. W. Martin, "Divalent cations and the divergence of βγ-crystallin function," *Biochemistry*, p. acs.biochem.9b00507, Oct. 2019.

[280] J. H. Kaplan, B. Forbush, and J. F. Hoffman, "Rapid photolytic release of adenosine 5'-triphosphate from a protected analog: utilization by the sodium:potassium pump of human red blood cell ghosts," *Biochemistry*, vol. 17, no. 10, pp. 1929–1935, May 1978.

Sana Azim   Hamburg, 2020

[281] J. P. Casey, R. A. Blidner, and W. T. Monroe, "Caged siRNAs for Spatiotemporal Control of Gene Silencing," *Mol. Pharm.*, vol. 6, no. 3, pp. 669–685, Jun. 2009.

[282] I. Dourki *et al.*, "Characterization and optimization of a thin direct electron detector for fast imaging applications," *J. Instrum.*, vol. 12, no. 03, pp. C03047–C03047, 2017.

[283] G. Singh, R. Bücker, G. Kassier, R. J. D. Miller, and S. T. Purcell, "Development of a LaB6 based ultra-bright cold field emitter electron source," in *2017 30th International Vacuum Nanoelectronics Conference (IVNC)*, 2017, pp. 144–145.

[284] G. Singh *et al.*, "Fabrication and characterization of a focused ion beam milled lanthanum hexaboride based cold field electron emitter source," *Appl. Phys. Lett.*, vol. 113, no. 9, p. 93101, Aug. 2018.

[285] R. S. Dias, B. Lindman, and M. G. Miguel, "DNA interaction with catanionic vesicles," *J. Phys. Chem. B*, vol. 106, no. 48, pp. 12600–12607, Dec. 2002.

[286] C. R. Rädler, J.O., Koltover, I., Salditt, T., Safinya, "Structure of DNA-Cationic Liposome Complexes: DNA Intercalation in Multilamellar Membranes in Distinct Interhelical Packing Regimes," *Science (80-.).*, vol. 275, no. 5301, pp. 810–814, 1997.

[287] I. Koltover, T. Salditt, J. O. Rädler, and C. R. Safinya, "An inverted hexagonal phase of cationic liposome-DNA complexes related to DNA release and delivery," *Science (80-.).*, vol. 281, no. 5373, pp. 78–81, 1998.

[288] D. D. Lasic, H. Strey, M. C. A. Stuart, R. Podgornik, and P. M. Frederik, "The structure of DNA - Liposome complexes," *J. Am. Chem. Soc.*, vol. 119, no. 4, pp. 832–833, 1997.

[289] J. Gustafsson, G. Arvidson, G. Karlsson, and M. Almgren, "Complexes between cationic liposomes and DNA visualized by cryo-TEM," *BBA - Biomembr.*, vol. 1235, no. 2, pp. 305–312, 1995.

[290] B. J. Battersby, R. Grimm, S. Huebner, and G. Cevc, "Evidence for three-dimensional interlayer correlations in cationic lipid-DNA complexes as observed by cryo-electron microscopy," *Biochim. Biophys. Acta - Biomembr.*, vol. 1372, no. 2, pp. 379–383, 1998.

[291] T. Salditt, I. Koltover, J. O. Rädler, and C. R. Safinya, "Two-Dimensional Smectic Ordering of Linear DNA Chains in Self-Assembled DNA-Cationic Liposome Mixtures," *Phys. Rev. Lett.*, vol. 79, pp. 2582–2585, 1997.

Sana Azim   Hamburg, 2020

[292] P. L. Felgner *et al.*, "Lipofection: a highly efficient, lipid-mediated DNA-transfection procedure," *Proc. Natl. Acad. Sci.*, vol. 84, no. 21, pp. 7413–7417, Nov. 1987.

[293] P. L. Felgner and G. M. Ringold, "Cationic liposome-mediated transfection," *Nature*, vol. 337, pp. 387–388, 1989.

[294] H. Gershon, R. Ghirlando, S. B. Guttman, and A. Minsky, "Mode of Formation and Structural Features of DNA-Cationic Liposome Complexes Used for Transfectiont," *Biochemistry*, vol. 32, no. 28, pp. 7143–7151, 1993.

[295] B. Sternberg, F. L. Sorgi, and L. Huang, "New structures in complex formation between DNA and cationic liposomes visualized by freeze-fracture electron microscopy," *FEBS Lett.*, vol. 356, no. 2–3, pp. 361–366, 1994.

[296] B. Ruozi, G. Tosi, E. Leo, and M. A. Vandelli, "Application of atomic force microscopy to characterize liposomes as drug and gene carriers," *Talanta*, vol. 73, no. 1, pp. 12–22, 2007.

[297] S. M. Mel'nikov, R. Dias, Y. S. Mel'nikova, E. F. Marques, M. G. Miguel, and B. Lindman, "DNA conformational dynamics in the presence of catanionic mixtures," *FEBS Lett.*, vol. 453, no. 1–2, pp. 113–118, 1999.

[298] M. G. Miguel, A. A. C. C. Pais, R. S. Dias, C. Leal, M. Rosa, and B. Lindman, "DNA-cationic amphiphile interactions," *Colloids Surfaces A Physicochem. Eng. Asp.*, vol. 228, no. 1–3, pp. 43–55, 2003.

[299] J. Jay *et al.*, "IgG Antibody 3D Structures and Dynamics," *Antibodies*, vol. 7, no. 2, p. 18, 2018.

Acknowledgement

visionary scientist. I would also like to thank Prof. Dr. Nils Huse for his guidance and sharing his valuable point of view in the meetings we have had.

I would like to express my sincere gratitude to Dr. Günther Kassier. He has taken not only great responsibility in decision-making, planning and problem-solving throughout the project but also made priceless contributions to the experiments while educating me at the same time. I cannot find significant words to describe my appreciation for his impact on my scientific development, as well as his gentleness and endurance while being an outstanding and friendly supervisor.

I would like to thank Dr. Michiel de Kock for his contributions to develop the theoretical basis for most of the experimental work done in this thesis. I would also like to express my gratitude to, Dr. Pedram Mehrabi, Dr. Eike Christian Schulz, Dr. Dennis Egert and Dr. Robert Bücker for their vast contributions and for creating the excellent working environment that has made this work possible. I am very grateful to my colleague and friend, Ms Lindsey M Bultema, for providing a very supportive and enlightening hand throughout my PhD journey.

I would also like to sincerely thank Trieu Group in TUHH, Deybith Venegas-Rojas, Mrs Freia Gast, and Prof. Dr. Hoc Khiem Trieu for their essential contribution to the nanofabrication part of the project. My sincere thanks to Dr. Kyle W Roskamp, and his supervisor Rachel W Martin for collaborating on an exciting project of Human γS-crystallin.

I would like to thank Dr. Sercan Keskin and Dr. Stephanie Manz for providing the initial training and guidance in the commencement of the project.

I would like to thank the outstanding engineers of the Miller group, Josef Gonschior and Djordje Gitaric for all the intelligent designs ideas and Carsten Meklenburg (Mecki) for excellent machining. I would like to acknowledge the unlimited scientific support from the Machine physics, MPSD, Dr. Friedjof Tellkamp, Jan-Philipp Leimkohl, Hendrik Schikora, and Martin Kollewe.

I express thanks for the entire Miller group, Dr. Sascha Epp, Dr. Heinrich Schwoerer, Sadegh Bakhtiarzadeh, Dr. Maria Katsiaflaka, Gopal Singh… for their support and friendship.

Last but not least, I would like to express heartfelt thanks to my family, especially my parents, who supported me mentally and guided me to walk through this journey successfully.

Sana Azim   Hamburg, 2020